

Cover photo:

Novel oxide-free vertical-cavity surface-emitting lasers (VCSELs) with monolithically integrated phototransistor (PT) for optically self-controlled current confinement. As indicated in the schematic, the PT region is conductive where the laser mode establishes. Areas unexposed by laser light remain isolating, which restricts the current density distribution to the cross-section of the laser mode. Experimental light-current-voltage curves show hysteresis behavior induced by the phototransistor. The background depicts PT-VCSEL test structures with contact openings varying from 10 to 150 μm diameter. See the related article on p. 13.

Contents

Staff	II
--------------	----

Preface	1
----------------	---

Articles

Quantum-Well-Pumped Semiconductor Disk Lasers	3
VCSELs With Optically Controlled Current Confinement	13
Determination of the Thermal Resistance of VCSELs	21
New Approaches for Birefringence Tuning in VCSELs	29
Studies of (11 $\bar{2}$ 2) Oriented GaN Using Marker Layers	35
Semipolar GaInN Quantum Wells	45
Iron-doped GaN	53
Optical Biosensing of Ferritins	57
Investigation of AlBGaN Structures for UV-Lighting	65

Lists of Publications

Ph.D. Theses	71
Diploma and Master Theses	72
Bachelor Theses	74
Talks and Conference Contributions	75
Publications	78





- | | | |
|-------------------------|----------------------|-------------------------|
| 1: Oliver Rettig | 2: Peter Unger | 3: Rudolf Rösch |
| 4: Karl Joachim Ebeling | 5: Hildegard Mack | 6: Susanne Menzel |
| 7: Rainer Blood | 8: Jürgen Mähniß | 9: Rainer Michalzik |
| 10: Dominik Heinz | 11: Ferdinand Scholz | 12: Marian Caliebe |
| 13: Markus Polanik | 14: Thomas Zwosta | 15: Markus Daubenschütz |
| 16: Tobias Pusch | 17: Sven Bader | |

Not on the photo:

Sükran Kilic, Gerlinde Meixner, Eva Nüble, Ilona Schwaiger

Ulm University Institute of Optoelectronics

Albert-Einstein-Allee 45, 89081 Ulm, Germany
 URL: <http://www.uni-ulm.de/opto>
 Fax: +49-731/50-260 49
 Phone: +49-731/50-

Head of Institute

Prof. Dr. Karl Joachim Ebeling -2 60 51 karljoachim.ebeling@uni-ulm.de

Deputy Head

Prof. Dr. Ferdinand Scholz -2 60 52 ferdinand.scholz@uni-ulm.de

Prof. Dr. Peter Unger -2 60 54 peter.unger@uni-ulm.de

Group Leader

apl. Prof. Dr.-Ing. Rainer Michalzik -2 60 48 rainer.michalzik@uni-ulm.de

Cleanroom Management

Dr.-Ing. Jürgen Mähnbß -2 60 53 juergen.maehns@uni-ulm.de

Secretaries

Sükran Kilic -2 60 59 suekran.kilic@uni-ulm.de

Hildegard Mack -2 60 60 hildegard.mack@uni-ulm.de

Eva Nüßle -2 60 50 eva.nuessle@uni-ulm.de

Research Staff

M. Sc. Sven Bader -2 60 37 sven.bader@uni-ulm.de

Dipl.-Ing. Marian Caliebe -2 60 39 marian.caliebe@uni-ulm.de

M. Sc. Markus Daubenschütz -2 60 38 markus.daubenschue@uni-ulm.de

Dipl.-Ing. Alexander Hein* -2 60 46 alexander.hein@uni-ulm.de

Dipl.-Phys. Dominik Heinz -2 60 39 dominik.heinz@uni-ulm.de

Dipl.-Ing. Martin Klein* -2 60 44 martin.klein@uni-ulm.de

Dipl.-Phys. Tobias Meisch* -2 60 36 tobias.meisch@uni-ulm.de

M. Sc. Markus Polanik -2 60 46 markus.polanik@uni-ulm.de

M. Sc. Tobias Pusch -2 60 37 tobias.pusch@uni-ulm.de

M. Sc. Oliver Rettig -2 60 36 oliver.rettig@uni-ulm.de

Technical Staff

Rainer Blood -2 60 44 rainer.blood@uni-ulm.de

Gerlinde Meixner -2 60 41 gerlinde.meixner@uni-ulm.de

Susanne Menzel -2 60 41 susanne.menzel@uni-ulm.de

Rudolf Rösch -2 60 57 rudolf.roesch@uni-ulm.de

Ilona Schwaiger⁺ -2 60 36 ilona.schwaiger@uni-ulm.de

Thomas Zwosta -2 60 36 thomas.zwosta@uni-ulm.de

* Is an alumnus of the Institute meanwhile

⁺ Currently on parental leave

Preface

The preface of this year's Annual Report of the Institute of Optoelectronics starts with a personal detail: In Oct. 2015, after two and a half years as the Director of Corporate Research at Infineon Technologies in Munich and two full terms or twelve years as the President of Ulm University, Karl Joachim Ebeling has resumed his previous position as the Head of the Institute. Laser-based optical sensing is his main current research interest.

The VCSELs and Optical Interconnects Group has presented novel vertical-cavity surface-emitting lasers (VCSELs) with monolithically integrated phototransistors, which could render oxide-aperture-based current confinement unnecessary in future device generations, leading to easier manufacture and higher reliability. Remarkable hysteresis and negative differential resistance properties of the new lasers are found and studied in detail. We also investigate various methods to influence the birefringence in VCSEL cavities with the ultimate goal to use novel laser devices in spin optoelectronics in the 100 GHz frequency regime. The laser modeling for improved 28 Gbit/s VCSELs has been refined. A simplified and accurate method to extract the thermal resistance from temperature-dependent continuous-wave output data of VCSELs has been devised.

After more than 7 years, our DFG transregional research group "PolarCoN" about studies on semipolar GaN structures has come to an end in 2015, leading to a bunch of final publications (many of them are printed in January 2016, hence not yet listed in this Annual Report). Although excellent results have been obtained, these studies will not be directly continued. Instead, our studies about opto-chemical sensors are carried on with even increased importance. The close cooperation with bio-chemists of our university helps us to step into life-science applications. On the other hand, we have started new activities towards AlGaIn heterostructures which may find their application in deep-UV light emitting diodes.

In the High-Power Semiconductor Laser Group, a quantum-well-pumped semiconductor laser has been realized, which emits two wavelengths (957 nm and 998 nm) simultaneously and additionally allows to switch between these at continuous output powers of more than 10 W.

Karl Joachim Ebeling
Rainer Michalzik
Ferdinand Scholz
Peter Unger

Ulm, March 2016

Quantum-Well-Pumped Semiconductor Disk Lasers for Single- and Dual-Wavelength Emission

Markus Polanik

We present two quantum-well-pumped semiconductor disk lasers having identical epitaxial layer sequences, besides different resonance wavelengths. One shows an output power exceeding 16 W at a wavelength of 982.6 nm, although mounted on a copper heat sink. The other disk laser emits light with wavelengths of 960.8 nm and 997.5 nm simultaneously. Dual-wavelength emission was detected in a temperature range of 21.3–27.1 °C. The optical output power can be forced to switch from one longitudinal mode of the micro resonator to another, by changing the temperature T_{sink} of the laser heat sink. Output powers of 10.98 W at a wavelength of 957.0 nm ($T_{sink} = -15^\circ\text{C}$) and 10.24 W at a wavelength of 997.5 nm ($T_{sink} = 50^\circ\text{C}$) were measured. Thermal rollover was not seen, the limiting factor was the available maximum pump power. At a pump wavelength of 940 nm, quantum defects below 1.8 % have been obtained.

1. Introduction

Semiconductor disk lasers combine two major advantages of semiconductor lasers and solid-state thin-disk lasers in a single device. The result is a semiconductor laser having both, a high output power and a good beam quality [1]. A versatile wavelength range from the ultraviolet to the infrared can be covered with semiconductor devices by changing the material composition and the epitaxial layer sequence of the device [2]. The external out-coupling mirror allows the use of intra-cavity devices, e.g. etalons, birefringent filters, or nonlinear crystals. Dual-wavelength emission from a single laser disk can be forced by placing an etalon inside the cavity of the laser [3]. However, if a wide distance between the two simultaneously emitting wavelengths is required, a special laser design becomes mandatory [4]. Switching between two emission wavelengths can be realized, for instance, by a variation of the pump power [5]. In our approach, wavelength switching is realized by a change of the laser heat-sink temperature. Furthermore, we evaluate the output characteristics of two disk lasers having the same epitaxial layer sequence but with different resonance wavelengths of the internal cavities. One of them shows dual-wavelength emission at room temperature. Obtaining semiconductor chips with different resonance wavelengths from a single wafer is possible due to the decrease of the layer thicknesses from the middle to the edge of the wafer. Since the emission wavelength of a disk laser is given by the resonance wavelength of the micro cavity, a broad wavelength range of 955 to 1000 nm can be selected with laser chips from the same wafer [6]. The reduced amount of heat generated inside the active region of quantum-well-pumped lasers allows high output powers even if the gain-spectrum peak at room temperature has a larger wavelength

than the emission wavelength. In conventional barrier-pumped lasers, the amount of heat generated inside the active region is significantly larger than in quantum-well-pumped lasers and therefore the temperature-dependent shifts of emission wavelength and gain spectrum are more critical. For barrier pumped lasers at high output powers, a detuning of 25 nm at room temperature between these two wavelengths is recommended, because of the four to five times faster temperature-dependent shift of the gain peak compared to the shift in the emission wavelength. Even with the use of diamond heat spreaders and/or intra-cavity heat spreaders, it is impossible to keep the laser at the desired temperature, at high output powers [7]. Thermal rollover is therefore the main reason for the limited output power of semiconductor disk lasers [2].

Quantum well pumping allows to diminish the generated heat inside the active region by reducing the difference between the emission wavelength and the pump wavelength, also known as quantum defect. The smallest quantum defect we measured so far was 1.55 % for a laser with an emission wavelength of 954.8 nm and a pump wavelength of 940 nm. Thermal rollover isn't a large problem with these devices, the problem is the small absorption rate of the pump power which is often below 35 %. The pump absorption of quantum-well-pumped lasers, like the name indicates, solely takes place in the quantum wells. This is disadvantage compared to barrier-pumped disk lasers, where the pump absorption can be controlled by the thickness of the barriers and is independent of the number of quantum wells. Hence, a high absorption rate is much easier realizable with barrier pumped lasers. Nearly all barrier-pumped laser designs allow an absorption rate above 90 %. To achieve the same absorption rate with quantum-well-pumped lasers, a multipass optic is required. With a simple setup containing a parabolic mirror and two prisms acting as retro reflectors, a multipass optic can be realized, which allows three double passes of the pump radiation through the disk. This setup is already sufficient to achieve an absorption rate of the pump power, close to 80 %, from the quantum-well-pumped disk laser design presented here [6].

2. Laser Design and Fabrication

The layer design of the quantum-well-pumped laser is visualized in Fig. 1. A resonant design for the emission and pump wavelength was chosen. The eight double quantum wells are placed inside the active region at the anti nodes of the emission field. Because of the wavelength difference between the emission and the pump wavelength, the field intensities drift apart inside the device. Therefore, a 1.2 μm long GaAs spacer is grown after the first four double quantum wells, since a quantum well placed inside a node of the pump field isn't able to provide any gain to the laser field [8].

Both sides of the active region are terminated by a AlAs/GaAs Bragg mirror. The top mirror contains 3.5 pairs and the bottom mirror consists of 18.5 pairs. A dielectric coating is sputter deposited onto the last bottom mirror facet, before a metalization is evaporated onto the wafer. The purpose of this coating is to achieve a reflectivity over 99.95 % for the emission wavelength at the bottom of the device. A dielectric coating is also placed onto the surface of the device, acting as an anti-reflection (AR) coating. Additional information about the fabrication of the quantum-well-pumped disk lasers can be found in [9].

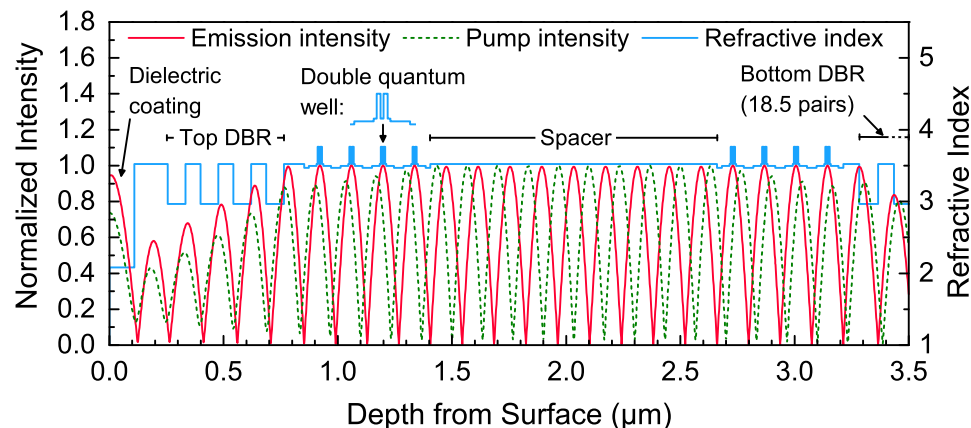


Fig. 1: Structure of the disk laser visualized in terms of the refractive index. Plotted are the calculated field intensities of the laser and pump fields (TE-component). Only one layer pair of the bottom Bragg mirror is displayed. On the top of the semiconductor device a dielectric coating is applied.

The flip-chip technique allows the complete removal of the substrate after the laser disk is mounted onto a heat sink. Since the design wavelength of 980 nm and the intended pump wavelength of 940 nm are larger than the absorption wavelength of GaAs. Laser emission is also possible without removing the GaAs substrate at the top of the laser, but even with undoped substrate, a small absorption in the substrate was still present and output powers over 1 W required a strong cooling of the device [6]. To conclude, removing the substrate for high power operation is still necessary.

3. Reflectivity Spectra

Measuring the reflectivity spectra of a disk lasers allows to determine a few important properties of the device, e.g., the positions of the resonance wavelength and the exciton absorption. Varying the detection angle from 10 to 70°, the resonance wavelengths experience cosine shifts to the small wavelengths, while the excitonic dip stays at one position [10]. The two diagrams on the left-hand side of Fig. 2 show the result of such a measurement.

At a distance of $r = 10.5$ mm from the middle of the wafer, the resonance wavelengths are located at 910, 945 and 980 nm. Only the first two resonance wavelengths are visible at a detection angle of 10°, due to lack of absorption of the quantum films at larger wavelengths. Measured at a distance of $r = 5.5$ mm, a shift of the resonance wavelength of 13 nm is noticeable. The approximate position of the excitonic dip only changed by 6 nm.

In our experiments, we use a wavelength-stabilized pump laser with a wavelength of 940 nm. For a good absorption rate of the pump power, it is important that the emission of the pump laser hits a resonance wavelength of the micro cavity. It is therefore necessary to pump the chips under a certain angle. In the case of the disk laser with $r = 10.5$ mm, a pump angle around 35° is favorable. However, a shift of the resonance wavelength

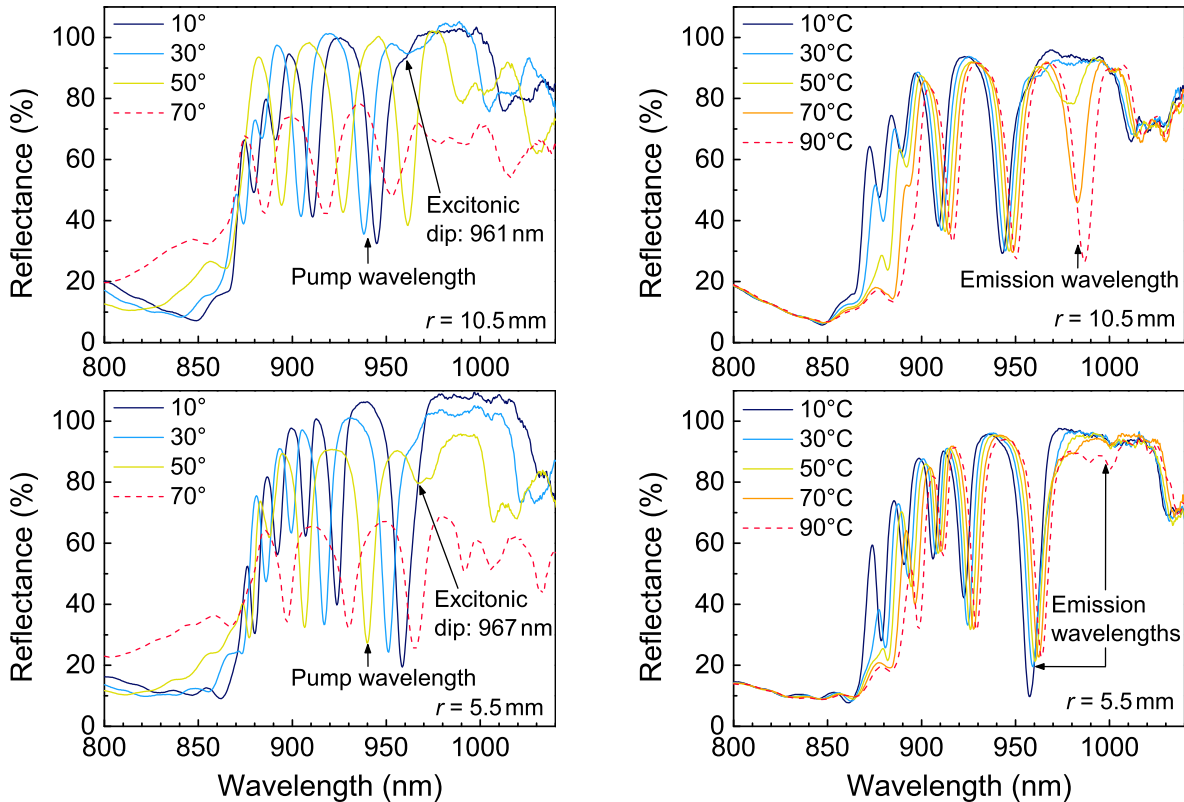


Fig. 2: Measured reflectivity spectra of two disk lasers from the same wafer. The two lasers have a different distance from the center of the wafer r , which causes a shift of the resonance wavelengths. Only the device with $r = 5.5$ mm is capable of dual-wavelength emission at room temperature. The left diagrams show the dependency of the reflectivity spectra from the detection angle and the diagrams on the right side show the dependency of the spectra from the temperature.

will occur if the temperature of the device changes. This is visible in the diagrams on the right-hand side of Fig. 2. The temperature-dependent spectra were measured at a detection angle of 10° and temperatures from 10 to 90°C . For the resonance wavelength, a shift of 0.09 nm/K can be calculated and the wavelength shift due to the shrinkage of the bandgap with rising temperature is 0.32 nm/K . The dependency of the bandgap size on the temperature is clearly visible in the range of 865 to 890 nm, in the measured temperature-dependent reflectivity spectra. Only the device with $r = 5.5$ mm is capable of dual-wavelength emission at room temperature. To force the other disk laser into lasing at the smaller resonance wavelength at 958 nm, subzero temperatures are necessary. We therefore only examined the single-wavelength emission of this device.

4. Single-Wavelength Emission

In this measurement, we demonstrate the capabilities of the used quantum-well-pumped disk laser design. As shown in Fig. 3 we have characterized one of the disk lasers for different pump angles to determine the optimum direction of the pump-laser beam. For

these measurements, the chip already mentioned in the previous chapter coming from a position of $r = 10.5$ mm on the wafer, was mounted on a copper heat sink. A wavelength-stabilized pump laser emitting at 940 nm is focused under angles of 17, 23, 27 or 35° onto the chip. The temperature of the laser is controlled by a temperature sensor on the heat sinks and a Peltier cooler. The backside of the Peltier device is water cooled. All measurements were performed at a heat-sink temperature of 0 °C and with an out-coupling mirror reflectivity of 96 %.

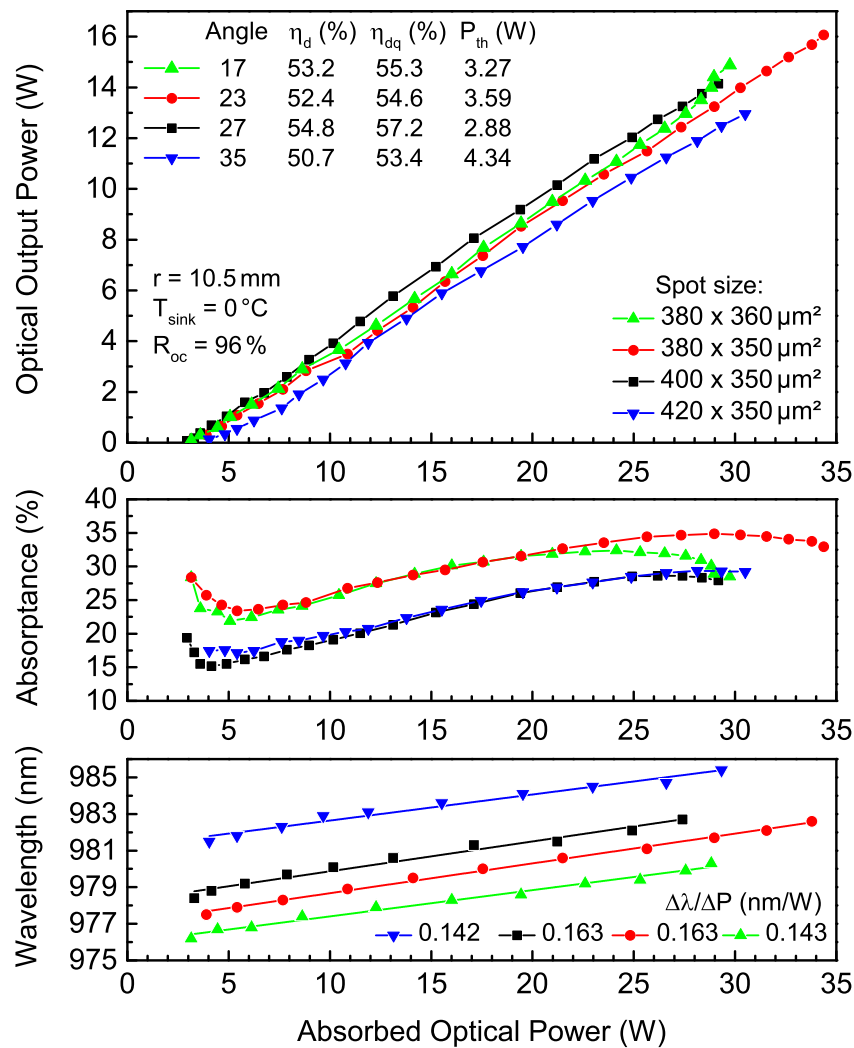


Fig. 3: Output characteristics of a quantum-well-pumped semiconductor disk laser pumped with a wavelength of 940 nm. The measurements were taken at four different pump angles.

During the measurements under a pump angle of 23° , the highest output powers up to 16.07 W were obtained. The measured optical output for all four pump angles was limited by the highest available pump power of 104 W. No indication of thermal rollover was observed. The values of the differential efficiency are between 50.7 and 54.8%. The highest absorption rate of the pump power with 34.8%, was measured at an angle of 23° , while 29 W of the pump power is absorbed. A small decrease in the pump absorptance is noticeable at higher pump powers, likely caused by the temperature raise of the disk with increasing pump power. The highest shift of the resonance wavelength with increasing absorption power is 0.163 nm/K. Typically, the wavelength shift of barrier-pumped disk lasers is slightly larger.

A dependency of the emission wavelength on the pump angle can be observed. Choosing a larger pump angle results in a longer emission wavelength. The explanation for this behavior is simple: When changing the pump angle, the setup is readjusted for maximum output power also by finding a optimum position for the pump spot on the laser chip. Since the output power for all pumping angles is limited by the pump power, the highest output power is observed at the position on the chip, where the highest pump absorption takes place, resulting in a different emission wavelength.

5. Switching Between Longitudinal Modes

A change in the lasers heat sink temperature causes the gain peak to shift with 0.33 nm/K. Lasing favorably occurs at the longitudinal mode which is closest to the gain peak. Since the resonance wavelength only shifts with 0.07 nm/K, a switch between two longitudinal laser modes can be realized by changing the laser temperature. The problem of a temperature-induced longitudinal mode switching is the incidental shift of the resonance wavelengths of the micro cavity. A temperature change therefore always has an impact on the pump absorption rate at a fixed pump wavelength. Some output characteristics of a disk laser for dual-wavelength emission are summarized in Fig. 4, showing the optical output power, the absorbed optical power, and the measured emission wavelength of the laser at different temperatures of the heat sink and at different pump angles. In this measurement, the quantum-well-pumped disk laser with $r = 10.5$ mm is used. This particular chip is mounted on a diamond heat spreader. However, similar results can be obtained with copper-mounted chips as well [6].

An output power of 10.24 W is possible, while the temperature of the heat sink is set to 50°C . The pump absorption stays constant at about 30% during the whole measurement and the wavelength shifts with 0.082 nm/K. A change of the heat-sink temperature of $\pm 50^\circ\text{C}$ is causing a bisection of the pump absorption rate and in the case of the reduction of the temperature, a step in the emission wavelength from the longitudinal mode at 997.5 nm to the mode at 957.0 nm. For the measurement of the output characteristics at -15°C , the pump angle was reduced to 45° , so that a reasonable absorption rate of the pump power was guaranteed. At this heat-sink temperature, an output power of 10.98 W and the smallest threshold pump power with 2.91 W was measured. A differential efficiency of 57.3% was determined. The shift of the 957 nm long emission wavelength,

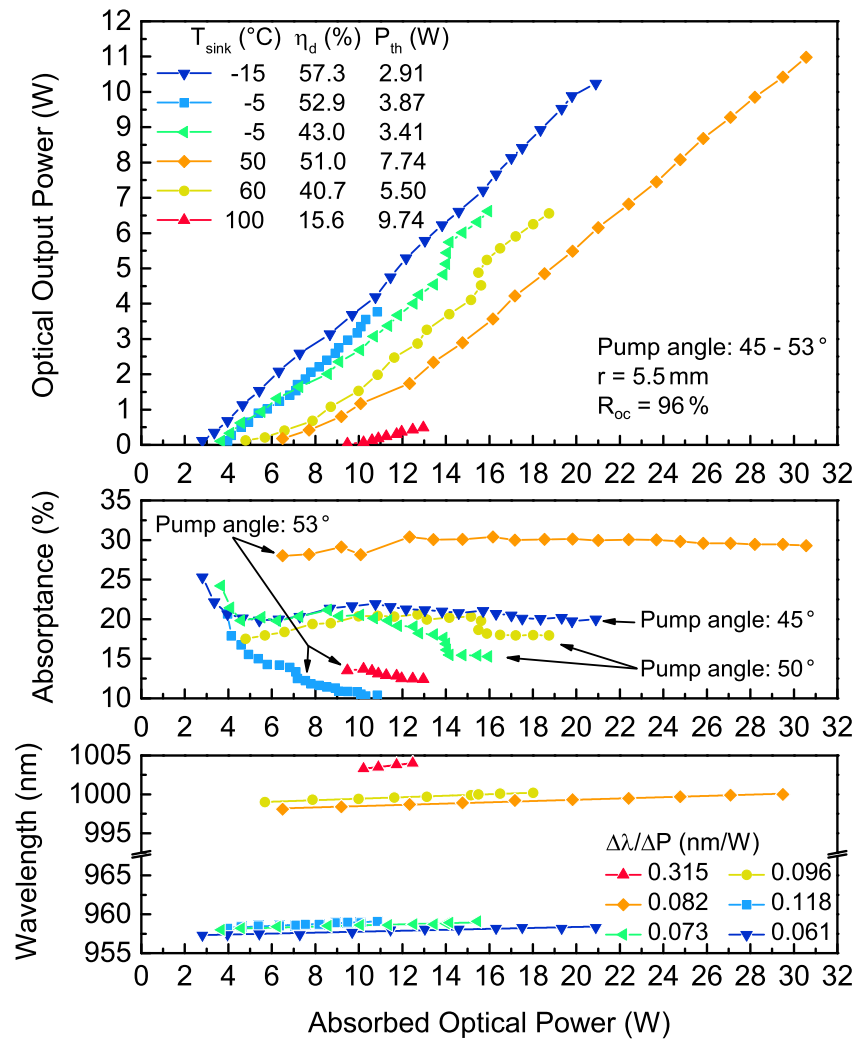


Fig. 4: Output characteristics of a quantum-well-pumped semiconductor disk laser, at a pump wavelength of 940 nm. The measurements were taken at five different temperatures and three different pump angles.

with absorbed optical power, only has a value of 0.061 nm/K, which is reasonable for a quantum defect under 1.8 %.

The measurements demonstrate, that a wavelength switch can be induced by a change of the laser temperature and that thermal rollover is successfully avoided because of the declining pump absorption rate at high pump powers. This behavior is mainly caused by the red shifting resonance.

The temperature dependency of the optical output power and the absorption rate is shown in Fig. 5. The disk laser was adjusted for maximum output power at a heat-sink temperature of 50 °C. Then, without readjusting or changing the pump power, the heat-sink temperature was changed. The used pump power during this measurement was 104 W. Raising the laser heat-sink temperature above 50 °C caused a quick decline of the output power and of the pump absorption. A similar behavior is seen while decreasing

the temperature below $50\text{ }^{\circ}\text{C}$, until a temperature of $25\text{ }^{\circ}\text{C}$ is reached. In the temperature range from 25 to $40\text{ }^{\circ}\text{C}$, a constant change of the pump absorptance with $0.681\text{ }^{\circ}\text{C}^{-1}$ can be observed. At a temperature of the heat-sink below $21.3\text{ }^{\circ}\text{C}$, the laser stops emitting at 997.5 nm and only emits at 960.8 nm . The optical output power measurement shows a clear kink while the temperature induced wavelength switch occurs. A small kink can also be noticed in the behavior of the pump absorptance at the wavelength switch. A change of the heat-sink temperature, while the device is lasing at the smaller wavelength, induced an absorption rate change of $0.295\text{ }^{\circ}\text{C}^{-1}$. Below $-10\text{ }^{\circ}\text{C}$ humidity is freezing on the chip surface preventing further measurements.

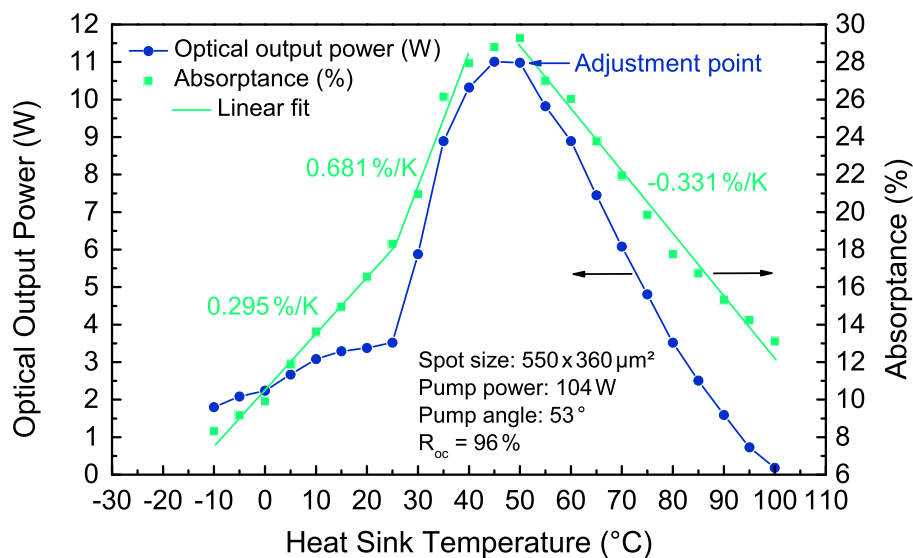


Fig. 5: Optical output power and pump power absorptance over the temperature of the heat sink. The chip was adjusted at $50\text{ }^{\circ}\text{C}$ for maximum output power. While the temperature of the heat sink was varied, the pump power stayed constant at a value of 104 W .

6. Dual-Wavelength Emission

Dual-wavelength emission can be detected while the temperature of the heat sink is between 21.3 and $27.1\text{ }^{\circ}\text{C}$. The measured emission spectra at different temperatures of the heat sink are displayed in Fig. 6. The quantum-well-pumped disk laser has the same output power at both wavelengths at a temperature of the heat sink around $22.0\text{ }^{\circ}\text{C}$. The rising temperature causes a quick decrease of the output power of the smaller longitudinal mode. At a temperature above $27.1\text{ }^{\circ}\text{C}$ only the longer longitudinal mode can be detected. The opposite occurs at temperatures below $21.3\text{ }^{\circ}\text{C}$. The spectral widths of the measured spectra are quite small. Even at output powers larger than 10 W the FWHM (full width at half maximum) wavelength of the spectrum is below 1.1 nm . This makes this quantum-well-pumped laser design particular interesting for frequency doubling applications. Using a birefringent filter for narrowing the spectral width is no longer mandatory.

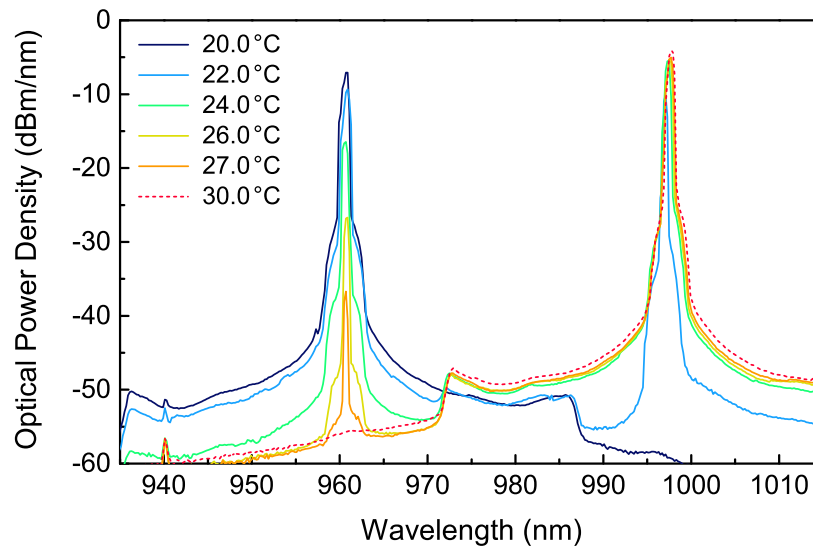


Fig. 6: Measured spectra of a quantum-well-pumped semiconductor disk laser at different temperatures of the heat sink. Dual-wavelength emission of the laser occurs at the wavelengths 960.8 and 997.5 nm, while the temperature of the heat sink is between 21.3 and 27.1 °C. The small peak at 940 nm is caused by the pump laser.

7. Conclusion

In this work we demonstrated the benefits of laser operation with low quantum defect, which was enabled by quantum-well pumping of the disk laser. A high output power exceeding 16 W was easily achievable, although no diamond heat spreader was used. The small spectral width of under 1.1 nm at high output powers will make the in-well pumped disk laser peculiar interesting for frequency-doubling applications. Furthermore, the emission wavelength can be easily switched from emitting at 957 nm to 998 nm just by changing the temperature of the lasers heat sink. A dual-wavelength emission with a distance between the emissions wavelengths of 36.7 nm is also possible without the use of intra-cavity elements.

8. Acknowledgment

These results wouldn't be possible without the previous work of my colleague Alexander Hein, the epitaxial growth of the laser material by Susanne Menzel and the assistance of Rudolf Rösch with chip processing and mechanical issues.

References

- [1] M. Kuznetsov, F. Hakimi, R. Sprague, and A. Mooradian, "Design and characteristics of high-power (>0.5-W CW) diode-pumped vertical-external-cavity surface-emitting semiconductor lasers with circular TEM₀₀ beams", *IEEE J. Select. Topics Quantum Electron.*, vol. 5, pp. 561–573, 1999.

- [2] O.G. Okhotnikov, *Semiconductor Disk Lasers: Physics and Technology*, Weinheim: WILEY-VCH Verlag, 2009.
- [3] L. Fan, M. Fallahi, J. Hader, A.R. Zakharian, J.V. Moloney, W. Stolz, S.W. Koch, R. Bedford, and J.T. Murray, “Linearly polarized dual-wavelength vertical-external-cavity surface-emitting laser”, *Appl. Phys. Lett.*, vol. 90, pp. 181124-1–3, 2007.
- [4] Y.A. Morozov, T. Leinonen, A. Harkonen, and M. Pessa, “Simultaneous dual-wavelength emission from vertical external-cavity surface-emitting laser: a numerical modeling”, *IEEE J. Quantum Electron.*, vol. 42, pp. 1055–1061, 2006.
- [5] J. Muszalski, A. Broda, A. Trajnerowicz, A. Wójcik-Jedlińska, R.P. Sarzała, M. Wasiak, P. Gutowski, I. Sankowska, J. Kubacka-Traczyk, and K. Gołaszewska-Malec, “Switchable double wavelength generating vertical external cavity surface-emitting laser”, *Optics Express*, vol. 22, pp. 6447–6452, 2014.
- [6] M. Polanik, *Charakterisierung von optisch quantenfilmgepumpten Halbleiterscheibenlasern mit kleinem Quantendefekt*, Master Thesis, Ulm University, Ulm, Germany, 2015.
- [7] P. Holl, M. Rattunde, S. Adler, S. Kaspar, W. Bronner, A. Bachle, R. Aidam, and J. Wagner, “Recent advances in power scaling of GaSb-based semiconductor disk lasers”, *IEEE J. Select. Topics Quantum Electron.*, vol. 21, pp. 324–335, 2015.
- [8] S.S. Beyertt, *Quantenfilm-Pumpen zur Leistungsskalierung von Halbleiter-Scheibenlasern*, Ph.D. Thesis, Stuttgart University, Stuttgart, Germany, 2010.
- [9] A. Hein and U. Brauch, “Optically in-well-pumped semiconductor disk laser with low quantum defect”, *Annual Report 2005*, pp. 69–76, Ulm University, Institute of Optoelectronics.
- [10] F. Demaria, *Schicht und Resonatordesign von Halbleiterscheibenlasern*, Ph.D. Thesis, Ulm University, Ulm, Germany, 2008.

VCSELs With Optically Controlled Current Confinement

Sven Bader

We present a concept for optically controlled current confinement in vertical-cavity surface-emitting lasers (VCSELs) based on the monolithic integration of a phototransistor. Omitting the usual oxide aperture improves the manufacturability and prevents built-in strain near the active zone. Measured continuous-wave operation characteristics of fabricated devices show hysteresis loops in the current–voltage and light–current curves or a negative differential resistance region. Requirements for the switch-on point of the laser are defined and explained.

1. Introduction

Vertical-cavity surface-emitting lasers are widely used in optical sensing and short-distance data communication [1]. Two major advantages of these devices compared to conventional edge-emitting laser diodes are low threshold currents and high conversion efficiencies at low output power. This requires high current densities in the close proximity of the active region via current confinement. Early demonstrations successfully used mesa etching [2] and proton implantation [3]. Epitaxial regrowth is an alternative method to produce current-blocking regions [4, 5].

The bulk of today’s commercial VCSELs relies on oxide confinement [1, 6], where excellent operation behavior is achieved. Using a wet-thermal oxidation process, AlGaAs layers of the top mirror with very high aluminum content are turned selectively into a non-conductive oxide and thus form buried apertures. A tight process control is required for reproducible results. During oxidation, the volume of the AlGaAs layers shrinks. Hence, strain near the active zone of the VCSEL is inevitable, which gives rise to concerns about the very-long-term reliability of the laser [7].

In order to avoid these disadvantages, we have developed a novel approach for current confinement [8]. In contrast to existing methods, the concept is based on the idea that the laser light beam itself should determine the current path through the device. Therefore a phototransistor (PT) is monolithically integrated close to the active region of the VCSEL. Only light-exposed PT areas allow current flow, whereas un- or underexposed regions form a current-blocking layer (Fig. 1). Hence, the PT works as an optical switch. This should result in an optically controlled enhancement of the current density distribution in close vicinity to the laser mode.

The article is organized as follows. Section 2 introduces the novel current confinement concept in some detail. Continuous-wave (cw) measurements of fabricated devices are presented in Sect. 3. A model of the turn-on behavior is presented in Sect. 4.

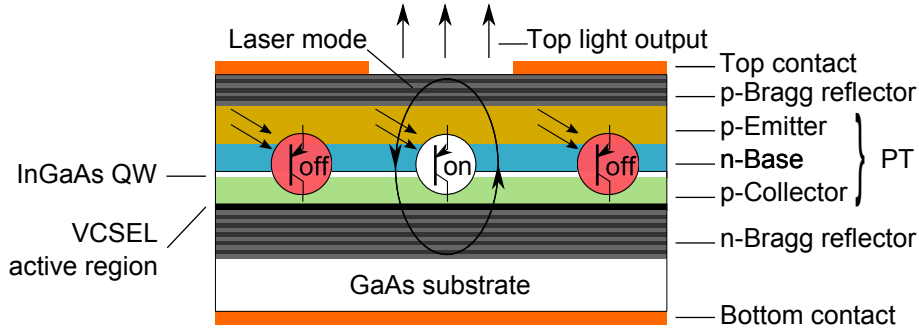


Fig. 1: Layout and operation principle of a top-emitting oxide-free PT-VCSEL with optically controlled current confinement. The integrated phototransistor, consisting of emitter, base, and collector layers, is configured as an optical switch. Areas exposed to the laser beam turn conductive, which results in a laterally defined current path.

2. Device Concept

Previous methods achieving current confinement in VCSELs manipulate the current flow with physical barriers which form non-conductive layers. In consequence, the laser beam is affected directly by the current path and will establish at areas with the highest current density. The concept presented here works oppositely. The photons of the VCSEL beam specify the current path, which entails an optical feedback. This is enabled by epitaxially integrating a PT on top of the active region of the VCSEL between the two Bragg reflectors (Fig. 1). In the standard configuration, the PT works similar to a bipolar transistor, here pnp-type, which means that it consists of p-emitter, n-base, and p-collector layers. In PTs, a photocurrent I_{ph} is generated by absorption of incident photons in the base-collector depletion zone. In the devices discussed below, for this task an InGaAs quantum well (QW) with defined width d and absorption coefficient α is embedded between base and collector. The photocurrent is equivalent to the base current $I_{\text{B,ph}}$ which controls the collector current flow through the device. Thus, no external base current is needed. The generated base current can be estimated accordingly as

$$I_{\text{B,ph}} \hat{=} I_{\text{ph}} = (1 - \exp(-\alpha d)) \cdot \frac{q\lambda}{hc} \cdot P \approx \alpha d \cdot \frac{q\lambda}{hc} \cdot P \quad (1)$$

like in a regular pin-type photodiode, where the approximation is valid for $\alpha d \ll 1$ (as in a QW). q is the elementary charge, h is Planck's constant, and c the vacuum velocity of light. Incident light emitted from the VCSEL's active region, with wavelength λ and power P in the cavity is responsible for $I_{\text{B,ph}}$, which means that the coupling between VCSEL and PT creates an optical feedback. The laser is driven by an external current I_0 , which can only flow in the light-exposed areas. There, the electrons of the photocurrent are swept directly through the n-doped base toward the p-emitter layer. Due to the charge neutrality of the base, the hole current I_0 flows through the device toward the collector. To reach this state, a certain amount of photons are required to satisfy the turn-on condition, which is introduced and explained in detail in Sect. 4. Un- or underexposed areas remain non-conductive when the optical power is too small and hence not able to switch the PT on. In this new concept, the lateral position of the laser beam cannot be influenced by

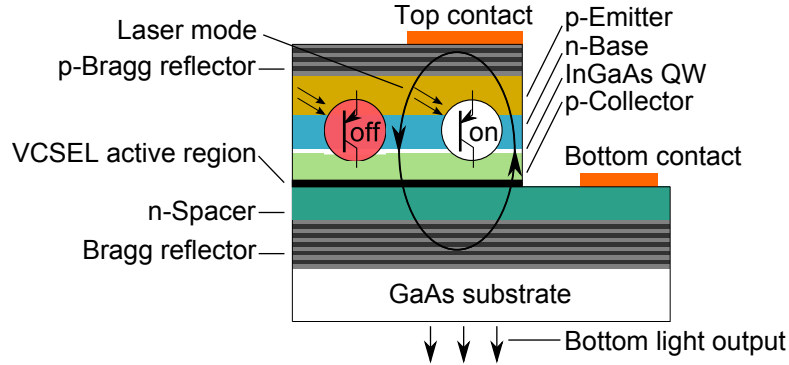


Fig. 2: Schematic layer structure of the investigated bottom-emitting PT-VCSEL.

just controlling the current path. Instead, the photons and hence the location of the laser mode must be manipulated directly by the quality of the resonator. The laser field will establish where the best cavity is found, as defined, e.g., by the top contact metal or a shallow surface relief [9]. As shown in Fig. 1, no transverse waveguiding is provided.

One-step epitaxial growth plus metal deposition can already produce a fully functional VCSEL. No mesa-etching and oxidation are required, which prevents the mentioned built-in strain near the active zone. The low additional structural complexity and the inherent light-to-current alignment give this device a strong potential to simplify the fabrication. The latter feature should also be beneficial for the conversion efficiency of such devices.

3. Characterization

3.1 Bottom-emitting PT-VCSEL

We have grown first test structures by molecular beam epitaxy. The schematic layer structure is depicted in Fig. 2. The active zone contains three InGaAs QWs for lasing operation at $\lambda = 1040$ nm. The PT layers are made of GaAs and are 255 nm thick. The 6 nm thick absorbing QW of the PT, embedded between the base and collector layer, has an absorption coefficient of ≈ 3500 cm⁻¹. The resonator is formed by 4 AlGaAs–GaAs-based top mirror pairs and 31.5 binary (AlAs–GaAs) mirror pairs of the bottom reflector with a simulated lossless reflectivity of $R_{\text{bottom}} = 99.99\%$. The VCSEL was processed for light output through the thicker mirror because the laser mode establishes under the top contact metal (Ti/Pt/Au) due to the increased top mirror reflectivity. The estimated threshold gains are 2750 cm⁻¹ (corresponding to $R_{\text{top}} = 99.3\%$) and ≈ 37000 cm⁻¹ ($R_{\text{top}} = 74.6\%$) with and without the metal, respectively.

Figure 3 (a) shows the measured light–current–voltage (LIV) characteristics of the PT-VCSEL bottom emitter when the current is ramped from 0 to 3.5 mA. Owing to this initial, non-ideal design, the optical output power is rather low. For very low input currents below 20 μ A (point A), the IV curve corresponds to the usual dark current ($I_{\text{B,ph}} = 0$) region of a PT, where the current results from the leakage current of the collector–base junction. Above 20 μ A the curve shows a negative differential resistance (NDR) behavior until

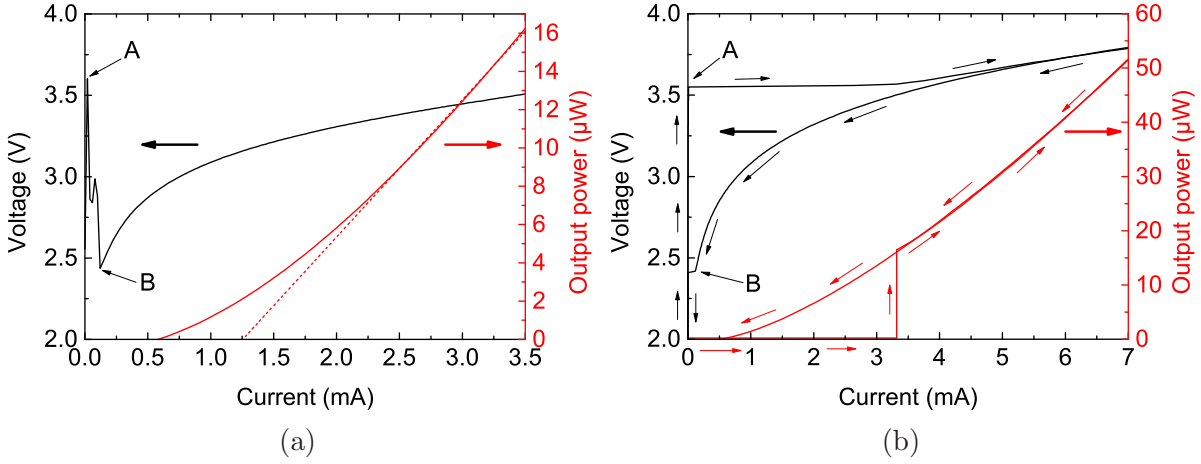


Fig. 3: Continuous-wave operation curves of the device from Fig. 2 when ramping (a) the current or (b) the voltage, which results either in an NDR region or a hysteresis loop. The operation points A and B are addressed in the text. The linear fit (dashed line in (a)) serves to estimate the threshold current.

120 μA (point B). At this point the PT switches on. A further current increase results in lasing operation above the threshold current $I_{\text{th}} = 1.26 \text{ mA}$. CCD camera observations qualitatively show that the positive curvature of the LI curve is caused by an expansion of the laser mode diameter since there is no built-in transverse waveguiding, in contrast to oxide-confined VCSELs. For PT-VCSELs a behavior similar to gain-guided VCSELs can be expected, with contributions from thermally induced index guiding. The current confinement in this device is thus rather weak.

Driving the PT-VCSEL with a voltage ramp, the switch-on/-off behavior changes into a hysteresis loop (Fig. 3 (b)). First, as for current ramping, the device is operated on the identical dark current curve. At 3.55 V (point A) the current increases suddenly to 3.32 mA and the device turns on. Once $I_{\text{B,ph}}$ flows through the device, the current rises in a positive feedback loop (more collector current induces more light emission in the QWs, which means more absorption in the PT and thus a higher $I_{\text{B,ph}}$) until reaching the stable state at the diode characteristic curve of the PT-VCSEL. Reducing the voltage, the laser remains on the diode curve (due to the already conductive base) until the PT turns off at 2.42 V with a remaining current of 120 μA (point B).

The LIV characteristics in Figs. 3 (a) and (b) differ only in the switch-on/-off mechanism of the PT. After leaving operation on the dark current curve due to $I_{\text{B,ph}} > 0$, the NDR region originates from an unstable state where not enough photons are available to switch the PT on. In contrast, while using a voltage source, the PT jumps directly to the on-state of the PT and the VCSEL. Ramping down from lasing operation, in both cases the LIV characteristics are identical up to the switching point of the PT. Using a current source the device enters the NDR region again, whereas with a voltage source the IV curve suddenly jumps to the dark current curve. Thus, this behavior results in a hysteresis loop.

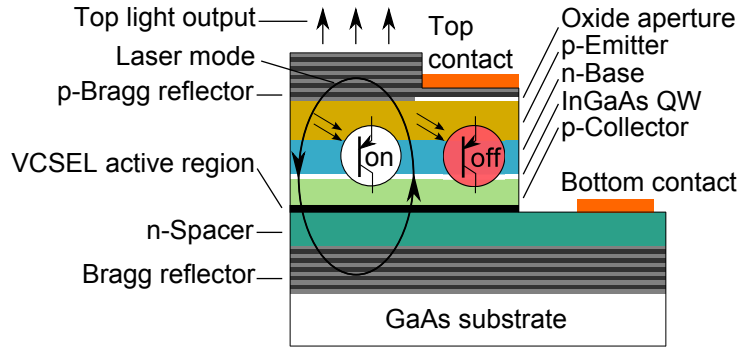


Fig. 4: Layer structure of the top-emitting PT-VCSEL. The oxidized aperture avoids laser operation under the top contact.

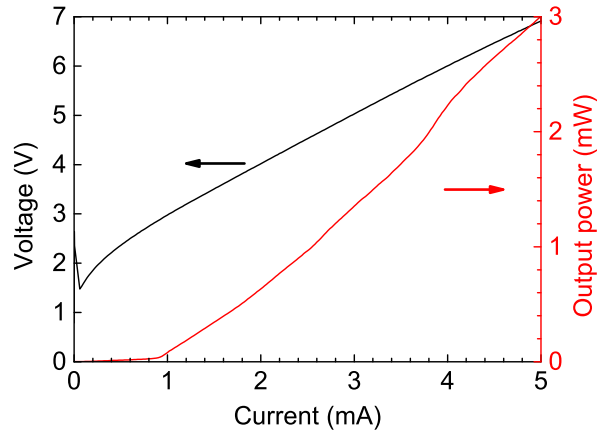


Fig. 5: LIV characteristics of the top-emitting PT-VCSEL with current ramping.

3.2 Top-emitting PT-VCSEL

In order to increase the optical output power, the device from Fig. 2 has been post-processed to create a top emitter (Fig. 4): First, we applied dielectric mirror layers which increase the top mirror reflectivity to 98.9%. Second, an oxide aperture with $9\ \mu\text{m}$ diameter was incorporated between the top mirror and the emitter layer. The oxide width was chosen according to the contact width to prevent lasing under the contact. The LIV characteristics are depicted in Fig. 5. The current was ramped from 0 to 5 mA.

As expected, the optical power of the device increases drastically to the mW range. The threshold current amounts to 0.90 mA. The average slope efficiency is about 0.77 W/A, which is 70 times higher than that of the bottom emitter. Lasing starts at the fundamental mode. With increasing current, higher-order modes begin to oscillate, which is visible as a kink in the LI curve at 3.7 mA. The NDR region at very low currents proves the functionality of the PT and hence its predicted influence on the current confinement. Nevertheless the current confinement is rather weak because the current aperture grows with increasing current. This can be improved by decreasing the photosensitivity of the PT. Raising the transparency of the InGaAs QW will enhance the slope efficiency in an improved design.

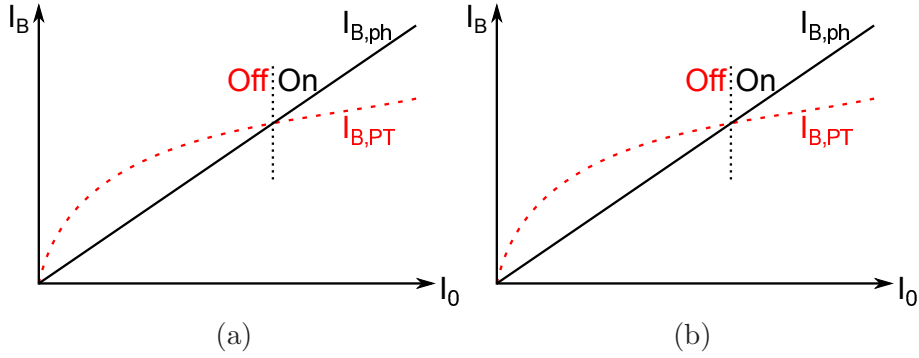


Fig. 6: Graphical illustration of the base photocurrent $I_{B,ph}$ and of $I_{B,PT}$ versus the laser current I_0 . The point of intersection defines the switching point of the PT determined by (a) the nonlinear shape of the gain curve of the PT at low currents in the μA -range and (b) the threshold current of the PT-VCSEL (mA-range). Operation according to (b) is desired for strong current confinement.

4. Turn-on Model

As mentioned in Sect. 3, the turn-on current and voltage largely define the current confinement functionality of the device. They depend on several parameters, namely the absorption coefficient α of the absorbing layer of the PT, its position in the standing-wave field in the cavity, as well as the current gain β_{PT} of the PT.

The latter determines the laser (or collector) current I_0 via the base current according to

$$I_0 = \beta_{PT} \cdot I_{B,PT}, \quad (2)$$

where $I_{B,PT}$ defines the base current which is needed to turn the PT on in order to allow I_0 to flow through the laser. If a current $I_0 < I_{th}$ is provided by a current source, spontaneous optical power P_{se} is generated in the active region of the VCSEL, where $P_{se} \propto I_0$ like in a light-emitting diode. Identifying $P = P_{se}$ we obtain $I_{B,ph} \propto \alpha d \cdot I_0$ from (1). Hence the base current $I_{B,ph}$, created by absorption, is not constant but depends linearly on I_0 . According to (2) this is also valid for $I_{B,PT}$. However, in a regular transistor β_{PT} turns out to be not constant while increasing I_0 , which directly affects the slope of $I_{B,PT}$ versus I_0 , as sketched in Fig. 6 (a). Low collector currents result in low current gains due to high recombination currents in the emitter–base depletion zone and interface and possibly surface leakage currents. This behavior is known and well explained in the literature using the so-called Gummel plot [10]. The PT switches to the on-state when $I_{B,ph} \geq I_{B,PT}$, which ensures the current flow I_0 through the laser. While increasing I_0 from the dark current curve ($I_{B,ph} = 0$) toward the turn-on point, the NDR region appears since the device transitions from an off-state with high voltage to a low-resistance on-state.

The turn-on point can be graphically determined by plotting $I_{B,ph}$ and $I_{B,PT}$ versus I_0 . The point of intersection of both lines defines the turn-on current where $I_{B,ph} = I_{B,PT}$ is satisfied. Due to the effect of the nonlinear β_{PT} at low I_0 , the point of intersection is located at low currents. However, if β_{PT} was constant, no such defined turn-on effect of the device would be expected. To achieve strong optically controlled current confinement, this point should be shifted to the threshold current I_{th} of the VCSEL. Otherwise, low currents,

respectively low optical powers, are sufficient to switch the PT on, which is likely to lead to a lateral broadening of the laser field when the evanescent tails of the laser mode(s) are able to open the PT. This corresponds to a weak current confinement, as seen in the experiments in Sects. 3.1 and 3.2. Figure 6 (b) depicts the desired operation. The PT should be in the off-state until I_{th} is reached. This could be achieved by reducing its current gain. Simultaneously, the PT should be designed to have a lower light sensitivity by decreasing the absorption coefficient of the InGaAs QW in the present design or by shifting its position towards a field node in the resonator. After finally reaching I_{th} , the amount of photons and hence $I_{\text{B,ph}}$ will rise strongly due to stimulated emission. This would lead to a turn-on point slightly beyond I_{th} (see Fig. 6 (b)) and therefore to strong optically controlled current confinement.

5. Conclusion

In summary, we have presented the concept of a novel oxide-free VCSEL with optically controlled current confinement induced by a monolithically integrated phototransistor next to the laser active region. First experiments give clear indications of the functionality of the transistor in both operation schemes: in current mode, a negative differential resistance region appears in the IV curve and in voltage mode, wide hysteresis loops establish both in the IV and LI curves. We have introduced a simple model to explain the occurrence of a distinct turn-on point of the PT-VCSEL. After the PT has turned-on, regular VCSEL behavior is found.

In the fabricated initial devices, the degree of current confinement is smaller than desired. This can be deduced from the continuous increase of the slope of the LI curve resulting from an expansion of the beam diameter, which is observed on qualitative images of the mode profile. The waveguiding properties of PT-VCSELs will be a topic of future studies. Also a noticeable voltage penalty is caused by the present design of the PT. We have indicated the routes to optimize these adverse effects, namely a higher transparency of the absorbing QW and a reduction of the PT's current gain. Implementing these, there is a strong potential to create a new kind of high-performance VCSELs with simplified fabrication and potentially superior reliability.

Acknowledgment

The author thanks Philips Technologie GmbH (U-L-M Photonics) for the MBE growth and the contributions to the processing of the PT-VCSELs. Furthermore the author is grateful to Dr.-Ing. Philipp Gerlach for the numerous helpful discussions and the food for thoughts. Also the author acknowledges the technical support of Susanne Menzel and Rudolf Rösch.

References

- [1] R. Michalzik (Ed.), *VCSELs — Fundamentals, Technology and Applications of Vertical-Cavity Surface-Emitting Lasers*, Springer Series in Optical Sciences, vol. 166. Berlin: Springer, 2013.
- [2] J.L. Jewell, A. Scherer, S.L. McCall, Y.H. Lee, S. Walker, J.P. Harbison, and L.T. Florez, “Low-threshold electrically pumped vertical-cavity surface-emitting micro-lasers”, *Electron. Lett.*, vol. 25, pp. 1123–1129, 1989.
- [3] M. Orenstein, A.C. Von Lehmen, C. Chang-Hasnain, N.G. Stoffel, J.P. Harbison, L.T. Florez, E. Clausen, and J.E. Jewell, “Vertical-cavity surface-emitting InGaAs/GaAs lasers with planar lateral definition”, *Appl. Phys. Lett.*, vol. 56, pp. 2384–2386, 1990.
- [4] M. Ortsiefer, W. Hofmann, J. Roskopf, and M.C. Amann, “Long-Wavelength VCSELs with Buried Tunnel Junction”, Chap. 10 in *VCSELs*, R. Michalzik (Ed.), pp. 321–351. Berlin: Springer, 2013.
- [5] X. Yang, M. Li, G. Zhao, Y. Zhang, S. Freisem, and D. Deppe, “Small-sized lithographic single-mode VCSELs with high power conversion efficiency”, *Proc. SPIE*, vol. 9381, pp. 93810R-1–6, 2015.
- [6] D.L. Huffaker, D.G. Deppe, K. Kumar, and T.J. Rogers, “Native-oxide defined ring contact for low threshold vertical-cavity lasers”, *Appl. Phys. Lett.*, vol. 65, pp. 97–99, 1994.
- [7] B.M. Hawkins, R.A. Hawthorne III, J.K. Guenter, J.A. Tatum, and J.R. Biard, “Reliability of various size oxide aperture VCSELs”, in *Proc. Electron. Comp. and Technol. Conf. (ECTC)*, vol. 52, pp. 540–550, 2002.
- [8] S. Bader, P. Gerlach, and R. Michalzik, “Novel oxide-free VCSEL with optically controlled current confinement”, *Europ. Conf. on Lasers and Electro-Optics, CLEO/Europe*, paper CB-2.6, one page, 2015.
- [9] H.J. Unold, S.W.Z. Mahmoud, R. Jäger, M. Grabherr, R. Michalzik, and K.J. Ebeling, “Large-area single-mode VCSELs and the self-aligned surface relief”, *IEEE J. Select. Topics Quantum Electron.*, vol. 7, pp. 386–392, 2001.
- [10] S.M. Sze, “Bipolar Transistors”, Chap. 3 in *Physics of Semiconductor Devices*, pp. 133–189, New York: John Wiley and Sons, 1981.

Simplified Determination of the Thermal Resistance of Vertical-Cavity Surface-Emitting Lasers

Markus Daubenschütz

We present a novel approach to determine the thermal resistance and the internal temperature of vertical-cavity surface-emitting lasers (VCSELs) based on easily accessible laser parameters. The described method does not use any empirical parameters or pulsed measurements that are often mentioned in literature. We explain how to determine the thermal resistance and show the computation of the internal temperature for any operation point. Furthermore the data evaluation can be used for characteristic parameter extraction that enables us to establish an isothermal modeling of the VCSEL operation curves.

1. Introduction

VCSELs are key optoelectronic devices for optical sensing and data communication in high-performance computing, data centers, and in-building networks [1, 2]. The performance of such lasers depends on numerous design parameters. To develop and optimize next-generation VCSELs with data rates of 28 Gbit/s and above [3, 4] or to enable new sensing applications, an accurate knowledge about current flow and heat generation inside the device is inevitable. High average internal temperatures T_i in the laser cavity are a major problem, causing, e.g., a drop in conversion efficiency and reduced lifetimes. For datacom VCSELs T_i easily rises since higher-speed lasers need higher currents to reach the required bandwidth. In general, VCSELs are often used in environments where active cooling is not permitted due to the involved power dissipation and cost. Different approaches have been demonstrated to decrease the internal temperature by a reduction of the thermal resistance [5, 6] or by minimizing the optical absorption [7] and series resistances [8]. To compare the impact of different designs, an accurate determination of T_i is required. An externally measurable parameter that is exclusively related to the temperature distribution inside the laser is the change of the resonance wavelength with temperature. For VCSELs with an emission wavelength in the 800–1000 nm range, a mode shift of $d\lambda/dT \approx 0.07$ nm/K [9] is found. This value can be used to estimate the temperature increase directly from the measured spectral red-shift. Another common method to compute T_i is the determination of the thermal resistance

$$R_{\text{Th}} = \frac{\Delta T}{\Delta P_{\text{diss}}}, \quad (1)$$

which relates the average temperature change ΔT in the laser cavity to a change ΔP_{diss} of the dissipated power. For this purpose, the VCSEL is typically driven with electrical

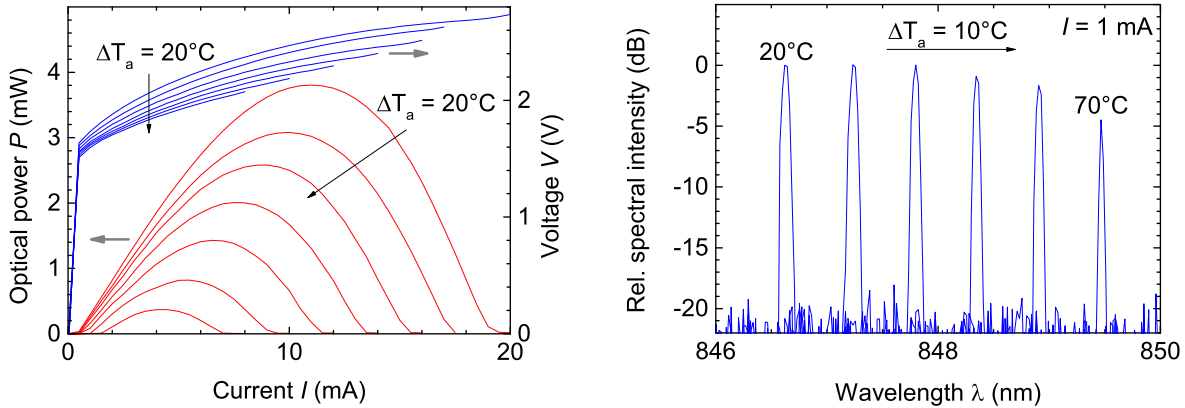


Fig. 1: Temperature-dependent light–current–voltage characteristics of a VCSEL with an active diameter $D_{ac} = 4\ \mu\text{m}$ for $T_a = 0^\circ\text{C}$ to 120°C in steps of 20°C (left) and optical spectra of the same laser at different T_a and $I = 1\ \text{mA}$ current (right).

pulses up to a few hundred nanoseconds [10], namely shorter than the thermal time constant which is in the range of some microseconds [11]. With this method, no internal heating of the VCSEL by the dissipated power arises and thereby no thermal wavelength shift appears. Pulsed operation thus allows to separate the influence of internal and external heating. The wavelength shift is then only induced by a change of the ambient temperature T_a . A series of such measurements results in the above-mentioned $d\lambda/dT$. As will be seen later, the VCSEL behaves differently for uniform heating and for internal heating by a dissipated power density profile. The drawback of pulsed measurements is the need for high-speed equipment. In this article we briefly describe the thermal influence on the laser characteristics and show the novel procedure of determining the thermal resistance and internal temperature. The analysis of T_i enables us to establish an isothermal model by which we can extract important static laser parameters dependent on the internal temperature.

2. Thermal Resistance

As can be seen in Fig. 1 (left), the operation curves of a VCSEL or of a laser diode in general are highly temperature-dependent. They are influenced by the ambient temperature as well as the internal temperature, which is related to several different mechanisms of power dissipation [12]. The effects can be classified into linear power dissipation (absorption, carrier thermalization, carrier leakage, and spontaneous carrier recombination) and quadratic power dissipation across the series resistance [13]. An increase of the internal temperature T_i leads to a change of different internal parameters that result in the case of Fig. 1 in an increase of the threshold current I_{th} , a decrease of the slope efficiency SE, and reductions of the kink voltage V_k and the differential resistance $R_d = dV/dI$. All of these changes are indirectly related to T_i and cannot be used to determine the internal temperature.

As mentioned before, one measurable parameter that exclusively depends on the temperature profile is the resonance wavelength λ of the VCSEL. With an increase of T_i or

T_a one observes a so-called red-shift of the emission spectrum to higher wavelengths, as displayed in Fig. 1 (right). The shift is induced by a temperature-related change of the refractive indices \bar{n} of the semiconductor materials and by the thermal expansion of the epitaxial layers and can be expressed as

$$\frac{1}{\lambda} \frac{d\lambda}{dT} = \frac{1}{\bar{n}} \frac{d\bar{n}}{dT} + \frac{1}{L} \frac{dL}{dT}, \quad (2)$$

which follows from the laser resonance condition. Both $d\bar{n}/dT > 0$ and $dL/dT > 0$. The second term on the right is more than an order of magnitude smaller than the first one.

The continuous-wave (cw) measurements of Fig. 1 were performed at wafer level on GaAs-based VCSELs with an operation wavelength close to 850 nm and varying active diameters D_{ac} . The active region of the VCSELs contains three GaAs quantum wells, and the top and bottom Bragg mirrors have 21 and 37.5 layer pairs, respectively. The LIV and spectral data were taken with a fully automated setup including a precise temperature-controlled wafer chuck. For a measurement range from -10 to 140°C the curves were recorded in steps of 5°C . The output power was measured with a calibrated Si photodiode housed in an integrating sphere. The spectral measurements were done with a grating spectrometer with wavelength steps of 22 pm, from which the measurable temperature resolution can be estimated as 0.3 K when $d\lambda/dT \approx 0.07$ nm/K.

The dissipated power needed for the determination of R_{Th} is defined as

$$P_{diss} = P_{el} - P = IV(1 - \eta_c) \quad (3)$$

with the electrical power P_{el} , the optical output power P , the injected current I , the voltage drop V over the VCSEL, and the conversion efficiency $\eta_c = P/P_{el}$. In Fig. 2 we show measurements of the peak wavelength λ_p of the fundamental LP_{01} mode over P_{diss} for the single-mode VCSEL from Fig. 1. One can clearly see a linear relation of λ_p and P_{diss} in the working range of the VCSEL for all ambient temperatures. This would also be true for higher-order transverse modes [14]. Nevertheless in the following we will restrict ourselves to the fundamental mode. In the analysis, this linear behavior of the mode shift versus P_{diss} is used to determine the thermal resistance R_{Th} of the laser. From (1) we can also write R_{Th} as [9]

$$R_{Th} = \frac{\Delta T}{\Delta P_{diss}} = \frac{\Delta\lambda/\Delta P_{diss}}{\Delta\lambda/\Delta T} = \frac{C_1}{C_2} \quad (4)$$

with the parameters $C_1 = \Delta\lambda/\Delta P_{diss}$ and $C_2 = \Delta\lambda/\Delta T$ for the wavelength shifts with dissipated power and ambient temperature, respectively. The parameter C_2 is mainly related to the change $d\bar{n}/dT$ of the refractive indices with temperature (see (2)) and — to avoid self-heating — must be determined with pulsed measurements or the aforementioned estimated value for $d\lambda/dT$. Our approach eliminates these difficulties or uncertainties in the following way: with simple linear extrapolations we can identify the wavelengths λ_0 of the LP_{01} mode without internal heating ($P_{diss} = 0$ mW) for all T_a . The data points correspond to the LP_{01} peak wavelengths of the laser in pulsed operation. The plot $\lambda_0 = \lambda_0(T_a)$ yields a linear relationship with a slope of $d\lambda_0/dT_a = 57$ pm/K, as shown in Fig. 3 (left). As expected, for the same epitaxial design we find the same slope for

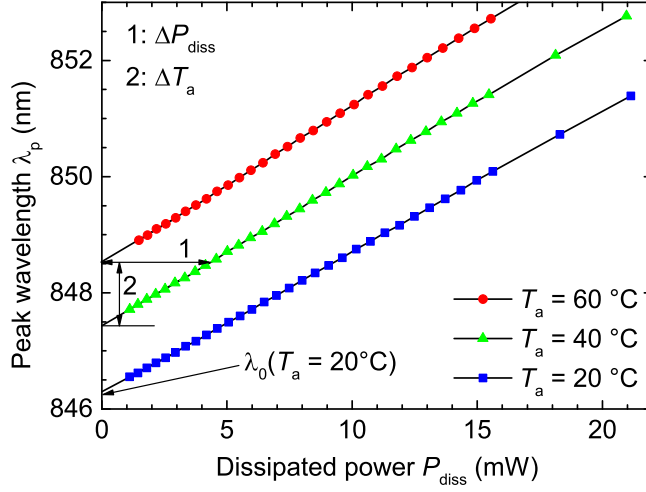


Fig. 2: Peak wavelength λ_p versus dissipated power P_{diss} for different ambient temperatures T_a . The labels ‘1’ and ‘2’ indicate the required changes of P_{diss} and T_a in (4).

all other values of D_{ac} . As can be seen in Fig. 2, λ_p increases linearly with P_{diss} , i.e., no curvature is seen even for high dissipated power. However, the slope of the straight lines increases with T_a . We find values of $d\lambda/dP_{\text{diss}} = 0.24 \text{ nm/mW}$ for $T_a = 20^\circ\text{C}$ to 0.32 nm/mW for 100°C . To deduce the thermal resistance in (4) we need associated values of ΔT and ΔP_{diss} . For our analysis we are using the fact that one gets the same emission wavelength for the same average internal temperature of the VCSEL, irrespective of T_a or P_{diss} being the origin. With the temperature-controlled wafer chuck we generate a $\Delta T = \Delta T_a$ that is labeled with ‘2’ in Fig. 2. The temperature increase results in a red-shift of λ_0 . For the initial ambient temperature, the same wavelength $\lambda_p = \lambda_0$ can also be achieved by internal heating. The necessary ΔP_{diss} to create this T_i is labeled with ‘1’ in Fig. 2. Because of the increasing slopes of the $\lambda_p = \lambda_p(P_{\text{diss}})$ curves with increasing T_a and the more homogeneous internal temperature profiles for small P_{diss} we have used temperature steps of only 5°C between the adjacent curves, in contrast to the 20°C step used for illustration in Fig. 2. If we now repeat the procedure for all adjacent curves we get thermal resistances for different T_a that are not constant due to the changing slope of the $\lambda_p = \lambda_p(P_{\text{diss}})$ curves. This is caused by decreasing thermal conductivities of the semiconductor layers with increasing temperature. If we plot the values of R_{Th} over T_a , as shown in Fig. 3 (right), we get again a linear behavior. The thermal resistance can thus be written as the sum

$$R_{\text{Th}} = R_{\text{Th}}(D_{\text{ac}}) + R_{\text{Th}}(T_a) \quad (5)$$

with the contribution $R_{\text{Th}}(D_{\text{ac}})$ depending on the semiconductor material and the active diameter and a thermal resistance

$$R_{\text{Th}}(T_a) = (T_a - T_{a0}) \cdot \frac{dR_{\text{Th}}}{dT_a} \quad (6)$$

depending on the ambient temperature, where $R_{\text{Th}}(D_{\text{ac}})$ is defined at the temperature $T_{a0} = 0^\circ\text{C}$. We find values of $R_{\text{Th}}(D_{\text{ac}})$ in the range of 4.54 K/mW to 3.02 K/mW and

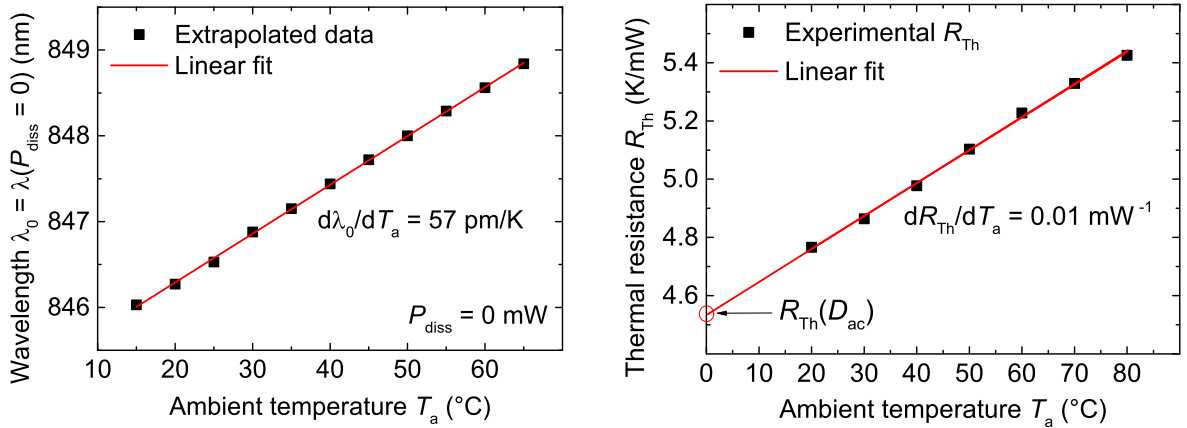


Fig. 3: Intrinsic wavelength λ_0 determined from linear curve fits for different ambient temperatures T_a (left) and extracted thermal resistance R_{Th} as a function of T_a (right).

dR_{Th}/dT_a from 0.0109 mW^{-1} to 0.0086 mW^{-1} for active diameters between 4 and 7 μm , respectively.

3. Isothermal Model

As shown in Sect. 2, the proposed analysis of the thermal resistance enables to extract the internal temperature for every point in a LIV curve. This gives the possibility to perform detailed analyses of the thermal effects and extract internal temperature-dependent VCSEL parameters. Furthermore one can also exclude internal heating in the examination of the LIV curves.

For this isothermal model we rearrange the measurement results in a new way. As shown in Fig. 4, we can determine the output power P as a function of T_i for each individual bias current. Similarly from the measured IV characteristic, $V = V(T_a)$ can be plotted for different I . With the help of these data we can now model the isothermal characteristic of the VCSEL for any T_i in the measured range of temperatures. The procedure is visualized in Fig. 4 for $T_i = 60^\circ\text{C}$. The temperature is kept constant and output powers are collected for every data point. It should be noted that a curve in Fig. 4 can be generated from the experimental data for every intermediate current I . The same procedure is repeated for the IV curve and a LIV diagram is plotted. As a result, in Fig. 5 we find perfectly linear characteristics which strongly deviate from the measured curves. The resulting isothermal LIV curves would be found experimentally for pulsed operation at an ambient temperature $T_a = T_i$. For $T_i = 60^\circ\text{C}$ in Fig. 5 we identify a kink voltage $V_k = 1.60 \text{ V}$ and a constant differential resistance $R_d = 109 \Omega$. The threshold current is $I_{\text{th}} = 0.45 \text{ mA}$ and the slope efficiency is $\text{SE} = 0.49 \text{ W/A}$. This kind of data evaluation enables us to extract the dependences of I_{th} , SE , V_k , and R_d on the internal temperature. These are plotted in Fig. 6 for the VCSEL with $D_{\text{ac}} = 4 \mu\text{m}$. The data points are fitted with polynomial functions. The threshold current shows a minimum value of $I_{\text{th,min}} = 0.24 \text{ mA}$ at $T_i = 5.24^\circ\text{C}$. The threshold minimum nearly corresponds to the maximum achievable slope efficiency $\text{SE}_{\text{max}} = 0.54 \text{ W/A}$. Both electrical parameters, namely V_k and R_d , decrease

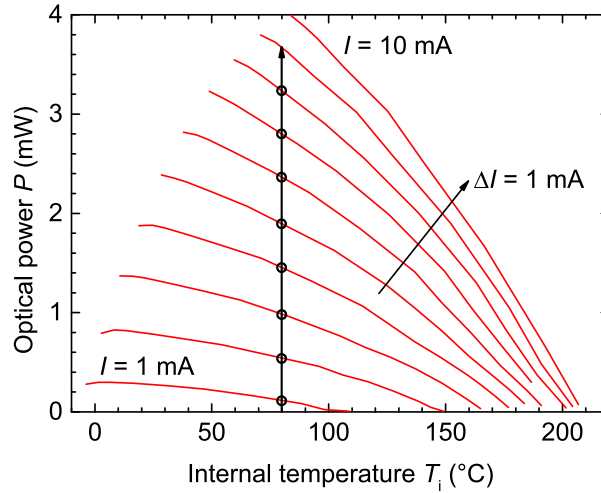


Fig. 4: Optical output power of the VCSEL from Fig. 1 versus internal temperature for different bias currents. The vertical arrow with the open bullets shows how an isothermal $P(I)$ curve is obtained for $T_i = 60^\circ\text{C}$.

with increasing T_i , as known from the experiment.

4. Conclusion

We have demonstrated a novel approach for the determination of the thermal resistance of vertical-cavity surface-emitting lasers. It is based on measured temperature-dependent continuous-wave light–current–voltage curves and corresponding optical spectra. The analysis requires no empirical data or pulsed measurements. The model allows to calculate the internal temperature at all operating points. Moreover we can simulate an isothermal operation of the VCSEL where the internal temperature is kept constant. As known

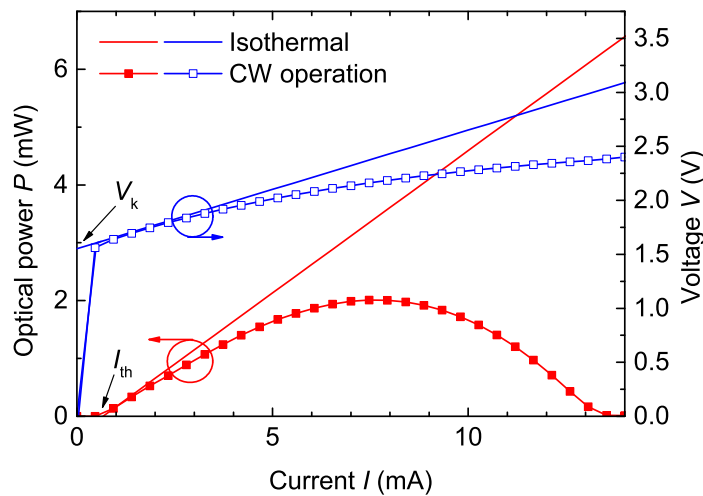


Fig. 5: Comparison of the measured cw output characteristics of a $4\ \mu\text{m}$ VCSEL and isothermal curves for an ambient temperature $T_a = 60^\circ\text{C}$.

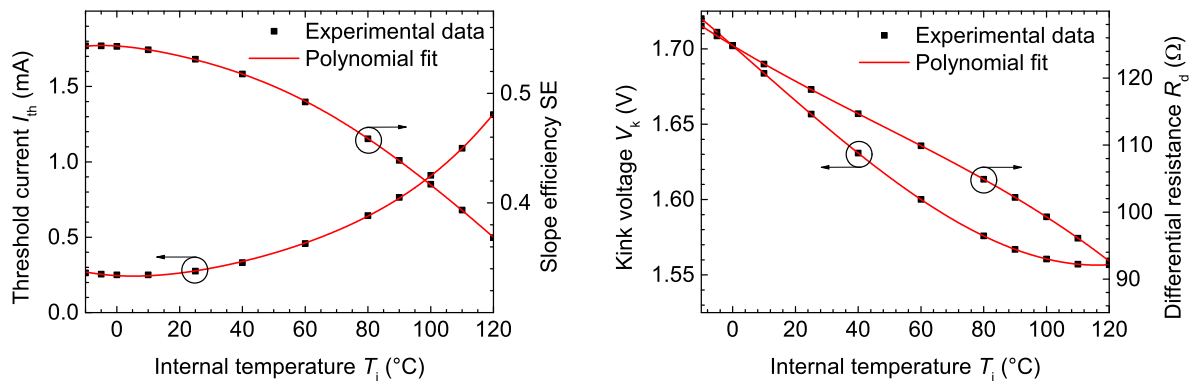


Fig. 6: Threshold current I_{th} and slope efficiency SE on the left as well as kink voltage V_k and differential resistance R_d on the right, all versus the internal temperature T_i .

from laser operation with short electrical pulses, we obtain perfectly linear light–current and current–voltage curves. At the same time, the temperature dependence of the four characteristic laser parameters, namely threshold current, slope efficiency, kink voltage, and differential resistance can be extracted.

Acknowledgment

We thank Philips Technologie GmbH, U-L-M Photonics, Germany for providing the VCSEL material and the measurement setup used in this study, Stefanie Unsel for the data evaluation within her master thesis, and the German Federal Ministry of Education and Research (BMBF) for funding the HyPOT project.

References

- [1] K. Jackson and C. Schow, “VCSEL-Based Transceiver for Data Communication,” Chap. 14 in *VCSELs*, R. Michalzik (Ed.), pp. 431–448, Springer, Berlin, 2013.
- [2] D. Kuchta, “Progress in VCSEL-Based Parallel Links,” Chap. 16 in *VCSELs*, R. Michalzik (Ed.), pp. 473–519, Springer, Berlin, 2013.
- [3] P. Westbergh, R. Safaisini, E. Haglund, J. Gustavsson, A. Larsson, M. Green, R. Lawrence, and A. Joel, “High-speed oxide confined 850 nm VCSELs operating error-free at 40 Gb/s up to 85°C,” *IEEE Photon. Technol. Lett.*, vol. 25, pp. 768–771, 2013.
- [4] D. Kuchta, A. Rylyakov, C. Schow, J. Proesel, C. Baks, P. Westbergh, J. Gustavsson, and A. Larsson, “64Gb/s transmission over 57m MMF using an NRZ modulated 850nm VCSEL,” *Optical Fiber Commun. Conf. (OFC) 2014*, Th3C.2. San Francisco, CA, USA, Mar. 2014.

-
- [5] D. Mathine, H. Nejad, D. Allee, R. Droopad, and G. Maracas, "Reduction of the thermal impedance of vertical-cavity surface-emitting lasers after integration with copper substrates," *Appl. Phys. Lett.*, vol. 69, pp. 463–464, 1996.
- [6] A. AL-Omari and K. Lear, "VCSEL with a self-aligned contact and copper-plated heatsink," *IEEE Photon. Technol. Lett.*, vol. 17, pp. 1767–1769, 2005.
- [7] P. Westbergh, J. Gustavsson, B. Kögel, Å. Haglund, and A. Larsson, "Impact of photon lifetime on high-speed VCSEL performance," *IEEE J. Select. Topics Quantum Electron.*, vol. 17, pp. 1603–1613, 2011.
- [8] K. Lear and R. Schneider Jr., "Uniparabolic mirror grating for vertical cavity surface emitting lasers," *Appl. Phys. Lett.*, vol. 67, pp. 605–607, 1996.
- [9] R. Michalzik, "VCSEL Fundamentals," Chap. 2 in *VCSELs*, R. Michalzik (Ed.), pp. 19–75, Springer, Berlin, 2013.
- [10] M. Dabbicco, V. Spagnolo, I. Catalano, and G. Scamarcio, "Direct measurement of the local temperature distribution in oxide VCSELs," in *Vertical-Cavity Surface-Emitting Lasers VI*, C. Lei and S. P. Kilcoyne (Eds.), Proc. SPIE 4649, pp. 62–70, 2002.
- [11] E. Kyriakis-Bitzaros and G. Halkias, "Thermal resistance evaluation of high-speed VCSEL: an isothermal optical transient technique," *IEEE Photon. Technol. Lett.*, vol. 14, pp. 269–271, 2002.
- [12] P. Debernardi, A. Kroner, F. Rinaldi, and R. Michalzik, "Surface relief versus standard VCSELs: a comparison between experimental and hot-cavity model results," *IEEE J. Select. Topics Quantum Electron.*, vol. 15, pp. 1603–1613, 2009.
- [13] P. Baveja, B. Kögel, P. Westbergh, J. Gustavsson, Å. Haglund, D. Maywar, G. Agrawal, and A. Larsson, "Assessment of VCSEL thermal rollover mechanisms from measurements and empirical modeling," *Optics Express*, vol. 19, pp. 15490–15505, 2011.
- [14] T. Flick, K. Becks, J. Dopke, P. Mättig, and P. Tegel, "Measurement of the thermal resistance of VCSEL devices," in *Topical Workshop on Electronics for Particle Physics 2010*, doi: 10.1088/1748-0221/6/01/C01021. Aachen, Germany, Sep. 2010.

New Approaches for Birefringence Tuning in Vertical-Cavity Surface-Emitting Lasers

Tobias Pusch

Using the elasto-optic effect we increase the frequency difference between the two orthogonally polarized modes, the so-called birefringence splitting, in standard single-mode oxide-confined GaAs-based vertical-cavity surface-emitting lasers (VCSELs). The birefringence may play an important role in the realization of ultrafast polarization modulation for high-speed data transmission. For practical implementation it is necessary to miniaturize the strain-inducing mechanism for birefringence tuning in VCSELs. The goal is the realization of integrated structures on the VCSEL chip. In this article we discuss our work on miniaturized bending devices as the next step in achieving extremely high birefringence splitting. Furthermore measurements with integrated hotspot structures on VCSEL chips were made to reach much smaller scales for birefringence fine-tuning.

1. Introduction

VCSELs are extensively used today as transmitters in high-speed optical interconnects. A first generation of 25 to 28 Gbit/s devices is currently being deployed. Although digital modulation at about 71 Gbit/s with transmitter equalization has been shown [1], it is not certain that 100 Gbit/s signals can be generated by direct current modulation. A potential alternative to direct intensity modulation might be found in the research on birefringence splitting, i.e., the frequency difference between the two orthogonally polarized components of a VCSEL mode. It has been demonstrated that by optical spin injection a birefringent VCSEL can be excited to oscillations in the degree of circular polarization [2]. Here the oscillation frequency is nearly equal to the birefringence splitting. The generation of extremely fast polarization bursts was shown as well [2]. Contributions to the birefringence are geometrical anisotropies, the electro-optic effect in the cavity, and incorporated strain [3]. Mechanically induced strain seems to be the most promising way. We have achieved a record-high birefringence splitting of more than 250 GHz via direct substrate bending [4]. As a next step, new miniaturized concepts for birefringence tuning have to be investigated.

2. Options for Miniaturized Mechanical Strain Incorporation

The maximum birefringence splitting of 259 GHz [4] has been reached by bending a $10 \times 10 \text{ mm}^2$ large VCSEL sample with the custom-made mount sketched in Fig. 1. The aim was to reach birefringence splittings of more than 100 GHz. We have found that values of 100–150 GHz are safely obtainable without sample failure. Based on this result, a much

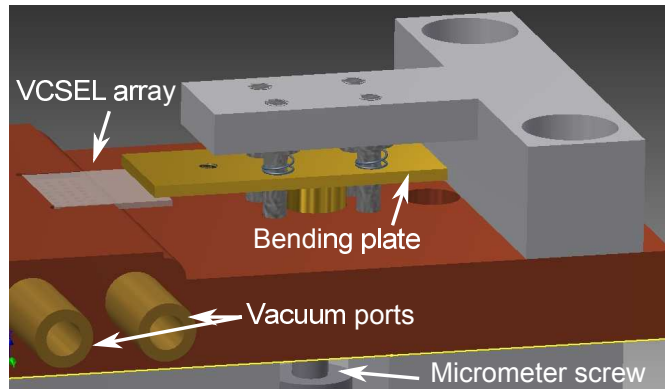


Fig. 1: Drawing of our first custom-made mount with bending plate and VCSEL array sample [4].

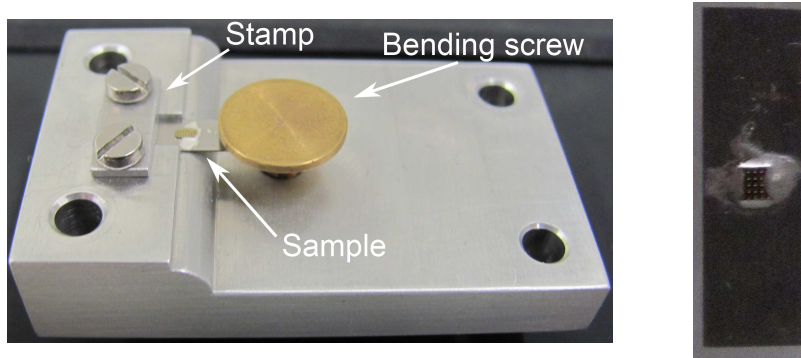


Fig. 2: Miniaturized second-generation bending device. A metal stripe with a glued VCSEL array is fixed in a recess via a stamp. Strain is induced indirectly in the VCSEL array by bending the free part of the metal stripe by movements of the screw (left). The VCSEL array is mounted with conductive glue on the $10 \times 4 \text{ mm}^2$ large metal stripe (right).

simpler miniaturized bending mount can be constructed. It is depicted in Fig. 2, together with a mounted sample.

In contrast to the mount in Fig. 1 we use indirect bending. The VCSEL array with a size of $1 \times 1 \text{ mm}^2$ is 100 times smaller than in the first bending device. The array is fixed on a metal stripe via conductive glue. The stripe itself is fixed on the left side by a stamp (see Fig. 2, left) and about half the area is free-standing. The position of the VCSEL array is close to the edge of the recess to achieve a maximum effect. We use a screw with a pitch of $350 \mu\text{m}$ to bend the metal stripe and thereby to induce strain indirectly in the VCSEL sample. The resulting optical spectrum for large bending is shown in Fig. 3 (left). With a value of 226 GHz we have reached a comparably high birefringence splitting as with the first bending device. The measurement was stopped here in order not to risk sample damage. Figure 3 (right) displays the light-current-voltage (LIV) curves of the investigated standard single-mode oxide-confined VCSEL with about $4 \mu\text{m}$ active diameter. The threshold current and voltage are 0.44 mA and 1.82 V , respectively. An optical output power of 1.0 mW is reached at about $I = 1.82 \text{ mA}$ current. The higher-order transverse mode is still suppressed by approximately 25 dB at $I = 2.1 \text{ mA}$.

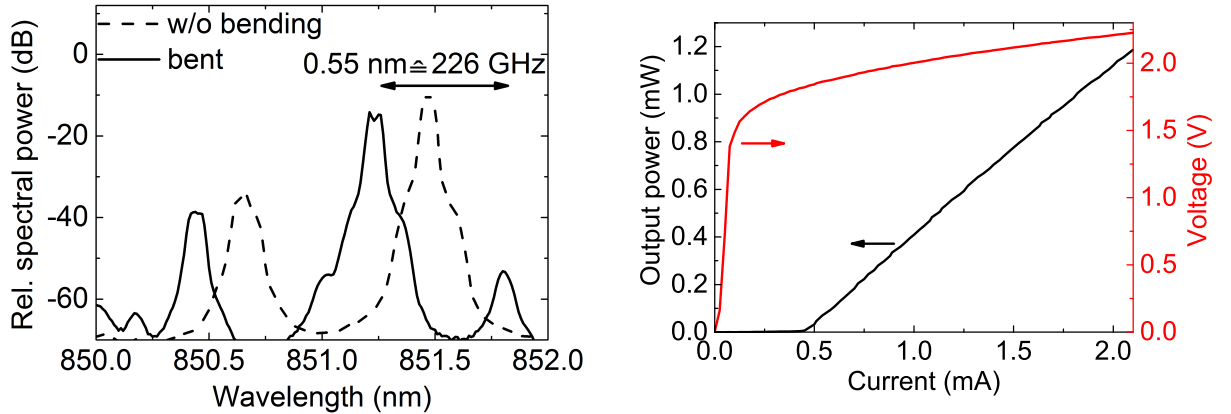


Fig. 3: Optical spectra without bending and with maximum applied bending of the metal stripe, measured at 2.1 mA (left). LIV characteristics at maximum bending (right).

3. Approaches to Thermal Birefringence Tuning

The ultimate miniaturization step is a birefringence tuning mechanism integrated on the VCSEL chip. At this level, mechanical bending seems impractical. Mechanisms for thermally induced strain are more simple to construct. Studies with an external heat source were made by Jansen van Doorn et al. [5,6] for birefringence tuning in VCSELs. In this case a Ti-sapphire laser beam was focused close to the VCSEL and the induced heat deformed the crystal structure. The change of birefringence (less than 3 GHz reversible [5] and 23 GHz with material ablation [6]) is substantially smaller compared to mechanical bending due to the much lower induced stress.

We have made alternative investigations using standard 850 nm oxide-confined single-mode VCSEL samples from Philips Technologie GmbH (U-L-M Photonics) which were partly post-processed. The first sample design comprises three VCSELs per unit cell, where one of them is a regular VCSEL structure. The other two are metalized on the surface and can be used as hotspots. We measure the optical spectra and the LIV curves for different current flow in one of the metalized VCSELs. The current in the lasing VCSEL is constant at $I = 2.1$ mA. A photograph of the device and measured optical spectra for different tuning currents are depicted in Fig. 4. The spectra show a red-shift of the fundamental mode as a result of a temperature increase in the lasing VCSEL. However, no increase of the birefringence splitting is seen. With an estimated wavelength shift rate of 0.07 nm/K [7] we get a temperature increase in the lasing VCSEL of about $\Delta T = 2.4$ K. The main problem is visible in Fig. 4 (left). The distance of 75 μm between the lasing VCSEL and the heat-inducing metalized VCSEL is simply too large. In other words, the thermal cross-resistance $R_{\text{Th,X}} = \Delta T / P_{\text{diss}} = 2.4 \text{ K} / (3.51 \text{ V} \cdot 10 \text{ mA}) = 0.068 \text{ K/mW}$ is very low owing to a thick (thermally insulating) polyimide layer employed for sample planarization. We get a slightly improved result of $\Delta T = 2.9$ K from a second measurement with the nearest-neighbor (68 μm distance) VCSEL of Fig. 4 (left).

The second investigated sample has been post-processed in the cleanroom. We have placed a 120 nm thick nickel line in the vicinity of the VCSEL to potentially increase the thermal cross-resistance. As in the first case of Fig. 4 we have measured the LIV curves and

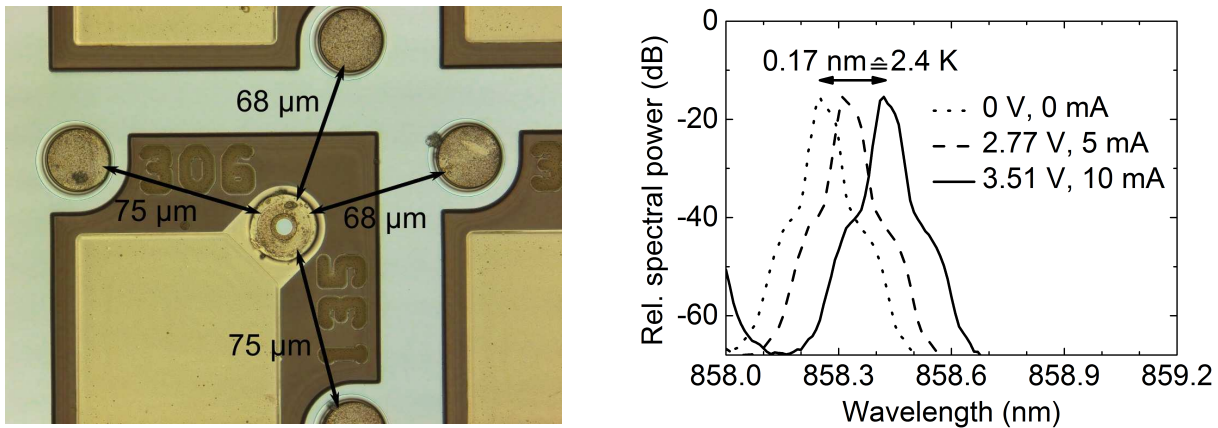


Fig. 4: Photograph of a sample with three VCSELs per unit cell. The distances between the lasing VCSEL and the metalized heating VCSELs are indicated (left). Optical spectra for different heating currents in a 75 μm distance metalized VCSEL (right).

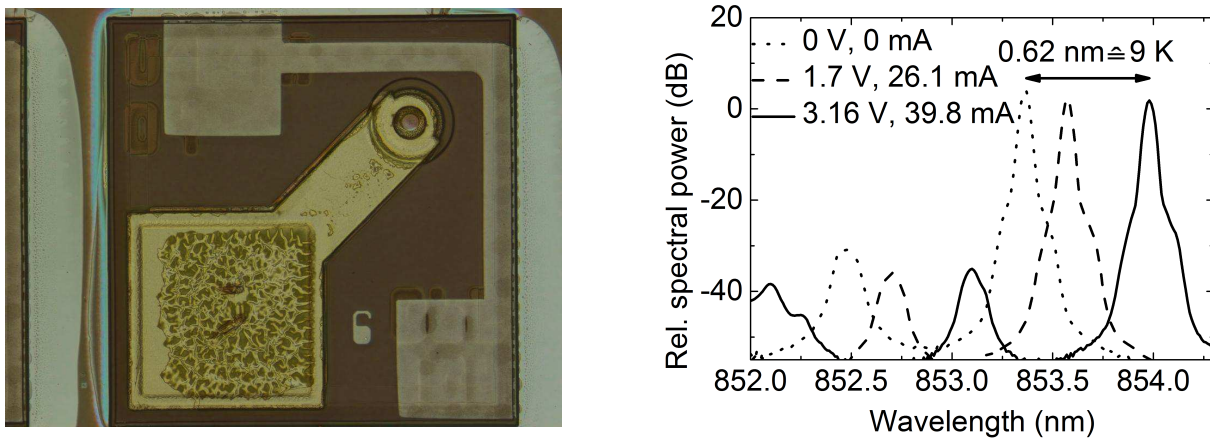


Fig. 5: Post-processed VCSEL sample with a nickel heating line (left). Optical spectra for different heating currents are shown on the right.

optical spectra for different currents in the nickel line. A photograph of the sample and measured optical spectra are shown in Fig. 5. The laser current is $I = 2.5 \text{ mA}$. Every unit cell is surrounded by large trenches. For that reason it was not possible to run a straight heating line across unit cells. Instead, the line and both bondpads had to be confined in one unit cell, which resulted in a non-ideal geometry of a 90° bent heating line. To get the main heating on one side we adjust the distance of the nickel line to the VCSEL. In Fig. 5 the horizontal line is closer to the VCSEL and should have a larger heating effect. In the optical spectra in Fig. 5, a red-shift is clearly seen. With a wavelength shift rate of 0.07 nm/K we get a temperature increase of about $\Delta T = 9 \text{ K}$ but no measurable increase of the birefringence splitting. The thermal cross-resistance with a value of $R_{\text{Th},X} = 9 \text{ K}/(3.16 \text{ V} \cdot 39.8 \text{ mA}) = 0.072 \text{ K/mW}$ is insignificantly larger than in the previous hotspot design.

The obtained results make clear that the small temperature increase (and temperature gradient) in the active VCSEL originates in the bad thermal conductivity between the

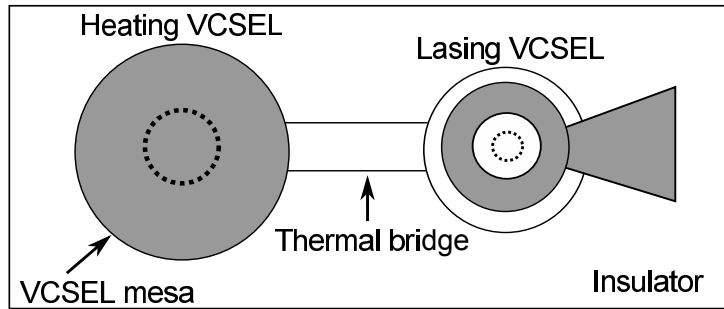


Fig. 6: Schematic top view of a VCSEL chip design for thermal tuning. Dark color and the dashed lines indicate deposited metal and the oxide apertures, respectively.

heating element and the VCSEL. To solve this problem, a revised VCSEL design is necessary. As a possible candidate we investigate the structure sketched in Fig. 6, which incorporates a thermal bridge between the heating element and the active VCSEL.

For convenience, the heat is again generated by a VCSEL with a metalized surface. In the previous designs of Figs. 4 and 5, a polyimide layer (necessary for planarization and electrical insulation) on the surface of the VCSEL chip has led to low lateral thermal conductivity. For the thermal bridge in the new design a compromise must be found between good thermal conductivity and electrical insulation. Thermal simulations are underway to identify, among others, the influence of thermal bridge dimensions (width, length, height) on achievable thermal cross-resistances and stress gradients.

4. Conclusion

New approaches for birefringence tuning in VCSELs were shown. With a second-generation bending device we have obtained a birefringence splitting up to 226 GHz by indirect bending with much smaller sizes of the mount and the sample. Further investigations into thermally induced strain were made. Measurements with integrated hotspot structures show only an internal heating of the VCSEL but no visible increase of the birefringence splitting. Custom-made VCSEL chip designs with optimized placement of heating elements have to be implemented. First simulations are in progress.

5. Acknowledgment

The author thanks Rudolf Rösch and Willi Kogler for fruitful discussions and technical support. Furthermore the author is grateful to Philips Technologie GmbH (U-L-M Photonics) for the provision of the VCSEL samples. This work is funded by the German Research Foundation.

References

- [1] D.M. Kuchta, A.V. Rylyakov, F.E. Doany, C.L. Schow, J.E. Proesel, C.W. Baks, P. Westbergh, J.S. Gustavsson, and A. Larsson, “A 71-Gb/s NRZ modulated 850-nm VCSEL-based optical link”, *IEEE Photon. Technol. Lett.*, vol. 27, pp. 577–580, 2015.
- [2] N.C. Gerhardt and M. Hofmann, “Spin-controlled vertical-cavity surface-emitting lasers”, *Advances in Optical Technol.*, vol. 2012, pp. 268949-1–15, 2012.
- [3] K. Panajotov and F. Prati, “Polarization Dynamics of VCSELs”, Chap. 6 in *VCSELs*, R. Michalzik (Ed.), pp. 181–231. Berlin: Springer, 2013.
- [4] T. Pusch, M. Lindemann, N.C. Gerhardt, M.R. Hofmann, and R. Michalzik “Vertical-cavity surface-emitting lasers with birefringence splitting above 250 GHz”, *Electron. Lett.*, vol. 51, pp. 1600–1602, 2015.
- [5] A.K. Jansen van Doorn, M.P. van Exter, and J.P. Woerdman, “Elasto-optic anisotropy and polarization orientation of vertical-cavity surface-emitting semiconductor lasers”, *Appl. Phys. Lett.*, vol. 69, pp. 1041–1043, 1996.
- [6] A.K. Jansen van Doorn, M.P. van Exter, and J.P. Woerdman, “Tailoring the birefringence in a vertical-cavity semiconductor laser”, *Appl. Phys. Lett.*, vol. 69, pp. 3635–3637, 1996.
- [7] R. Michalzik, “VCSEL Fundamentals”, Chap. 2 in *VCSELs*, R. Michalzik (Ed.), pp. 19–76. Berlin: Springer, 2013.

Growth and Coalescence Studies of (11 $\bar{2}2$) Oriented GaN on Pre-Structured Sapphire Substrates Using Marker Layers

Marian Caliebe

In this article¹, the growth and coalescence of semipolar (11 $\bar{2}2$) oriented GaN layers, deposited on pre-structured r-plane sapphire substrates, is studied with the help of Si-doped marker layers. It has been found to be very important to adjust the shape of the initial GaN stripes by varying the growth temperature to obtain not only a smooth surface, but also a low density of basal plane stacking faults (BSFs) and threading dislocations (TDs) on the wafer surface. With the help of transmission electron microscopy (TEM) and cathodoluminescence measurements (CL), we can conclude that during growth, we need to achieve a compromise between low BSF density, low TD density, and perfect coalescence with smooth surface, free of fissures and other growth artifacts.

1. Introduction

A promising approach for the production of green and yellow GaN-based light-emitting diodes (LEDs) is the usage of semipolar substrates. Compared to commercial c-oriented devices, these substrates have a reduced piezo-electric field in the quantum wells. Thus, the influence of the quantum-confined Stark effect can be reduced, which is expected to result in higher efficiency of the recombination of carriers in the quantum wells [2–6].

The samples studied in this article are produced based on a method first demonstrated by Okada *et al.* [7]. We use 2" r-plane sapphire wafers for hetero-epitaxy. These substrates are patterned with trenches parallel to the a-direction of the sapphire. A special property of these trenches is that one of the side-facets is c-plane-like. Under appropriate GaN growth conditions, the selectivity is large enough that growth mainly takes place on these c-plane-like facets, resulting in GaN stripes that coalesce after some time into a closed layer with the desired (11 $\bar{2}2$) surface. Compared to epitaxy on planar m-oriented sapphire, a much better crystal quality can be achieved [8].

While Okada *et al.* [7] focused on this growth method itself and on growth selectivity on the different sapphire crystal planes, Kurisu *et al.* [9] studied the variation of the shape of the uncoalesced GaN stripes by varying the temperature and V/III ratio and selected the optimum parameters merely by judging the growth selectivity, the shape of the GaN stripes and their surface morphology (before coalescence). However, we focus our studies on the influence of the shape on the fully grown sample by having a closer look on the

¹For the full version of this article see [1].

coalescence behavior and study its impact on defects in the final structure with the help of marker layers. In both publications [7,9], dislocations and stacking faults were already detected by TEM, but their development and propagation has not yet been studied in detail.

The marker layers in this article are produced by doping with Si and can be observed as a contrast caused by changed electrical conductivity in scanning electron microscopy (SEM) [10]. They give direct insight into the growth evolution. It is easily possible to recognize at each point the shape of the growth front. Also, we can immediately observe, how a change of the growth conditions influences the local growth behavior. Moreover, it is possible to correlate the shape found in SEM micrographs on the cross-section with transmission electron microscopy (TEM) images, to understand the propagation of threading dislocations. Comparing samples with and without marker layers, we observed that the influence of the marker layers on the crystal quality is negligible.

2. Experimental

2.1 Sample preparation

The metal organic vapor phase epitaxy (MOVPE) growth experiments are conducted on (1 $\bar{1}$ 02)-oriented sapphire substrates, which are structured in the following way: First, a pattern of resist stripes with a period of 6 μm and an aspect ratio of 1:1 is prepared by common photolithography. Then, trenches are etched by reactive-ion etching (RIE) using the gases Ar, BCl_3 , and Cl_2 . Afterwards, the remaining resist is removed in O_2 plasma. Finally, the sapphire is cleaned wet-chemically with KOH and piranha solution ($\text{H}_2\text{SO}_4:\text{H}_2\text{O}_2$).

2.2 MOVPE growth conditions

The sapphire wafers are overgrown in a commercial Aixtron-200/4 RF-S HT reactor using the precursors TMGa, NH_3 , TMAI, and SiH_4 . The indicated growth temperatures are the reactor temperatures measured on the backside of the susceptor which may differ from the real wafer temperature. The sample structure is sketched in Fig. 1 and given in Table 1. First, an intentionally doped AlN:O nucleation layer with an oxygen content of approximately 10%, similar as in our standard c-plane growth [11, 12], is deposited. Then, a GaN buffer layer (layer I) is grown at 1080 $^\circ\text{C}$, a TMGa flow of $f(\text{TMGa}) = 102 \mu\text{mol}/\text{min}$ with a V/III ratio of 870, and a reactor pressure of 150 hPa. After 3.5 min, the reactor temperature is slowly ramped to 1000 $^\circ\text{C}$. After growth of approximately 0.5 μm on the c-facet of the sapphire trench, an in situ deposited SiN_x interlayer (layer II) is incorporated for defect reduction using SiH_4 [13]. Then, GaN growth continues for further 6 min. In the next 50 min, the GaN stripe (layer III) is formed. In layer III, 5 marker layers are incorporated by doping for 2 min with SiH_4 in a period of 10 min with an estimated resulting n -carrier density of $\sim 5 \cdot 10^{19} \text{cm}^{-3}$. Then, the reactor temperature is set to 970 $^\circ\text{C}$ for 40 min (4 marker layers) to deposit a GaN interlayer (layer IV). Its purpose is discussed in [1]. Finally, in layer V, the reactor parameters are set to

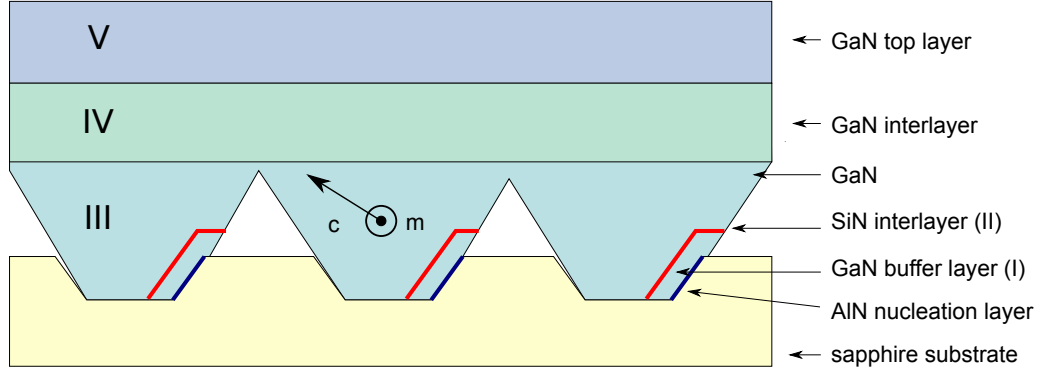


Fig. 1: Sketch of the layer sequence of samples A, B, and C.

Table 1: Layer sequence of the samples studied in Sect. 3.1. The marker layers are deposited in a period of 10 min.

Layer	Layer #	Growth conditions	Sample #	Marker layers
GaN top layer	V	1041 °C, V/III = 140, $f(\text{TMGa}) = 156 \mu\text{mol}/\text{min}$		3
GaN interlayer	IV	970 °C		4
GaN stripe	III	6 min, ramp to $x = \begin{cases} 950^\circ\text{C} \\ 1000^\circ\text{C} \\ 1050^\circ\text{C} \end{cases}$	A B C	5
SiN _x interlayer	II	1000 °C		-
GaN buffer layer	I	1080 °C, ramp to 1000 °C		-

$T = 1041^\circ\text{C}$, $V/\text{III} = 140$, and $f(\text{TMGa}) = 156 \mu\text{mol}/\text{min}$ (resulting in a higher growth rate), since this has been found to be the optimum conditions after coalescence [14]. Under these conditions, 3 marker layers are deposited.

In this experiment, the growth temperature before coalescence (layer III) is varied between 950°C and 1050°C (Table 1) to study its influence on the resulting layer quality. Besides SEM and TEM studies, CL is used to investigate the distribution of BSFs and dark spots on the wafer surface, which allows inference to the distribution and density of TDs. The ratio of the BSF I_1 at 3.41 eV towards the donor bound exciton (D^0X) peak in photoluminescence (PL) is a qualitative measure of the amount of BSFs on the wafer surface. Further, the full width at half maximum (FWHM) of high resolution X-ray diffraction (HRXRD) rocking curves allows inference to the crystal quality. Atomic force microscopy (AFM) is used to determine the surface texture and roughness.

3. Results and Discussion

3.1 Shape of initial GaN stripes

In Fig. 2 (first row), SEM micrographs of the samples' cross-sections are presented, which show the marker layers. In TEM, (Fig. 2, second row), the marker layers are not visible. The black lines in these images are threading dislocations.

By the course of the marker layers, it can be observed that at 950 °C (sample A), the shape of the initial GaN stripes is only formed by $\{11\bar{2}2\}$ planes. By increasing the temperature to 1000 °C (sample B), also (0001) and $(11\bar{2}0)$ planes appear. At 1050 °C (sample C), they become larger than the $(11\bar{2}2)$ surface plane. This behavior has already been observed by Kurisu *et al.* by stopping the growth before coalescence [9].

The initial shape of the GaN stripes has a strong influence on coalescence and the residual layer quality: It is well known that basal plane stacking faults (BSFs) are mainly located in the -c-wing and may be blocked at the coalescence point by a small gap (see e.g. [15–18]). For sample A, no a-plane exists at all. Thus, there is no gap in the coalescence region to block BSFs. They can propagate unhindered to the surface, confirmed by the highest BSF-related peak in PL (Fig. 3) and largest area of BSF induced luminescence in CL (Fig. 2, bottom). Additionally, the neighboring stripe grows in c-direction over the $(11\bar{2}2)$ plane leading to non-planar coalescence. Sometimes this overlap can continue up to the wafer surface resulting in the formation of several 10 μm long surface immersions called “chevrons” that have already been reported by Brunner *et al.* on $(11\bar{2}2)$ GaN samples produced after the same approach [19] and on $(11\bar{2}2)$ GaN grown on m-plane sapphire patterned with a SiO_2 epitaxial lateral overgrowth (ELOG) mask as reported by Zhu *et al.* [20]. While up to now only assumptions about the origin of “chevrons” could be done, we now were able to directly observe their formation (cf. [1]).

The optimum results were achieved for sample B (Fig. 2, center). Here, the surface is already planar shortly after coalescence, which leads to the smoothest surface and narrowest rocking curves in HRXRD (Fig. 4). Also, the small gap at the coalescence region is formed parallel to the a-plane to stop the continuation of BSFs to the surface.

If the sample is grown too hot (sample C), we observe the worst case of coalescence. Now, stripes grow together in a “V”-shape, which is formed by the a- and c-facets of neighboring stripes. However, the BSFs on the c-wing are blocked most effectively leading to the smallest BSF density on the surface (compare PL Fig. 3 and CL Fig. 2, bottom). The “V”-shape often prevents coalescence leading to fissures which propagate to the surface ending in a gap as shown in the SEM cross-section (Fig. 5, left), the SEM bird's eye view (Fig. 5, right) and the AFM image (Fig. 6, right). These fissures strongly decrease the electrical conductivity perpendicular to the stripes. This can be observed e.g. in van der Pauw Hall measurements, manifested in small geometry factors [21].

3.2 TEM investigations

In the TEM images (Fig. 2, second row), it is observed that threading dislocations mainly start on the c-sapphire-GaN interface and propagate in c-direction. TDs bend by 90° to

the a-direction as soon as they hit the $(11\bar{2}2)$ plane (Fig. 2, second row, left). However, if there is a wide c-plane like in sample C, some TDs might never bend and continue propagating in c-direction (Fig. 2, second row, right). A very similar dislocation bending has already been reported on c-oriented samples at 2S-ELO (two-step epitaxial lateral overgrowth) and FACELO (facet-controlled ELO) investigations, respectively [22–24].

Both bent and un-bent dislocations have the chance to propagate to the surface. For good layer quality, the bending should happen as early as possible. This way, the dislocations can be either blocked at the coalescence gap, or are at least cumulated above the coalescence point and not distributed equally over the whole sample surface.

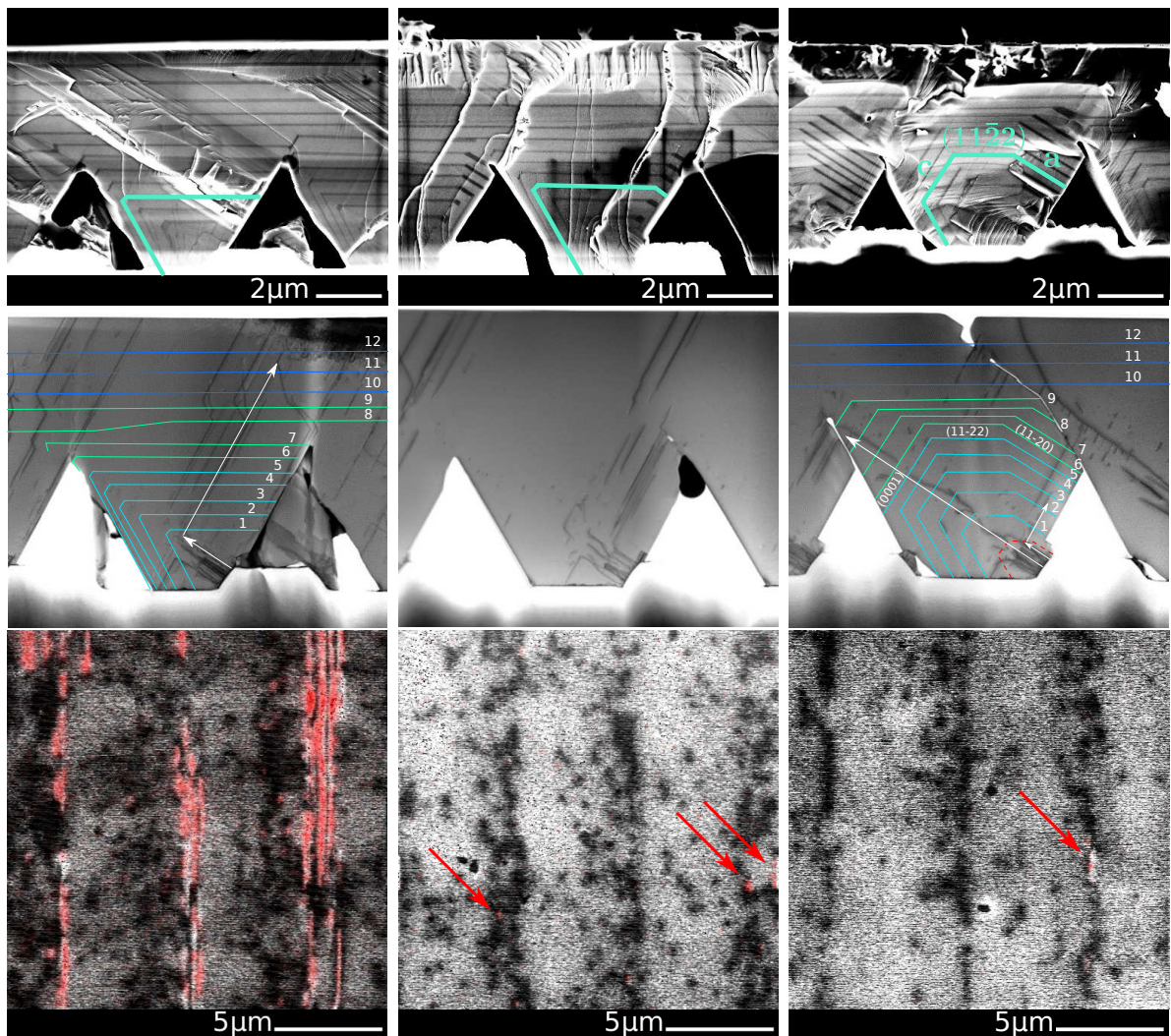


Fig. 2: Samples A (left), B (center), and C (right). First row: SEM cross-section. Second row: TEM images correlated with the course of the marker layers detected by SEM. The white arrows indicate the course of TDs. As soon as a TD hits the $(11\bar{2}2)$ plane, it bends from the c- into the a-direction. The red dashed line indicates the estimated course of the SiN_x interlayer. Third row: Low temperature CL measurement (3 keV, $T = 10$ K) of the wafer surface. The images are a superposition of a panchromatic map (grayscale) and the luminescence of the BSF I₁ (red).

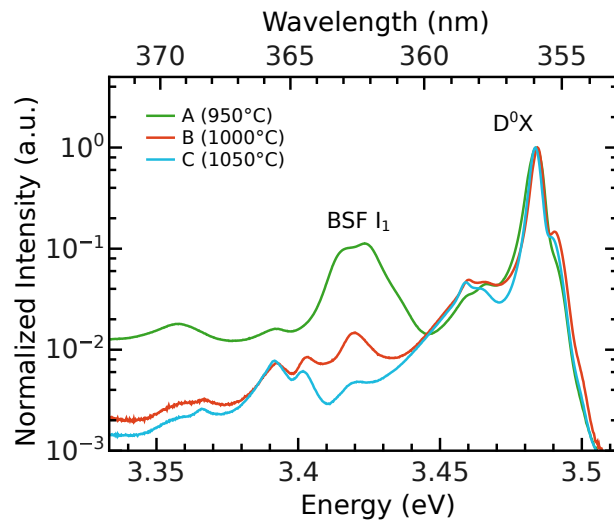


Fig. 3: Low temperature PL spectra measured at $T = 15\text{K}$ for the samples A–C. Due to the coalescence gap, BSFs are most effectively blocked in sample C, while sample A shows the highest density of BSFs on the surface.

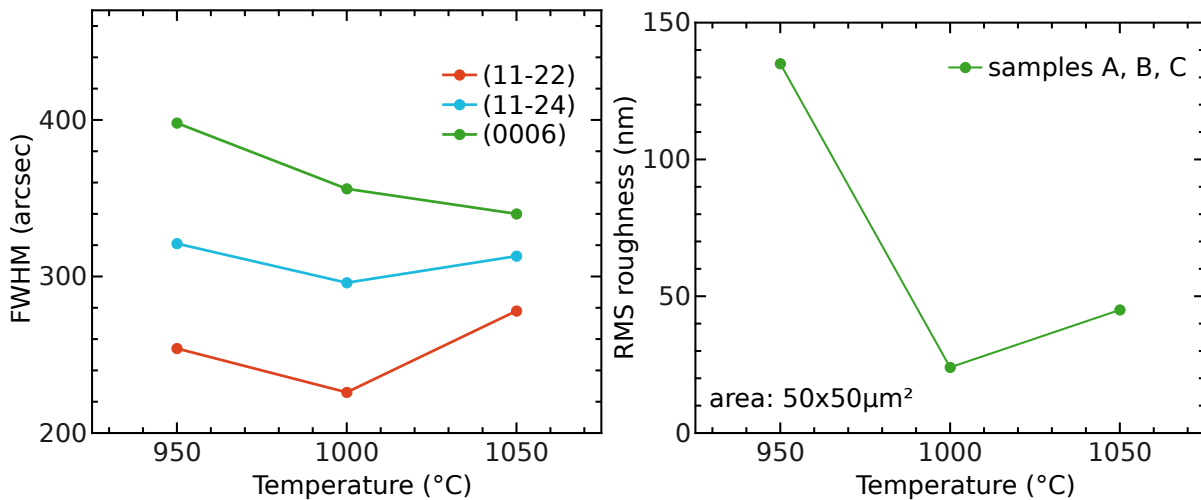


Fig. 4: HRXRD and AFM results. The temperature indicates the growth temperature before coalescence of samples A, B, and C. Sample B is clearly the optimum.

The TEM micrographs also confirm that sample B is the best (Fig. 2, second row). For both samples A and B, the c-plane is (almost) not existent. Thus, the dislocations bend early. However, in sample B many dislocations can be blocked by the gap at the coalescence point. In sample A, all dislocations can propagate to the surface, which might be the worst case scenario. Sample C has a huge c-plane facet just before coalescence. Therefore, dislocations might never bend. However, if the coalescence gap is big enough, they can be blocked (Fig. 2, second row, right).

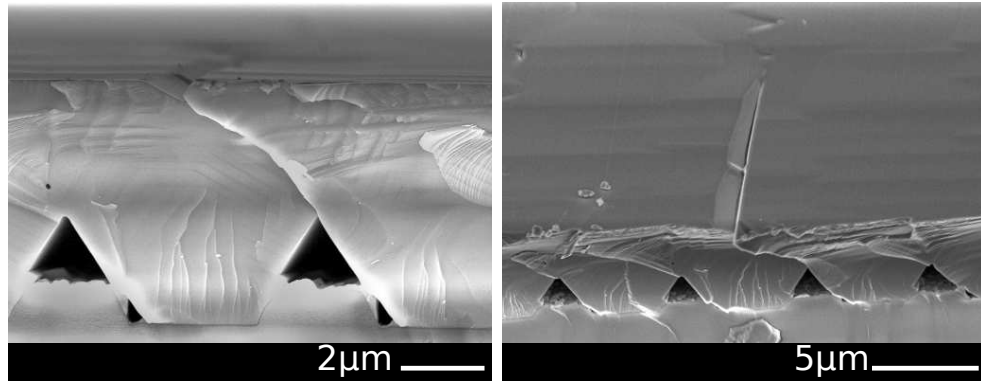


Fig. 5: Cross-section of failed coalescence leading to a “V”-pit (left). Bird’s eye view of “V”-pit (right). SEM images of a fissure resulting in a “V”-pit on the surface of sample C.

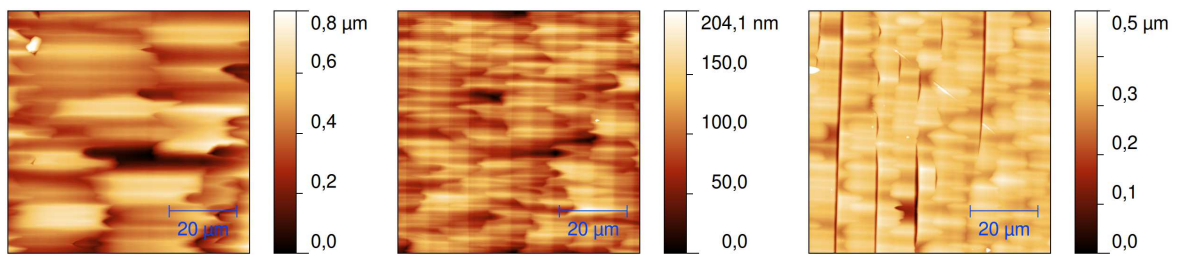


Fig. 6: AFM images of samples A, B, and C. The sapphire trenches are oriented vertically.

3.3 CL investigations

The low temperature cathodoluminescence (CL) measurement results of the wafer surface (3 keV, $T = 10$ K) are consistent with the findings of TEM. In Fig. 2 (bottom row), the superposition of the panchromatic map (gray scale) and BSF I_1 intensity (red) is depicted. Sample A shows the highest density of dark spots and BSFs, because both the TDs and SFs can propagate unhindered to the surface. Sample B has a clearly reduced density of dark spots and BSFs. We find that the dark spots are clustered in lines, while the BSFs are mainly aligned on the -c side parallel to the dark spots. Consistent with the PL measurement (Fig. 3), almost no BSFs can be found on sample C. Because of the huge gaps and fissures, also a lot of the dislocations can’t propagate to the surface resulting in an even smaller dark spot density compared to sample B.

Due to the superposition of the dark spots, it is not possible to determine their density exactly. The dark spot density could only be estimated roughly to $3 \cdot 10^8 \text{cm}^{-2}$, $1 \cdot 10^8 \text{cm}^{-2}$ and $8 \cdot 10^7 \text{cm}^{-2}$ for the samples A, B, and C, respectively.

4. Conclusion

In this study layers of $(11\bar{2}2)$ oriented GaN were grown on pre-structured sapphire substrates. We found that a variation of the shape of the initial GaN stripes has a huge impact on the coalescence behavior and the resulting layer and surface quality. We observed that threading dislocations starting from the stripe-shaped, c -oriented sapphire GaN interface in c -direction are bent by 90° as soon as they hit the $(11\bar{2}2)$ plane. In GaN stripes with a comparably large c -plane facet, TDs might never bend and continue up to the wafer surface.

We conclude that we have to make a compromise between a minimum TD density, a minimum BSF density, a good coalescence, and a smooth surface. Thus, an intermediate growth temperature of 1000°C of the initial GaN stripes before coalescence seems to be the best choice. Higher growth temperature of the initial GaN stripes would lead to smaller BSF density, but then a c -plane emerges, preventing TDs from bending into the a -plane and continuing unhindered to the wafer surface. In contrast, at lower growth temperature, BSFs from the $-c$ -wing propagate to the wafer surface resulting in a large BSF density.

Acknowledgment

I thank the co-authors of the full version of this article [1], namely Y. Han and C. Humphreys of the Department of Materials Science and Metallurgy of the University of Cambridge, United Kingdom, for TEM measurements, M. Hocker and K. Thonke of the Institute of Quantum Matter, Semiconductor Physics Group at Ulm University, Germany, for CL measurements, as well as T. Meisch and F. Scholz of the Institute of Optoelectronics at Ulm University, Germany, for scientific support. For technical support in the structuring of the sapphire wafers, I thank R. Rösch and C. Steinmann of the Institute of Optoelectronics at Ulm University. This work was financially supported by the European Commission (FP7) within the framework of the project “AlGaInN materials on semi-polar templates for yellow emission in solid state lighting applications” (ALIGHT).

References

- [1] M. Caliebe, Y. Han, M. Hocker, T. Meisch, C. Humphreys, K. Thonke, and F. Scholz, “Growth and coalescence studies of $(11\bar{2}2)$ oriented GaN on pre-structured sapphire substrates using marker layers”, *Phys. Status Solidi B*, vol. 253, pp. 46–53, 2016.
- [2] F. Scholz, T. Wunderer, B. Neubert, F. Feneberg, and K. Thonke, “GaN-based light-emitting diodes on selectively grown semipolar crystal facets”, *MRS Bulletin*, vol. 34, pp. 328–333, 2009.
- [3] T. Takeuchi, H. Amano, and I. Akasaki, “Theoretical study of orientation dependence of piezoelectric effects in wurtzite strained GaInN/GaN heterostructures and quantum wells”, *Jpn. J. Appl. Phys.*, vol. 39, pp. 413–416, 2000.

-
- [4] F. Bernardini, V. Fiorentini, and D. Vanderbilt, “Spontaneous polarization and piezoelectric constants of III-V nitrides”, *Phys. Rev. B*, vol. 56, pp. R10024–R10027, 1997.
- [5] O. Ambacher, “Growth and applications of group III-nitrides”, *J. Phys. D: Appl. Phys.*, vol. 31, pp. 2653–2710, 1998.
- [6] A.E. Romanov, T.J. Baker, S. Nakamura, and J.S. Speck, “Strain-induced polarization in wurtzite III-nitride semipolar layers”, *J. Appl. Phys.*, vol. 100, pp. 023522-1–10, 2006.
- [7] N. Okada, A. Kurisu, K. Murakami, and K. Tadatomo, “Growth of semipolar (11 $\bar{2}2$) GaN layer by controlling anisotropic growth rates in r-plane patterned sapphire substrate”, *Appl. Phys. Express*, vol. 2, pp. 091001-1–3, 2009.
- [8] P. de Mierry, N. Kriouche, M. Nemoz, S. Chenot, and G. Nataf, “Semipolar GaN films on patterned r-plane sapphire obtained by wet chemical etching”, *Appl. Phys. Lett.*, vol. 96, pp. 231918-1–3, 2010.
- [9] A. Kurisu, K. Murakami, Y. Abe, N. Okada, and K. Tadatomo, “Characterization of semipolar (11 $\bar{2}2$) GaN on c-plane sapphire sidewall of patterned r-plane sapphire substrate without SiO₂ mask”, *Phys. Status Solidi C*, vol. 7, pp. 2059–2062, 2010.
- [10] F. Habel, P. Brückner, and F. Scholz, “Marker layers for the development of a multistep GaN FACELO process”, *J. Cryst. Growth*, vol. 272, pp. 515–519, 2004.
- [11] J. Hertkorn, P. Brückner, S.B. Thapa, T. Wunderer, F. Scholz, M. Feneberg, K. Thonke, R. Sauer, M. Beer, and J. Zweck, “Optimization of nucleation and buffer layer growth for improved GaN quality”, *J. Cryst. Growth*, vol. 308, pp. 30–36, 2007.
- [12] J. Bläsing, A. Krost, J. Hertkorn, F. Scholz, L. Kirste, A. Chuvilin, and U. Kaiser, “Oxygen induced strain field homogenization in AlN nucleation layers and its impact on GaN grown by metal organic vapor phase epitaxy on sapphire: An X-ray diffraction study”, *J. Appl. Phys.*, vol. 105, pp. 033504-1–9, 2009.
- [13] M. Caliebe, T. Meisch, B. Neuschl, S. Bauer, J. Helbing, D. Beck, K. Thonke, M. Klein, D. Heinz, and F. Scholz, “Improvements of MOVPE grown (11 $\bar{2}2$) oriented GaN on prestructured sapphire substrates using a SiN_x interlayer and HVPE overgrowth”, *Phys. Status Solidi C*, vol. 11, pp. 525–529, 2014.
- [14] M. Caliebe, T. Meisch, M. Madel, and F. Scholz, “Effects of miscut of prestructured sapphire substrates and MOVPE growth conditions on (11 $\bar{2}2$) oriented GaN”, *J. Cryst. Growth*, vol. 414, pp. 100–104, 2015.
- [15] B. Lacroix, M.P. Chauvat, P. Ruterana, G. Nataf, and P. De Mierry, “Efficient blocking of planar defects by prismatic stacking faults in semipolar (11 $\bar{2}2$)-GaN layers on m-sapphire by epitaxial lateral overgrowth”, *Appl. Phys. Lett.*, vol. 98, pp. 121916-1–3, 2011.

- [16] N. Kriouche, M. Leroux, P. Vennéguès, M. Nemoz, G. Nataf, and P. de Mierry, “Filtering of defects in semipolar (11 $\bar{2}2$) GaN using 2-steps lateral epitaxial overgrowth”, *Nanoscale Res. Lett.*, vol. 5, pp. 1878–1881, 2010.
- [17] F. Tendille, P. De Mierry, P. Vennéguès, S. Chenot, and M. Teisseire, “Defect reduction method in (11-22) semipolar GaN grown on patterned sapphire substrate by MOCVD: Toward heteroepitaxial semipolar GaN free of basal stacking faults”, *J. Cryst. Growth*, vol. 404, pp. 177–183, 2014.
- [18] S. Schwaiger, S. Metzner, T. Wunderer, I. Argut, J. Thalmair, F. Lipski, M. Wieneke, J. Bläsing, F. Bertram, J. Zweck, A. Krost, J. Christen, and F. Scholz, “Growth and coalescence behavior of semipolar (11 $\bar{2}2$) GaN on pre-structured r-plane sapphire substrates”, *Phys. Status Solidi B*, vol. 248, pp. 588–593, 2011.
- [19] F. Brunner, F. Edokam, U. Zeimer, W. John, D. Prasai, O. Krüger, and M. Weyers, “Semi-polar (11 $\bar{2}2$)-GaN templates grown on 100 μ m trench-patterned r-plane sapphire”, *Phys. Status Solidi B*, vol. 252, pp. 1189–1194, 2015.
- [20] T. Zhu, C.F. Johnston, M.J. Kappers, and R.A. Oliver, “Microstructural, optical, and electrical characterization of semipolar (11 $\bar{2}2$) gallium nitride grown by epitaxial lateral overgrowth”, *J. Appl. Phys.*, vol. 108, pp. 083521-1–8, 2010.
- [21] L.J. van der Pauw, “A method of measuring the resistivity and Hall coefficient on lamellae of arbitrary shape”, *Philips Technical Review*, vol. 20, pp. 220–224, 1958.
- [22] K. Hiramatsu, K. Nishiyama, M. Onishi, H. Mizutani, M. Narukawa, A. Motogaito, H. Miyake, Y. Iyechika, and T. Maeda, “Fabrication and characterization of low defect density GaN using facet-controlled epitaxial lateral overgrowth (FACELO)”, *J. Cryst. Growth*, vol. 221, pp. 316–326, 2000.
- [23] P. Vennéguès, B. Beaumont, V. Bousquet, M. Vaille, and P. Gibart, “Reduction mechanisms for defect densities in GaN using one- or two-step epitaxial lateral overgrowth methods”, *J. Appl. Phys.*, vol. 87, pp. 4175–4181, 2000.
- [24] V. Wagner, O. Parillaud, H.J. Bühlmann, M. Ilegems, S. Gradecak, P. Stadelmann, T. Riemann, and J. Christen, “Influence of the carrier gas composition on morphology, dislocations, and microscopic luminescence properties of selectively grown GaN by hydride vapor phase epitaxy”, *J. Appl. Phys.*, vol. 92, pp. 1307–1316, 2002.

Efficiency Studies of Semipolar GaInN-GaN Quantum Well Structures

Tobias Meisch and Ferdinand Scholz

In order to clarify the reasons for the fairly poor electroluminescence (EL) performance of semipolar LED structures grown on patterned sapphire wafers, we have analyzed both, pure photoluminescence (PL) test structures without doping only containing 5 GaInN quantum wells and full EL test structures, all emitting at a wavelength of about 510 nm. Evaluating the PL intensity over a wide range of temperatures and excitation powers, we conclude that such quantum wells possess a fairly large internal quantum efficiency of about 20%. However, on EL test structures containing nominally the same quantum wells, we obtained an optical output power of only about 150 μ W at an applied current of 20 mA. This may be due partly to some thermal destruction of the quantum wells by the overgrowth with p-GaN. Even more important seems to be the not yet finally optimized p-doping of such structures.

1. Introduction

As discussed in our previous annual report contributions (see, e.g., [1]) and in other publications (see, e.g., [2] and references therein), the efficiency of green light emitting diodes based on GaN heterostructures is still significantly inferior as compared to their blue light emitting counterparts. Such longer wavelength emission requires an increased In content in the active quantum wells of these devices leading — on the one hand — to a more defective material owing to the increasing lattice mismatch to the GaN host material and the need to use fairly low growth temperatures for such In-rich layers. On the other hand, these quantum wells are heavily pseudomorphically strained causing strong internal piezoelectric fields leading to a tilt of the valence and conduction band in the quantum wells. Consequently, the wave functions of electrons and holes get spatially separated and the recombination probability is predicted to be significantly reduced [3]. These piezoelectric fields can be reduced or even avoided by growing such heterostructures in non- c -directions. While nonpolar GaN structures typically possess a poor crystal quality, semipolar growth directions like $\{11\bar{2}2\}$, $\{10\bar{1}1\}$, or $\{20\bar{2}1\}$ are a promising compromise between a reasonable crystal quality and a reduced internal field.

Our investigations focus on the growth of semipolar $\{11\bar{2}2\}$ GaN heterostructures on $\{10\bar{1}2\}$ trench-patterned sapphire substrates, similar as reported by Okada et al. [4]. The GaN, nucleating on the inclined c -side-facets of these trenches, first grows in the well-established c -direction, then forms triangularly shaped stripes and eventually coalesces after a suitable growth time to a planar $\{11\bar{2}2\}$ oriented surface [2, 5]. On such planar

semipolar surfaces, the growth of semipolar GaInN quantum wells and complete LED or laser diode structures in a single epitaxial run is possible. The wafer diameter is just limited by the reactor size. In our studies, 2" diameter sapphire wafers were used.

The main goal of these studies was the evaluation of the quantum efficiency of our semipolar quantum wells for emission wavelengths beyond 500 nm. As reported earlier [1,6], our semipolar LEDs emit comparably weak light intensities of about 100 μW at 20 mA. The current studies should help to clarify whether this is mainly caused by the limited quantum well quality or whether the p- and n-type doping of the outer barrier layers may be responsible for this behavior. Therefore, we have investigated the characteristics of GaInN quantum wells grown on previously optimized [5] semipolar GaN templates and of complete LED test structures. This required further optimisation of the p-doped layers which will also be discussed here. Magnesium, the only acceptor applicable to GaN, needs to be incorporated in huge concentrations, typically in the range of several 10^{19} cm^{-3} for hole concentrations still below 10^{18} cm^{-3} [7] owing to its large activation energy of about 180 meV [8]. Even worse, the Mg incorporation in $\{11\bar{2}2\}$ -oriented GaN is reported to be less efficient than on *c*-plane surfaces [9–11]. Somewhat higher concentrations have been obtained for lower growth temperatures, helping to overcome the quite large parasitic n-type background [1]. However, only a small Mg concentration window seems to be suitable for good semipolar LED performance.

2. Experimental

As reported earlier in more detail [1], trenches have been defined by optical lithography and then etched into $(10\bar{1}2)$ oriented sapphire wafers by reactive ion etching leading to *c*-plane-like facets on one side of the stripes. All other facets have been covered by directional sputtering of SiO_2 in order to prevent parasitic growth.

The MOVPE growth was done in a commercial Aixtron-200/4 RF-S HT reactor using the standard precursors ammonia (NH_3), trimethylgallium (TMGa), trimethylaluminum (TMAI) and trimethylindium (TMI). For doping, silane (SiH_4) and bis(cyclopentadienyl)-magnesium (Cp_2Mg) have been used. The details of the nominally undoped GaN buffer layer growth including a defect-reducing SiN interlayer up to a total thickness of about 5 μm is described in [1]. On top of such templates, GaInN-GaN quantum well test structures with 5 quantum wells have been grown with a quantum well width L_z of about 2.2 nm and a GaN barrier width L_B of about 6.5 nm. In order to achieve an emission wavelength beyond 500 nm, we have chosen quite low growth temperatures of 725 °C and 760 °C for wells and barriers, respectively. The top GaN layer was grown at the same conditions as the GaN barriers with a thickness of about 13 nm in order to allow efficient photoluminescence excitation even with a HeCd laser. For LED test structures, a 2 μm thick Si-doped GaN layer was grown between buffer and first quantum well with a nominal Si concentration of about 10^{19} cm^{-3} . After the last quantum well, 30 nm of undoped GaN have been deposited to minimize back-diffusion of Mg into the quantum wells. The structure was finalized by a Mg-doped p-GaN layer with a thickness of 100 nm. This layer was grown at a temperature of 910 °C, where we observed a larger Mg incorporation as

compared to higher temperatures [1]. Moreover, such fairly low capping layer temperature minimizes the detrimental thermal load to the GaInN quantum wells. More details of the Mg doping of this layer will be discussed later in this report. In order to have a low contact resistivity, an even higher doped cap layer with a thickness of about 10 nm was grown on top.

The quantum well structures were evaluated by photoluminescence (PL) at various excitation powers by mainly using a GaN-based laser diode with a wavelength of 405 nm and a maximum output power of more than 300 mW as excitation source. Simple p-type contacts with a diameter of 90 μm have been processed on the LED test structures by evaporating In, whereas the n-type contact has been formed by scratching the surface down to the n-GaN layer. The optical output power of these structures was measured on-wafer under DC conditions inside an integrating sphere at room temperature without additional light outcoupling features.

3. Photoluminescence of Semipolar Quantum Wells

In order to find out, whether the semipolar quantum wells are significantly inferior as compared to common polar ones, we have investigated our structures by PL in a wide temperature range between 10 K and room temperature. Thus, we can estimate the internal quantum efficiency as the PL intensity ratio between room temperature and low temperature, if we assume a pure radiative emission at low temperature.

Our QW samples show indeed a quite strong PL at low temperature and at room temperature (Fig. 1).

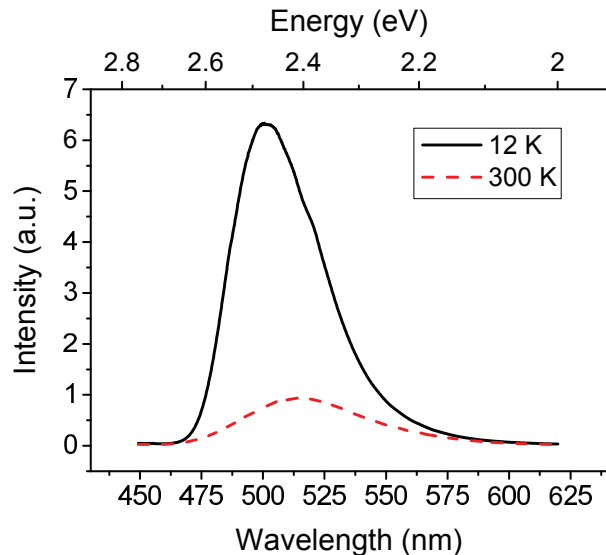


Fig. 1: PL spectra of one of our quantum well structures at low and room temperature.

The PL intensity of such quantum well structures is expected to be governed by the well-known *ABC-model*. The total spontaneous recombination rate R_{total} is given by

$$R_{\text{total}} = A \cdot n + B \cdot n^2 + C \cdot n^3 \quad (1)$$

where n describes the carrier concentration, A is the coefficient describing non-radiative transitions according to the Shockley-Read-Hall model, B represents the radiative recombination coefficient, and C is the Auger coefficient. Hence the radiative efficiency, also called “internal quantum efficiency” η_{IQE} depends on the carrier concentration according to

$$\eta_{\text{IQE}} = \frac{R_{\text{rad}}}{R_{\text{total}}} = \frac{B \cdot n^2}{A \cdot n + B \cdot n^2 + C \cdot n^3}. \quad (2)$$

Consequently, the internal quantum efficiency η_{IQE} is expected to change with carrier concentration. In order to get reliable data, we therefore have measured the PL intensity as a function of excitation intensity at many temperatures (Fig. 2).

Indeed, we found that the intensity ratio between room temperature and low temperature at a given laser excitation power is fairly constant in this range of excitation power. This ratio is often interpreted as internal quantum efficiency, assuming that the non-radiative coefficient A is negligible at low temperature and hence the recombination rate at low temperature is purely radiative. This assumption is fair if this ratio saturates at a high level for temperatures close to 0 K (Fig. 3). On the other hand, the Auger term should be still negligible, i.e. the excitation power should be not too large, being visible by the fact, that the PL efficiency does not yet decrease with increasing excitation power (Fig. 2). Hence, these data (Fig. 3) allow us to estimate a fairly large internal quantum efficiency of $\eta_{\text{IQE}} > 25\%$, which is confirmed by a comparably strong absolute PL intensity of these semipolar QWs.

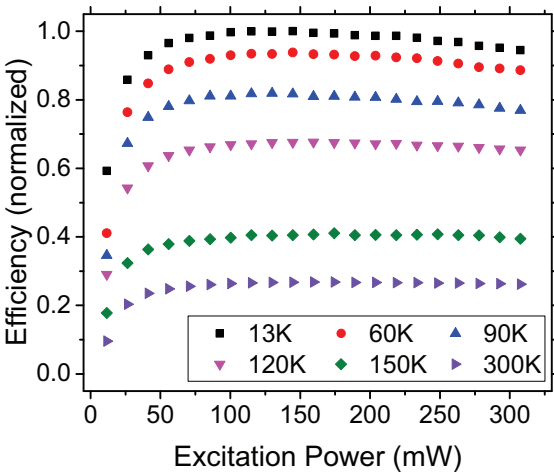


Fig. 2: Ratio of integrated photoluminescence intensity and excitation power (normalized) versus excitation laser power measured at various temperatures.

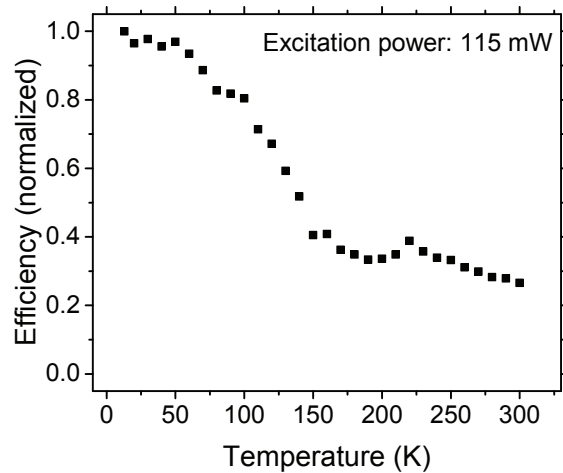


Fig. 3: Ratio of integrated photoluminescence intensity and excitation power (normalized) versus temperature at a laser excitation power of 115 mW.

As expected, our semipolar quantum wells show only a minor wavelength shift with excitation power between 10 and 300 mW of about 3 nm (Fig. 4, left), while a similarly grown polar quantum well structure shifts by 13 nm (Fig. 4, right), although emitting at somewhat shorter wavelength. Such a shift is a consequence of a screening of the internal

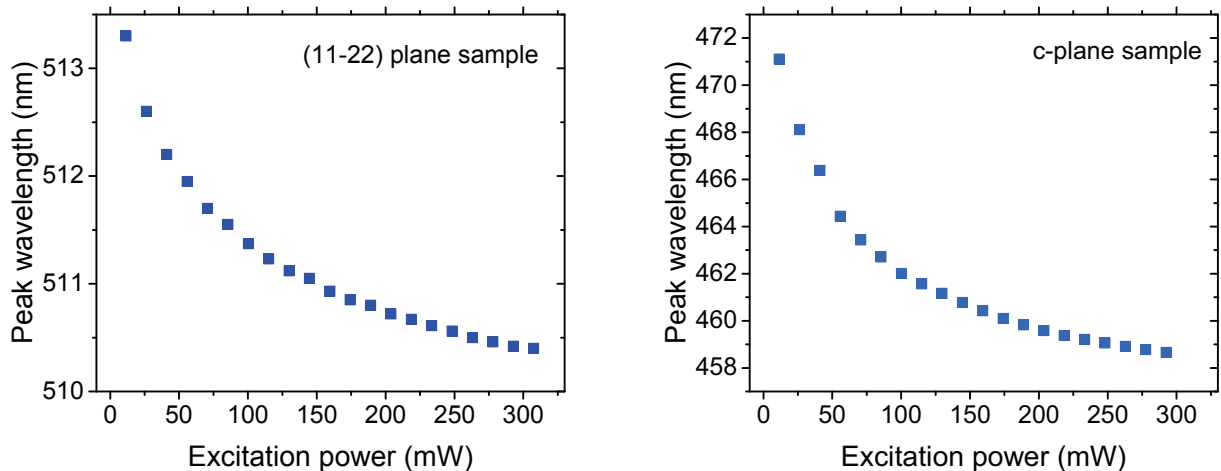


Fig. 4: PL peak shift of a semipolar QW structure (left) and a similar polar structure (right) at room temperature for the same excitation power range.

piezo-electric field in the quantum wells by the excited carriers. Hence, a smaller shift confirms the smaller electric field in our semipolar quantum wells.

4. Electroluminescence from Semipolar Test Structures

As described above, we have embedded such QWs into n- and p-doped GaN layers thus forming an electroluminescence test structure, which can be regarded as a simple semipolar light emitting diode (LED). As discussed previously, the Mg doping was carefully optimized. This eventually resulted in p-doped semipolar GaN layers despite the still fairly large n-type background as directly proven by Hall experiments [1]. Indeed, p-type behavior could be only obtained in a small window of Mg fluxes (Fig. 5). At low Mg flux, the n-background dominates, whereas at large flux, we assume that self-compensation effects lead again to n-type behavior as well-known for polar structures [7].

Accordingly, the LED performance seems to be very sensitive to the Mg flow during the growth of the top p-GaN layer (Fig. 6).

For the best Mg flow the total light output power reaches $150 \mu\text{W}$ at a current of 20 mA. Although being quite large as compared to other results obtained for semipolar LEDs on foreign substrates (see, e.g., [12]), this value still represents a wall-plug efficiency of $\eta_{\text{WPE}} < 0.25\%$. Even if we assume fairly large losses by a low light extraction efficiency, such values seem to indicate that the internal quantum efficiency of our LED structures is much lower than those 20% or so which we measured on our PL structures (see Sect. 3). In order to check whether the QWs of our LEDs are indeed worse than those of our PL structures, we have measured the PL intensities of both types of structures side by side carefully establishing similar measurement conditions (Fig. 7). Here, we used again the blue laser diode as excitation source in order to minimize any absorption of the excitation light in the top p-layer, although such losses cannot be completely disregarded. Indeed, the PL intensity of the QW structure is about 3 times brighter than the intensity of the LED test structure. This may indicate some degradation of the QWs in the LED structure

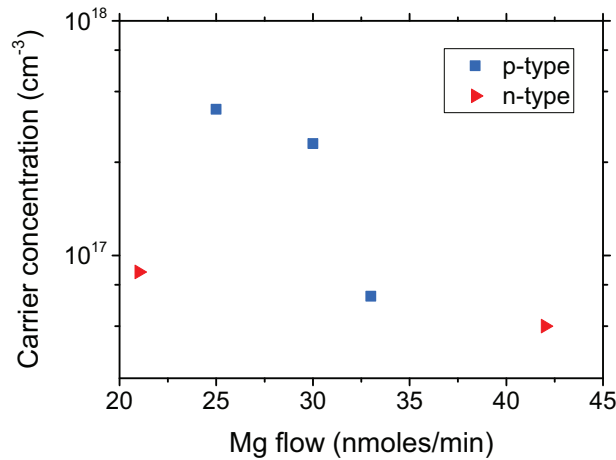


Fig. 5: Carrier concentration measured by the van der Pauw Hall method on Mg-doped test structures at room temperature versus Mg flux. We obtained p-doping only between about 24 and 35 nmol/min Mg flux.

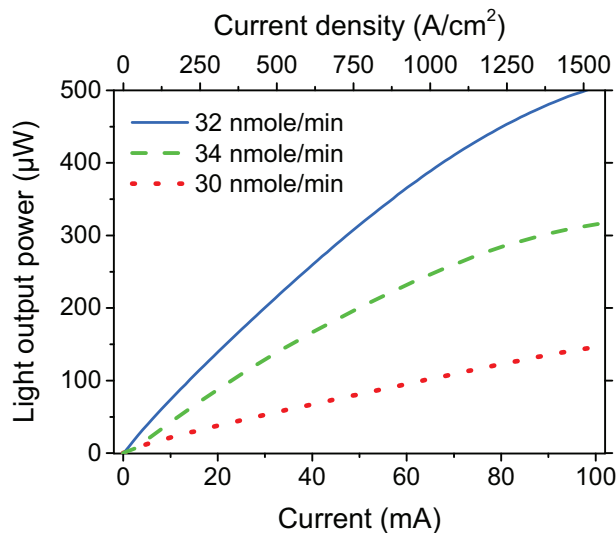


Fig. 6: Electroluminescence intensity versus applied current at room temperature for three different Mg flows during p-GaN growth. Owing to our small p-contact size, fairly large current densities have been obtained (top axis).

by the overgrowth of the QWs by the p-layer grown at 910 °C. Owing to the fairly large In content in these green light emitting QWs of about 30%, this may be indeed reasonable. However, this does not explain completely the poor performance of our LEDs. Therefore, we think that also the pn junction must be further optimized, particularly by reducing the strong parasitic oxygen doping in our semipolar GaN further.

5. Conclusion

We have carefully evaluated the photoluminescence and electroluminescence efficiency of semipolar GaInN quantum wells grown on patterned sapphire wafers. We found a

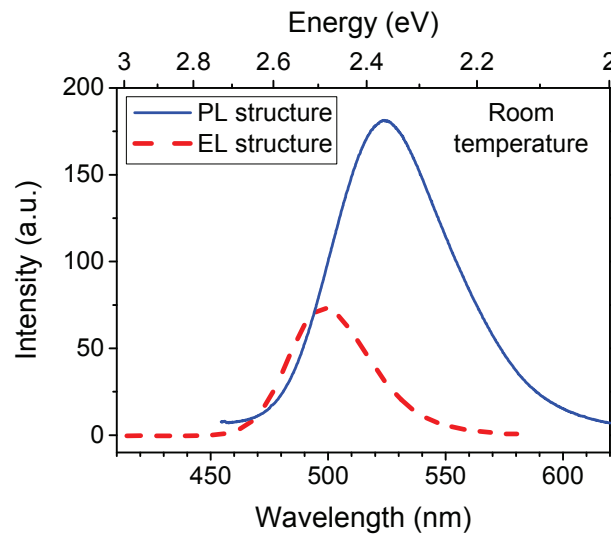


Fig. 7: Photoluminescence measured under comparable conditions on a QW and a LED test structure at room temperature.

fairly large ratio between room temperature and low temperature photoluminescence on samples which do not contain a p-doped top layer. From these data, we can estimate an internal quantum efficiency of about 20%. However, LED test structures show fairly weak electroluminescence indicating a wall plug efficiency below 0.25%. When comparing PL and EL data measured on various samples, we suppose that this strong discrepancy is partly a consequence of some degradation of the high In content quantum wells during the p-layer overgrowth. However, a further optimisation of the p- and n-type doping profiles seems to be even more important.

Acknowledgment

We are grateful for the strong technical and scientific support by many others, in particular Karim Adel Shams Aldein Alkhouly, Marian Caliebe, and Gulnaz Gahramanova. These studies have been partly financially supported by the DFG within our research group PolarCoN and by the EU in our project ALIGHT.

References

- [1] T. Meisch, “Doping Behavior of (11 $\bar{2}$ 2) GaN Grown on Patterned Sapphire Substrates”, Annual Report, Inst. of Optoelectronics, Ulm University, pp. 13–20, 2014.
- [2] F. Scholz, “Semipolar GaN grown on foreign substrates: a review”, *Semicond. Sci. Technol.*, vol. 27, pp. 024002-1–15, 2012.
- [3] S.H. Park and S.L. Chuang, “Crystal-orientation effects on the piezoelectric field and electronic properties of strained wurtzite semiconductors”, *Phys. Rev. B*, vol. 59, pp. 4725–4737, 1999.

-
- [4] N. Okada, A. Kurisu, K. Murakami, and K. Tadatomo, “Growth of semipolar (11 $\bar{2}$ 2) GaN layer by controlling anisotropic growth rates in r -plane patterned sapphire substrate”, *Appl. Phys. Express*, vol. 2, pp. 091001-1–3, 2009.
- [5] M. Caliebe, T. Meisch, B. Neuschl, S. Bauer, J. Helbing, D. Beck, K. Thonke, M. Klein, D. Heinz, and F. Scholz, “Improvements of MOVPE grown (11 $\bar{2}$ 2) oriented GaN on pre-structured sapphire substrates using a SiN_x interlayer and HVPE overgrowth”, *Phys. Status Solidi C*, vol. 11, pp. 525–529, 2014.
- [6] T. Meisch, R. Zeller, S. Schörner, K. Thonke, L. Kirste, T. Fuchs, and F. Scholz, “Doping behavior of (11 $\bar{2}$ 2)-GaN grown on patterned sapphire substrates”, *Phys. Status Solidi B*, vol. 253, pp. 164–168, 2016.
- [7] U. Kaufmann, P. Schlotter, H. Obloh, K. Köhler, and M. Maier, “Hole conductivity and compensation in epitaxial GaN:Mg layers”, *Phys. Rev. B*, vol. 62, pp. 10867–10872, 2000.
- [8] B. Šantić, “Statistics of the Mg acceptor in GaN in the band model”, *Semicond. Sci. Technol.*, vol. 21, pp. 1484–1487, 2006.
- [9] S.C. Cruz, S. Keller, T.E. Mates, U.K. Mishra, and S.P. DenBaars, “Crystallographic orientation dependence of dopant and impurity incorporation in GaN films grown by metalorganic chemical vapor deposition”, *J. Cryst. Growth*, vol. 311, pp. 3817–3823, 2009.
- [10] F. Scholz, T. Meisch, M. Caliebe, S. Schörner, K. Thonke, L. Kirste, S. Bauer, S. Lazarev, and T. Baumbach, “Growth and doping of semipolar GaN grown on patterned sapphire substrates”, *J. Cryst. Growth*, vol. 405, pp. 97–101, 2014.
- [11] J. Wang, Y. Gao, S. Alam, and F. Scholz, “Mg doping of 3D semipolar InGa_N/Ga_N-based light emitting diodes”, *Phys. Status Solidi A*, vol. 211, pp. 2645–2649, 2014.
- [12] D.V. Dinh, M. Akhter, S. Presa, G. Kozłowski, D. O’Mahony, P.P. Maaskant, F. Brunner, M. Caliebe, M. Weyers, F. Scholz, B. Corbett, and P.J. Parbrook, “Semipolar (11 $\bar{2}$ 2) InGa_N light-emitting diodes grown on chemically-mechanically polished Ga_N templates”, *Phys. Status Solidi A*, vol. 212, pp. 2196–2200, 2015.

Iron Doping in Hydride Vapor Phase Epitaxy of GaN

Martin Klein and Ferdinand Scholz

In order to overcome problems with non-uniform iron (Fe) doping in our GaN layers grown by hydride vapor phase epitaxy, we have optimized the construction of our ferrocene doping channel. By pre-heating the hydrogen carrier gas before entering the hot bubbler, a constant Fe supply could be established. Moreover, losses of the precursor gas in the reactor could be minimized by a re-design of the ferrocene mini-showerhead. In consequence, an about 1 mm thick free-standing GaN layer containing a uniform Fe concentration of $2 \cdot 10^{18} \text{ cm}^{-3}$ exhibited a specific resistivity of $10^7 \Omega\text{cm}$ at room temperature.

1. Introduction

Although GaN-based heterostructures have enabled the realization of many modern semiconductor devices like high-brightness blue and green LEDs, laser diodes, and high-power high-frequency field effect transistors, there are still many issues to be optimized for such devices. Most work is still done on foreign substrates like sapphire or SiC, which leads to fairly large defect densities in the epitaxial structures. Homoepitaxial growth on GaN wafers would be preferable, however, the availability of such substrates is still very limited. Therefore, our studies concentrate since several years on the growth of thick GaN layers by hydride vapor phase epitaxy (HVPE; see, e.g., our previous Annual Reports). Particularly, we are investigating the possibilities to realize semi-insulating GaN layers by iron doping in HVPE [1]. In order to improve the doping concentration control, we have attached a metalorganic gas channel to our HVPE system enabling to supply ferrocene (bis-cyclopentadienyl-iron, Cp_2Fe) as Fe source. However, first experiments resulted in a very non-uniform doping profile with a large Fe peak after switching on the precursor channel, while the remaining layer contained nearly about an order of magnitude less [Fe] [1]. Hence, the average Fe concentration in our layer of about $1\text{--}2 \cdot 10^{17} \text{ cm}^{-3}$ was too small to compensate the parasitic background doping and to lead to semi-insulating behavior of our GaN layers. This required a redesign of our precursor channel, which will be described in this report along with the obtained results.

2. Experimental

These studies have been performed in our horizontal HVPE reactor, which contains 5 separated heating zones. Liquid Ga, positioned in zone II at a temperature of 850°C , is transported by HCl to the substrate in heating zone IV, where the epitaxial growth takes place at typical temperatures of 1050°C . Ammonia (NH_3) is used as nitrogen precursor. As described in our last report, the ferrocene is transported by H_2 from its bubbler into

an additional quartz tube in the center of our reactor close to the growth zone. Owing to the high ferrocene bubbler temperature (see below), all gas lines connecting the bubbler and the HVPE reactor were heated by heating tapes to temperatures above 95 °C. As ferrocene would get lost by decomposing in the hot environment of our HVPE reactor, we mix it with HCl inside zone I of the HVPE reactor near to the reactor inlet to form FeCl₂ which then can be transported forward to the substrate. Details of this construction are described in [1].

The grown layers have been evaluated — besides standard characterization — by van der Pauw Hall experiments. In some samples, the Fe concentration has been directly determined by secondary ion mass spectrometry (SIMS), performed by Lutz Kirste *et al.* (Fraunhofer Institute of Solid State Physics, Freiburg).

3. Optimization of Doping Channel

3.1 Pre-heating of carrier gas

As mentioned above, when switching on our Fe precursor channel gas flow in our previous experiments, we had observed a peak Fe doping of up to $2 \cdot 10^{19} \text{ cm}^{-3}$ which then decreased rapidly to an average value of $1\text{--}2 \cdot 10^{17} \text{ cm}^{-3}$. Due to the very low vapor pressure of ferrocene, such values only could be obtained for bubbler temperatures of 95 °C. However, according to our conventional metalorganic precursor channel construction, the ferrocene bubbler was flushed with “cool” H₂ of about 20 °C (room temperature). Moreover, it must be considered that ferrocene is still solid even at 95 °C. Therefore, we tentatively explain the observed doping peak by a transportation of a large amount of ferrocene according to its vapor pressure at 95 °C only in the very first moment. However, then the “cool” H₂ carrier gas locally decreases the ferrocene temperature and also its vapor pressure. This leads to a reduced ferrocene uptake, keeping in mind a fairly low thermal conductivity of the solid ferrocene, whereas in a liquid material, the carrier gas bubbling would lead to a mixing of the material and hence to a much weaker temperature gradient.

Therefore, it is obvious that a pre-heating of the H₂ carrier gas would decrease our problem. We connected a coil of several windings of our H₂ precursor supply line connected to the inlet of the ferrocene bubbler, which was immersed into the thermo-bath liquid of our ferrocene bubbler. At a typical flow of 40 sccm, the carrier gas needs about 20 s to flow through this coil, which should be enough to heat up to the bubbler temperature of 95 °C. Indeed, we now could establish fairly uniform Fe doping concentrations during the growth of several hours.

3.2 Optimization of showerhead

After a few experiments, we observed black depositions solely at the first two of six small outlet holes in the showerhead which is responsible for distributing the FeCl₂ evenly over the growth region. This indicates that most of the dopant is leaving the showerhead at the upstream end of the growth zone. Due to the reactor geometry, the general flow of the carrier and source gases inside the growth zone is pointing backwards. Moreover, other

tests indicated a leakage between the supply tube and the showerhead as a consequence of a gas blocking in the showerhead. This means that in this configuration a significant part of the FeCl_2 flow is transported away from the wafer, before it can contribute to any doping of the layer.

Therefore, a new showerhead was constructed which only contains one larger elliptical outlet hole directly over the growth zone instead of a few small ones.

By applying all construction details discussed above, two Fe-doped GaN layers with a thickness of about 1 mm have been deposited on templates grown by metalorganic vapor phase epitaxy. Facilitated by a hexagonal SiN mask, they spontaneously separated from the sapphire substrate by the thermal expansion mismatch between GaN and sapphire [2]. On the sample depicted in Fig. 1, a uniform Fe concentration of $2 \cdot 10^{18} \text{ cm}^{-3}$ has been determined by SIMS (Fig. 3) at several positions. However, the crystalline quality of this sample was not good enough for Hall experiments due to many internal cracks etc. Therefore, we used an optimized hexagonal SiO_2 mask for strain management for the second sample shown in Fig. 2. Although the self-separation did not work properly in the center of this sample, we could perform Hall experiments over a wide temperature range from room temperature up to 1000 K on the other areas confirming a semi-insulating behavior with a specific resistivity of about $10^7 \Omega\text{cm}$ at room temperature.



Fig. 1: Free-standing Fe-doped GaN sample on a template with $30 \mu\text{m}$ mask period. Fe content according to SIMS: $2 \cdot 10^{18} \text{ cm}^{-3}$.



Fig. 2: Partly separated layer grown on a template with $15 \mu\text{m}$ mask period. According to van der Pauw Hall experiments: specific resistivity $\rho = 10^7 \Omega\text{cm}$.

4. Conclusion

In order to establish a controllable iron doping source for the growth of Fe-doped GaN, we have improved the metalorganic gas channel connected to our HVPE reactor. Owing to the low vapor pressure of ferrocene, a high bubbler temperature is required. Therefore,

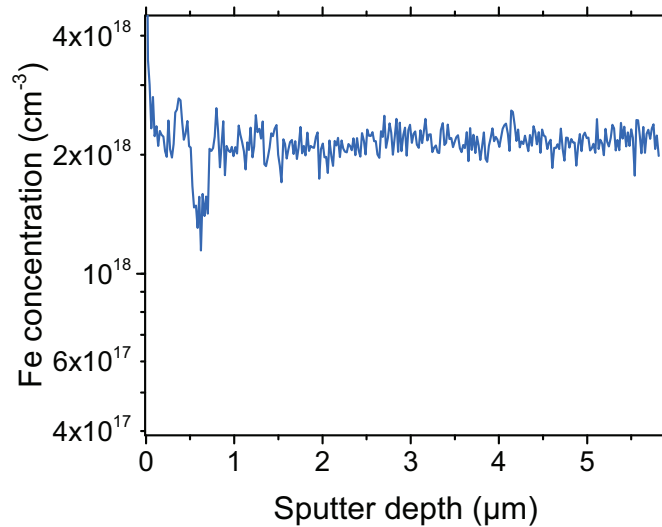


Fig. 3: SIMS profile of a free-standing GaN sample grown with ferrocene carrier gas pre-heating, measured down from the sample surface.

a pre-heating of the carrier gas was implemented, which stabilized the Fe supply over the full duration of an epitaxial run. Moreover, precursor gas losses in the reactor by unwanted backpressure could be minimized by changing the outlet hole design of the Fe showerhead. Now, uniformly doped thick GaN layers could be grown demonstrating semi-insulating behavior in temperature dependent Hall experiments.

Acknowledgment

We are grateful for the strong technical and scientific support by many others, in particular K. Thonke and his group for optical spectroscopy and electrical measurements and L. Kirste (Fraunhofer IAF Freiburg) for SIMS evaluations of our samples. We are also grateful to our project partner Aixtron helping to optimize our precursor channel. These studies have been financially supported by the Bundesministerium für Bildung und Forschung under contract no. 16BM1205 (TeleGaN).

References

- [1] M. Klein, “Ferrocene doping in horizontal hydride vapor phase epitaxy”, Annual Report, Inst. of Optoelectronics, Ulm University, pp. 53–60, 2014.
- [2] F. Lipski, T. Wunderer, S. Schwaiger, and F. Scholz, “Fabrication of freestanding 2”-GaN wafers by hydride vapour phase epitaxy and self-separation during cooldown”, *Phys. Status Solidi A*, vol. 207, pp. 1287–1291, 2010.

GaInN Quantum Wells as Optoelectronic Transducers for Biosensing of Ferritins

Dominik Heinz

In this work, investigations on gallium indium nitride (GaInN) quantum well structures as optochemical transducers in biosensing are presented. In contrast to the conventional electrical read-out of III-nitride-based sensors, a purely optical photoluminescence read-out is performed. Particularly, optical investigations of the iron-storage molecule ferritin deposited on GaInN quantum wells are presented. A significant spectral shift of the quantum well photoluminescence is observed for varying iron-load of ferritin.

1. Introduction

Currently, (bio)chemical sensing methods are often based on optical technologies [1–7]. Fluorescent labels which can be selectively linked by antibodies to different biomolecules [5] or even cells [8] are frequently applied. Most prominently, fluorescent markers are used in enzyme-linked immunosorbent assays (ELISA) which enables analytics down to the picomolar range [3] or in single molecule real time (SMRT) sequencing using fluorescent nucleotides [4, 5]. Today, the throughput in molecular analytics is often limited by the very weak light intensity of such fluorophors [3–5]. In particular, the signal-to-noise ratio is a crucial quantity for single molecule analytics [4, 5]. Fluorescent labels often suffer from photobleaching effects which limits the signal-to-noise ratio significantly [3, 9] or antibodies are not sensitive to specific molecular properties [10, 11].

As unbound iron is toxic, the iron-storage molecule ferritin plays an important role in the regulation of the iron concentration inside the human body [10]. The globular protein ferritin reversibly stores up to 4500 iron atoms inside its cavity where the ions undergo a mineralization process [10]. The concentration of ferritin molecules in human blood is typically determined using immunoassays. It is frequently monitored as biomarker in order to determine the iron status of the body [9, 10]. Ferritin bound iron is reported as a superior biomarker compared to ferritin protein levels [11]. Particularly, iron overload can be distinguished from an inflammation which also influences ferritin protein levels [11]. Additionally, other diseases such as hepatitis or cancer can influence the ferritin protein concentration [11]. A malfunction of the iron-incorporation and storage of the ferritin molecule is associated with Alzheimer's disease where higher concentrations of ferritin bound aluminum are found [12]. However, common antibodies used in immunoassays are only sensitive to the ferritin protein concentration but not to the iron load of the molecule itself [10, 11]. In contrast to immunoassays, determination of ferritin bound iron requires sophisticated methods such as species-specific isotope dilution mass spectrometry [10].

In recent years, gallium nitride (GaN) established as an excellent material system for general lighting and lasing applications in the visible spectral range. Besides classical applications in optoelectronics, group III-nitrides find increasing interest in (bio)chemical sensing [13–17]. Particularly, nanostructures such as nanowires are in the focus of research [13, 18–22]. Typically, nanostructures require rather sophisticated lithographic and epitaxial methods for their realization. Many studies involve an electrical read-out of nanostructures in (bio)chemical sensing [20–22]. However, group III-nitrides are expected to be particularly suited for optical sensing applications which so far has been rarely studied [13, 18, 19]. In contrast to other material systems, group III-nitrides benefit from an excellent chemical stability [23], biocompatibility [16, 17], optoelectronic properties [13, 18, 19], and polarity dependent piezoelectric properties [24, 25] which might be particularly useful in (bio)chemical sensing. In fact, the highest occupied and lowest unoccupied orbitals of many biomolecules match very well to the large bandgap of group III-nitrides [26].

In this work, an alternative “label-free” approach for molecular analytics without application of fluorophors is demonstrated using the stable photoluminescence (PL) of GaInN quantum wells. Particularly, the application of planar GaInN quantum well structures as optoelectronic transducers for sensing ferritin bound iron is investigated (Fig. 1). Planar, near-surface GaInN quantum wells allow a very flexible and reproducible arrangement of the optoelectronic properties compared to more sophisticated nanostructures. All investigations are based on the spectral and intensity changes of the GaInN quantum well luminescence in presence of ferritin with varying iron-load.

2. Experimental

GaInN quantum well structures are grown in a commercial Aixtron AIX200/RF metal organic vapor phase reactor using ammonia (NH_3), trimethylgallium (TMGa), trimethylaluminum (TMAI), triethylgallium (TEGa), and trimethylindium (TMIn) as precursors. Ultra-pure hydrogen and nitrogen are applied as carrier gases.

First, a thin oxygen-doped aluminium nitride (AlN) nucleation layer is grown on *c*-oriented sapphire wafers with a miscut of 0.3° towards the *a*-direction. Subsequently, a Ga-polar GaN buffer layer with a thickness of about $1\ \mu\text{m}$ is realized followed by five GaInN multi quantum wells with a nominal thickness of $3\ \text{nm}$ and $7\ \text{nm}$ GaN barrier. In order to enable a sensitivity of the quantum wells to the biomolecules at the surface, a thin GaN cap layer with a thickness of about $7\ \text{nm}$ is realized.

Before deposition, the GaInN quantum well surface is hydroxilated using a mixture of sulfuric acid (H_2SO_4) and hydrogen peroxide (H_2O_2) with a ratio of 1:1 for 5 min. Subsequently, the samples are rinsed in deionized water and dried under nitrogen flow. Ferritin and apoferritin (corresponds to ferritin without iron-load) from horse spleen are purchased from Sigma-Aldrich und purified using dialysis. In particular, the saline and glycol buffer solutions of the biomolecules are substituted by deionized water. A concentration of about $2\ \mu\text{mol dm}^{-3}$ of (apo)ferritin in deionized water is realized and deposited on the hydroxilated GaInN quantum well surface.

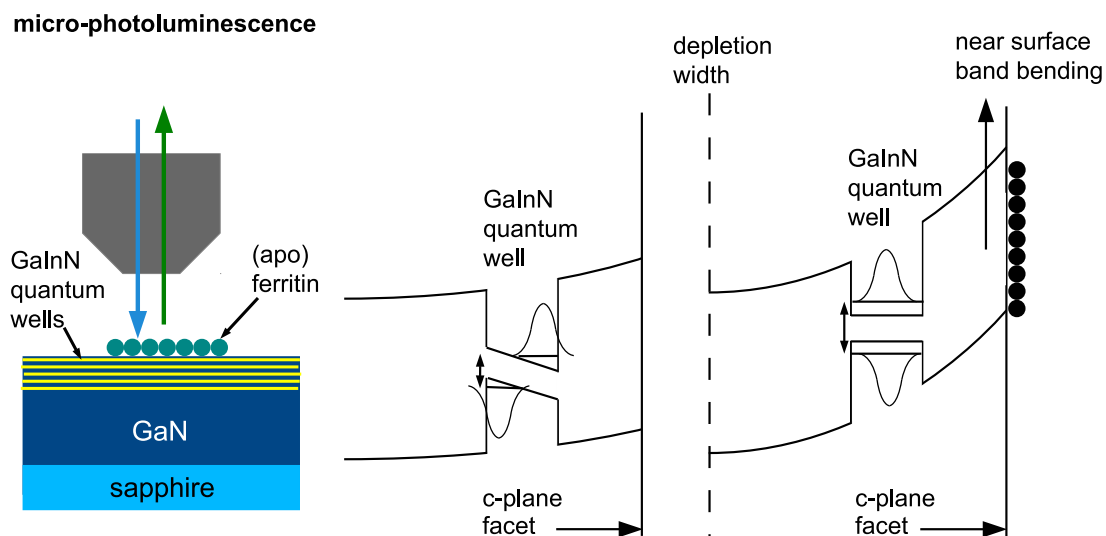


Fig. 1: Schematic illustration of the micro-photoluminescence setup for front side excitation of modified GaInN quantum well structures (left). Near-surface band structure of a polar single GaInN quantum well surface without biomolecule modification (middle) corresponding band structure with increasing band bending after adsorption of oxidizing molecules (right).

Photoluminescence measurements are performed using a micro-photoluminescence setup with mirror objective (Fig. 1). A HeCd laser with main emission wavelength at 325 nm is applied for excitation of the quantum well photoluminescence. The optical read-out is performed using a monochromator and a liquid nitrogen-cooled CCD camera.

Local backside excitation PL experiments are performed using backside polished GaInN quantum well structures. GaInN quantum well samples are mounted on a pinhole in order to allow local measurements before and after deposition of the biomolecules at the same position on the sample surface. A blue laser diode with an emission wavelength at 405 nm is used for resonant excitation of the quantum wells in order to avoid absorption inside the GaN buffer layer. The PL read-out is performed from the front side.

3. Influence of Ferritin Bound Iron on the GaInN Quantum Well Photoluminescence

Ferritin and apoferritin are locally deposited on a hydroxylated planar structure containing 5 GaInN quantum wells. Photoluminescence spectra measured from the front side are shown in Fig. 2.

A significant spectral shift and an intensity variation of the local photoluminescence response is observed after deposition of the biomolecules on the surface. In order to exclude the influence of local fluctuations of the quantum well photoluminescence, several local measurements are performed on ferritin and apoferritin areas.

A mean spectral red-shift of about 2.4 nm and an intensity increase of about 35% is observed for the areas where apoferritin is deposited with respect to ferritin. Regarding the Ga-polarity and *c*-orientation of the GaInN quantum wells, a red-shift for apoferritin

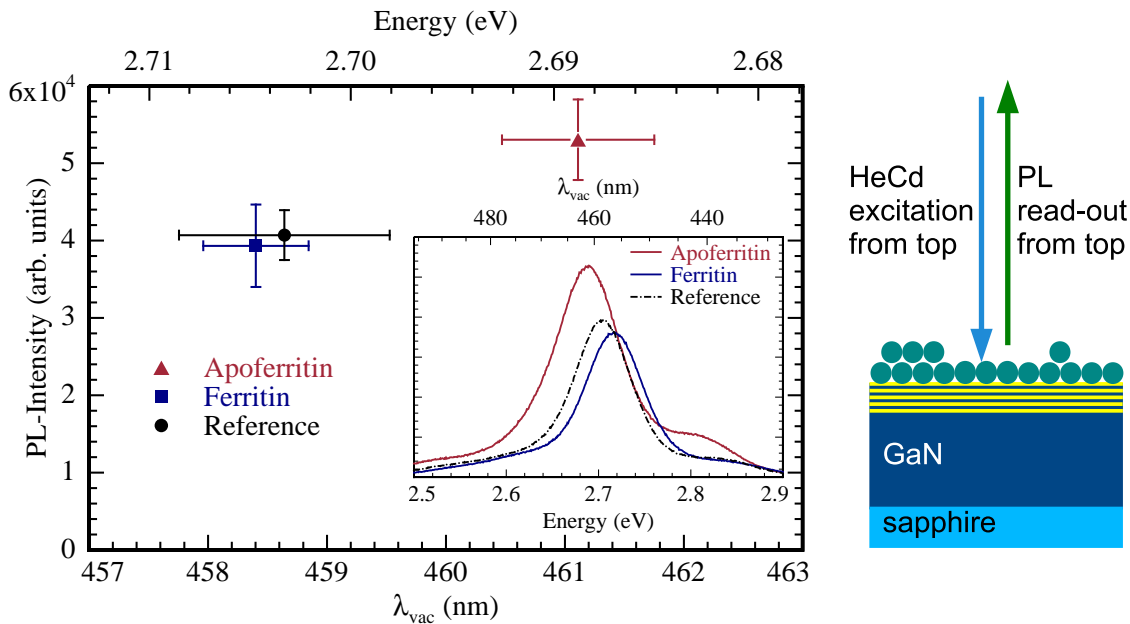


Fig. 2: Micro-photoluminescence of planar $5\times$ GaInN multi quantum wells with ferritin and apoferritin surface modification and corresponding reference structures without modification (left). Error bars are mainly caused by local fluctuations of the quantum well PL and local inhomogeneity of the deposited biofilm thickness (right).

corresponds to a reduction of the initially upward surface band bending. A reduced near-surface band bending leads to an increased tilting of the quantum well band structure and hence to an increased quantum confined Stark effect (QCSE). Therefore, apoferritin can be assumed to behave as a reducing agent which attracts holes at the GaN surface and hence reduces the band bending.

Indeed, it is reported in literature that apoferritin can bind different kinds of positively charged metal ions, particularly Fe^{2+} and Fe^{3+} ions [27]. The binding affinity is reported to be pH-dependent as protons in the buffer solutions compete with other metal ions [27, 28]. Ferritins are reported to obey a negative surface potential which attracts cations [29]. Surprisingly, the photoluminescence intensity slightly increased after apoferritin deposition. A reduced overlap of the electron and hole wave functions and reduced radiative recombination probability is expected due to the increased QCSE. The intensity increase might be explained by an improved light extraction due to the increased surface roughness or by reduced non-radiative surface recombination.

In contrast to apoferritin, a tendency for a blue shift with respect to the reference structure without surface modification is observed for ferritin. It is expected that the reducing nature of apoferritin is significantly weakened or overcompensated due to the incorporation of positively charged ions, which is indeed observed. The iron concentration inside the ferritin molecules is expected to vary. Unfortunately, local fluctuations of the quantum well PL and large error bars inhibit a clear statement about the electron transfer for ferritin. A spectral blue shift corresponds to an oxidizing nature of ferritin. This corresponds to an increase of the near-surface band bending and reduced QCSE.

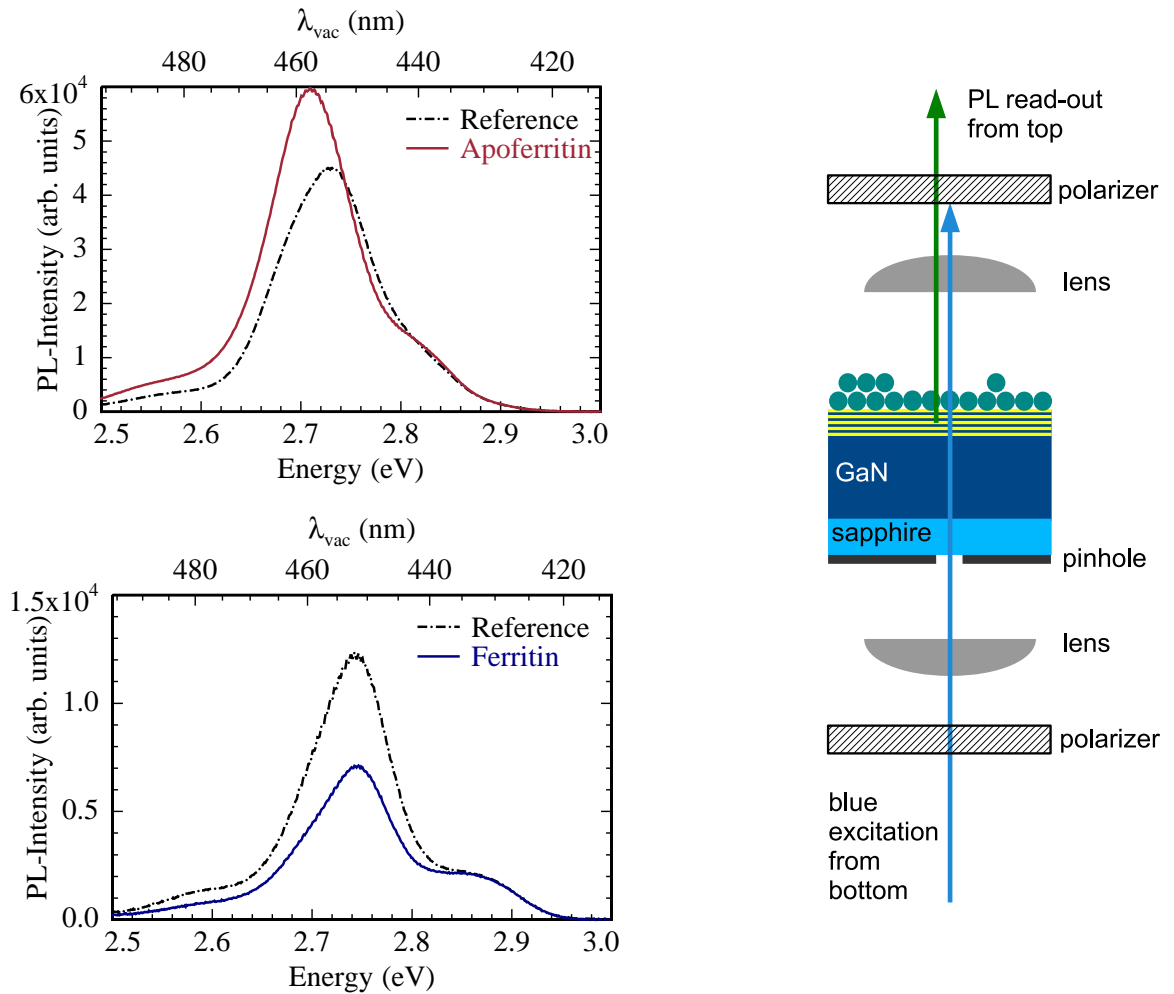


Fig. 3: Local backside excitation PL measurement using double polished $5\times$ GaInN multi quantum well structures (left) for apoferritin (top) and ferritin (bottom) modified surfaces. Schematic illustration of the setup (right): a polarized blue 405 nm laser is used for resonant excitation of the quantum wells which is selectively separated from the PL using a second polarizer. The sample is mounted on a pinhole to excite the same position before and after deposition of the biomolecules.

In order to exclude the influence of local variations of the quantum well PL, local backside excitation experiments are performed. The polished sapphire backside of a planar multi-quantum well structure is mounted on a pinhole (Fig. 3). As GaN is absorbing in the UV spectral range, a blue laser diode is used for optical resonant excitation of the GaInN quantum well PL. The optical PL read-out is again performed on the quantum well side.

Again a spectral redshift is found after deposition of apoferritin biomolecules on the quantum well surface compared to the local reference measurement without surface modification. A slightly higher intensity is found which might be again explained by improved PL light extraction on the quantum well surface. The result is in very good agreement with the previously described investigations on the front side. In contrast, a reduced spectral shift with a slight tendency for smaller wavelength is found for ferritin molecules

which again matches with our expectations. However, the PL quenching is much more pronounced compared to our frontside excitation experiments which might be a local effect. Obviously, the overall iron load of (apo)ferritin molecules seems to have a strong influence on the optoelectronic properties of polar GaInN quantum wells. A reduced spectral shift of ferritin molecules might be explained by a reduced binding affinity of ferritin for positive charges compared to apoferritin.

4. Summary

The realization and application of planar GaInN quantum well structures as optical transducer elements in biosensing is demonstrated. Ferritin molecules on the surface of such structures strongly influence the near-surface quantum well PL depending on the iron-load of the molecules. A significant spectral redshift of the photoluminescence is observed in the presence of apoferritin caused by the externally induced QCSE. The results might be particularly useful for new “label-free” optical sensor concepts without application of fluorophors based on the transducing properties of GaInN quantum wells.

Acknowledgment

Scientific support by L. Wu, M. Spiess, O. Rettig (Institute of Optoelectronics, Ulm University), F. Huber, S. Bauer, K. Thonke (Institute of Quantum Matter / Semiconductor Physics Group, Ulm University), Y. Wu, and T. Weil (Institute of Organic Chemistry III, Ulm University) is gratefully acknowledged. The author thanks R. Rösch for technical support with backside lapping and polishing. This work was financially supported by the Baden-Württemberg Stiftung gGmbH within the projects “Nitridische Nanosäulen für optisch auslesbare Sensoranwendungen” and “Intelligente optoelektronische Biosensoren”.

References

- [1] O.S. Wolfbeis, “Luminescent sensing and imaging of oxygen: fierce competition to the Clark electrode”, *BioEssays*, vol. 37, pp. 921–928, 2015.
- [2] X. Wang and O.S. Wolfbeis, “Optical methods for sensing and imaging oxygen: materials, spectroscopies and applications”, *Chem. Soc. Rev.*, vol. 43, pp. 3666–3761, 2014.
- [3] J.R. Heath and M.E. Davis, “Nanotechnology and cancer”, *Annu. Rev. Med.*, vol. 59, pp. 251–265, 2008.
- [4] M.J. Levene, J. Korlach, S.W. Turner, M. Foquet, H.G. Craighead, and W.W. Webb, “Zero-mode waveguides for single-molecule analysis at high concentrations”, *Science*, vol. 299, pp. 682–686, 2003.
- [5] J. Eid, A. Fehr, J. Gray, K. Luong, J. Lyle, G. Otto *et al.*, “Real-time DNA sequencing from single polymerase molecules”, *Science*, vol. 323, pp. 133–138, 2009.

- [6] M.C. Estevez, M.A. Otte, B. Sepulveda, and L.M. Lechuga, “Trends and challenges of refractometric nanoplasmonic biosensors: a review”, *Anal. Chim. Acta*, vol. 806, pp. 55–73, 2014.
- [7] H.P. Zassenhaus, “Biolayer interferometry measurement of biological targets”, *US Patent 8,512,950*, Aug. 20, 2013.
- [8] A.Y. Fu, C. Spence, A. Scherer, F.H. Arnold, and S.R. Quake, “A microfabricated fluorescence-activated cell sorter”, *Nat. Biotech.*, vol. 17, pp. 1109–1111, 1999.
- [9] A. Ermakova, G. Pramanik, J.M. Cai, G. Algara-Siller, U. Kaiser, T. Weil, Y.K. Tzeng, H.C. Chang, L.P. McGuinness, M.B. Plenio, B. Naydenov, and F. Jelezko, “Detection of a few metallo-protein molecules using color centers in nanodiamonds”, *Nano Lett.*, vol. 13, pp. 3305–3309, 2013.
- [10] Y. Ren and T. Walczyk, “Quantification of ferritin bound iron in human serum using species-specific isotope dilution mass spectrometry”, *Metallomics*, vol. 6, pp. 1709–1717, 2014.
- [11] V. Herbert, E. Jayatilleke, S. Shaw, A.S. Rosman, P. Giardina, R.W. Grady, B. Bowman, and E.W. Gunter, “Serum ferritin iron, a new test, measures human body iron stores unconfounded by inflammation”, *Stem Cell*, vol. 15, pp. 291–296, 1997.
- [12] P. De Sole, C. Rossi, M. Chiarpotto, G. Ciasca, B. Bocca, A. Alimonti, A. Bizzarro, C. Rossi, and C. Masullo, “Possible relationship between Al/ferritin complex and Alzheimer’s disease”, *Clin. Biochem.*, vol. 46, pp. 89–93, 2013.
- [13] J. Teubert, P. Becker, F. Furtmayr, and M. Eickhoff, “GaN nanodiscs embedded in nanowires as optochemical transducers”, *Nanotechnology*, vol. 22, pp. 275505-1–5, 2011.
- [14] N. Chaniotakis and N. Sofikiti, “Novel semiconductor materials for the development of chemical sensors and biosensors: a review”, *Anal. Chim. Acta*, vol. 615, pp. 1–9, 2008.
- [15] B. Chu, C. Chang, S.J. Pearton, J. Lin, and F. Ren, “Recent advances in wide-bandgap semiconductor biological and gas sensors”, Chap. 2 in *Semiconductor Device-Based Sensors for Gas, Chemical, and Biomedical Applications*, F. Ren and S. Pearton (Eds.), p. 43, Boca Raton: CRC Press, 2011.
- [16] I. Cimalla, F. Will, K. Tonisch, M. Niebelschütz, V. Cimalla, V. Lebedev, G. Kittler, M. Himmerlich, S. Krischok, J. Schaefer, M. Gebinoga, A. Schober, T. Friedrich, and O. Ambacher, “AlGaIn/GaN biosensor – effect of device processing steps on the surface properties and biocompatibility”, *Sens. Actuator B*, vol. 123, pp. 740–748, 2007.
- [17] I. Cimalla, M. Gebinoga, A. Schober, V. Polyakov, V. Lebedev, and V. Cimalla, “AlGaIn/GaN sensors for direct monitoring of nerve cell response”, Chap. 1 in *Semiconductor Device-Based Sensors for Gas, Chemical, and Biomedical Applications*, F. Ren and S.J. Pearton (Eds.), p. 1, Boca Raton: CRC Press, 2011.

- [18] S. Paul, A. Helwig, G. Müller, F. Furtmayr, J. Teubert, and M. Eickhoff, “Optochemical sensor system for the detection of H₂ and hydrocarbons based on InGaN/GaN nanowires”, *Sens. Actuator B*, vol. 173, pp. 120–126, 2012.
- [19] K. Maier, A. Helwig, G. Müller, P. Becker, P. Hille, J. Schörmann, J. Teubert, and M. Eickhoff, “Detection of oxidising gases using an optochemical sensor system based on GaN/InGaN nanowires”, *Sens. Actuator B*, vol. 197, pp. 87–94, 2014.
- [20] C.P. Chen, A. Ganguly, C.Y. Lu, T.Y. Chen, C.C. Kuo, R.S. Chen, W.H. Tu, W.B. Fischer, K.H. Chen, and L.C. Chen, “Ultrasensitive in situ label-free DNA detection using a GaN nanowire-based extended-gate field-effect-transistor sensor”, *Anal. Chem.*, vol. 83, pp. 1938–1943, 2011.
- [21] J. Sim, K. Kim, S. Song, and J. Kim, “Suspended GaN nanowires as NO₂ sensor for high temperature applications”, *Analyst*, vol. 138, pp. 2432–2437, 2013.
- [22] W. Lim, J.S. Wright, B.P. Gila, J.L. Johnson, A. Ural, T. Anderson, F. Ren, and S.J. Pearton, “Room temperature hydrogen detection using Pd-coated GaN nanowires”, *Appl. Phys. Lett.*, vol. 93, pp. 072109-1–3, 2008.
- [23] K.A. Son, A. Liao, G. Lung, M. Gallegos, T. Hatake, R.D. Harris, L.Z. Scheick, and W.D. Smythe, “GaN-based high-temperature and radiation-hard electronics for harsh environments”, in *Micro- and Nano-Harsh Environment Sensors*, T. George, M.S. Islam, and A.K. Dutta (Eds.), Proc. SPIE 7679, pp. 76790U-1–8, 2010.
- [24] Y.L. Wang, F. Ren, U. Zhang, Q. Sun, C.D. Yerino, T.S. Ko, Y.S. Cho, I.H. Lee, J. Han, and S.J. Pearton, “Improved hydrogen detection sensitivity in N-polar GaN Schottky diodes”, *Appl. Phys. Lett.*, vol. 94, pp. 212108-1–3, 2009.
- [25] K. Hyeon Baik, H. Kim, S.N. Lee, E. Lim, S.J. Pearton, F. Ren, and S. Jang, “Hydrogen sensing characteristics of semipolar (11 $\bar{2}$ 2) GaN Schottky diodes”, *Appl. Phys. Lett.*, vol. 104, pp. 072103-1–3, 2014.
- [26] M. Stutzmann, J.A. Garrido, M. Eickhoff, and M.S. Brandt, “Direct biofunctionalization of semiconductors: a survey”, *Phys. Status Solidi A*, vol. 203, pp. 3424–3437, 2006.
- [27] R. Laghaei, D.G. Evans, and R.D. Coalson, “Metal binding sites of human H-chain ferritin and iron transport mechanism to the ferroxidase sites: a molecular dynamics simulation study”, *Proteins*, vol. 81, pp. 1042–1050, 2013.
- [28] E. Paques, A. Paques, and R. Chrichton, “A kinetic study of the mechanism of ferritin formation: the effects of buffer, of pH, and of the iron content of the molecule”, *J. Mol. Catal. Chem.*, vol. 5, pp. 363–375, 1979.
- [29] T. Douglas and D.R. Ripoll, “Calculated electrostatic gradients in recombinant human H-chain ferritin”, *Protein Sci.*, vol. 7, pp. 1083–1091, 1998.

Investigation of AlBGaN Structures for UV-Lighting

Oliver Rettig

In this work, a brief introduction in the advantages of AlBGaN as a material for UV-lighting devices will be given. As a template, AlN layers will be developed based on knowledge already obtained in our group. Also new approaches will be discussed to further increase the AlN crystal quality.

1. Introduction

Highly efficient blue light-emitting diodes (LED) already exist on the basis of Ga(In)N [1] enabling the generation of white light. Also LEDs in the UV range, especially the UV-C range (~ 270 nm), have many applications since they can be used for sterilization and disinfection of water and air [2, 3], phototherapy [2], fluorescence analytical systems [3], bio-agent detection [4], spectrometry [5] and currency validation [5]. However, LEDs in the UV spectral range are typically much less efficient [2] due to the challenges of growing high quality AlN layers with low threading dislocation density (TDD). Such dislocations penetrating through the optically active layers, drastically decrease the efficiency of the device. Due to lattice mismatch between the sapphire substrate used for overgrowth and AlN, defects are generated. To minimize lattice mismatch between the substrate and the AlGa_xN with very high Al-content as well as reducing the absorption of light in the substrate, UV-LEDs are not grown on GaN- but on AlN substrates [6]. Moreover, lattice mismatch between layers of different Al content lead to further problems, e.g., further defect generation or even cracking. Due to the quantum confined Stark effect (QCSE), piezoelectric fields reduce the overlap of the electron and hole wave functions and, hence, the recombination probability in the active quantum wells decreases.

Boron containing AlGa_xN layers enable a further degree of freedom in lattice matching the optically active layers to the AlN templates since BN has an approximately 18% smaller lattice constant compared to AlN [7]. Hence, strain and TDD can be reduced which normally negatively affect the efficiency of the optoelectronic device. Lattice matching also leads to reduced piezoelectric fields in the active layers which also helps increasing the efficiency of the LEDs.

However, boron exhibits a poor solubility into AlGa_xN [8]. To overcome this problem high temperature growth up to 1400 °C will be applied. Fortunately, only 3–4% of boron are sufficient to compensate compressive strain in Al_{0.75}Ga_{0.25}N grown on AlN.

Therefore, we recently have started a project which will clarify whether boron incorporation helps to reduce the strain in AlGa_xN hetero structures without deteriorating the crystal quality. Only little information about Al_xB_yGa_{1-x-y}N can be found in literature [9–11]. Many fundamental properties like band gap as a function of the composition

and donor/acceptor ionization energies are still unknown or uncertain. Here, we report about our first steps to optimize the growth of AlN layers on sapphire which will be used as templates for our later AlBGaN growth studies.

2. Experimental Details

The MOVPE reactor used for this study is a low-pressure horizontal reactor (Aixtron AIX-200/4 RF-S) with a high-temperature susceptor kit enabling growth temperatures up to 1400 °C. All group III-nitrides are grown on standard (0001) sapphire substrates with an offset of 0.3° towards the m-plane. Trimethylaluminium (TMAI), trimethylgallium (TMGa), trimethylindium (TMIn), triethylboron (TEB), and ammonia are used as precursors.

For characterization, a high resolution X-ray diffractometer (Bruker Discover D8) is used to study the crystal quality of the samples.

Photoluminescence spectroscopy is performed by using an argon fluoride excimer laser as excitation source which operates at a wavelength of 193 nm.

3. Growth of the AlN Template

Thapa and Qi [12, 13] have already investigated the growth of AlN layers and optimized the growth parameters.

Hence, we started our investigations by following their proposed recipes [14]: AlN templates are grown in a two-step process. First, an oxygen doped approximately 20 nm thick AlN nucleation layer is grown. This is followed by a faster grown undoped AlN layer with a mixture of carrier gases $N_2 : H_2 = 2 : 1$. After nucleation layer growth, a 10 min low temperature annealing step is employed at 500 °C. The TMAI and ammonia mass flows during layer growth are 10 μ mol/min and 10 mmol/min, respectively which results in a V/III ratio of approximately 1000. The reactor pressure is set to 35 hPa and the surface temperature is set to 1085 °C which is measured pyrometrically from the top.

It was found that the addition of TMIn during growth helps improving the adsorption and surface mobility of the Al-precursors and hence enhances the crystal quality [12]. Due to the high growth temperature, indium is not incorporated effectively into the AlN layer [15].

XRD results for a 500 nm thick layer show very narrow reflections with a full width at half maximum (FWHM) of 92 arcsec and 1163 arcsec for the (0002) and (10 $\bar{1}$ 2) peaks, respectively.

Figure 1 shows the XRD measurement of the (10 $\bar{1}$ 2) reflection with a pseudo-Voigt regression.

The TDD can be roughly estimated by [16]

$$D = \frac{\beta}{4.35 \cdot b} \quad , \quad (1)$$

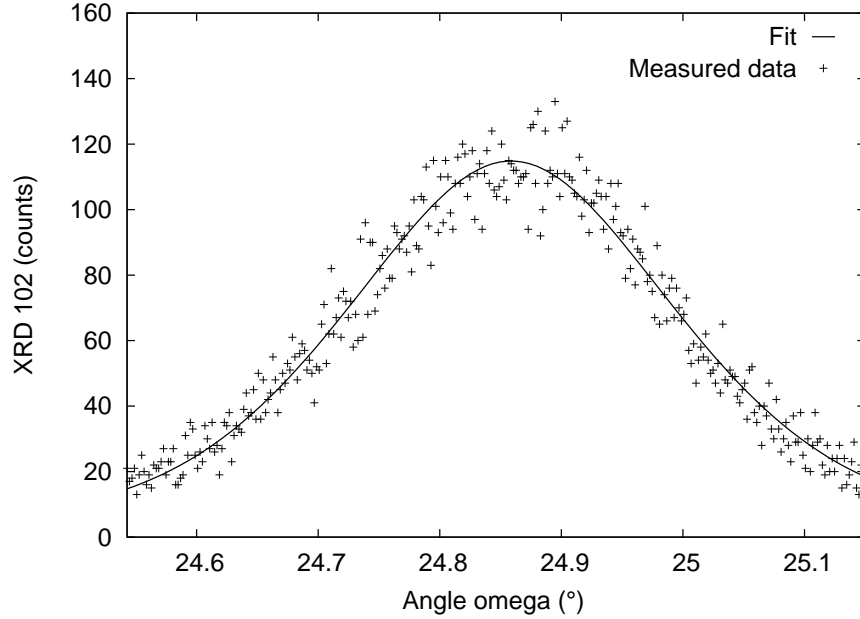


Fig. 1: XRD measurement of the $(10\bar{1}2)$ reflection of a 500 nm thick AlN template with a FWHM of 1163 arcsec.

where

$$\beta = \beta_{\text{hkl}} = \sqrt{(\beta_{\text{screw}} \cdot \cos \chi)^2 + (\beta_{\text{edge}} \cdot \sin \chi)^2} \quad (2)$$

stands for the FWHM of the respective hkl-reflection measured by XRD and b is the length of the Burgers vector of the screw- or edge-type TD, respectively. The angle χ is taken from the position of the hkl-reflection peak of the XRD's Euler cradle. From the FWHM of the (0002) reflection β_{screw} can directly be calculated since $\chi = 0$. For the calculation of the edge-type TDD the FWHM of the $(10\bar{1}2)$ reflection as well as the already obtained value for β_{screw} are used. Hence, on our recent 500 nm AlN templates we can estimate the TDDs to $D_{\text{screw}} = 2 \cdot 10^7 \text{ cm}^{-2}$ and $D_{\text{edge}} = 1 \cdot 10^{10} \text{ cm}^{-2}$.

However, simulations show that in AlGaIn MQW LEDs a TDD in the range of 10^{10} cm^{-2} is too high to achieve an internal quantum efficiency larger than a few percent [2]. Therefore, we need to reduce particularly the FWHM of the $(10\bar{1}2)$ reflection.

There are still possibilities for improvement mentioned in literature. Hirayama et al. suggest a multi-step process with faster and slower growth rates. Also AlGaIn-AlN-multilayers are used to enhance the crystal properties of the template [2]. Since it is possible to install a high temperature setup in our MOVPE, higher growth temperatures will be also investigated. Pulsed growth is also successfully applied to enhance the surface mobility of the Al precursors and hence improve the crystal quality [17]. A very promising method of drastically enhancing the crystal properties is thermal annealing of the AlN template up to 1600 °C [18]. Some groups also improved the crystal quality of the AlN template by an epitaxial lateral overgrowth (ELO) process [19]. All of these approaches will be investigated to get the best possible foundation for further research.

3.1 Modification of the precursor usage

For the slow growth of the AlN:O nucleation layer, a TMAI bubbler at a temperature of 5°C is used. This provides decently low mass flow to achieve thin and controlled nucleation layer growth. However, for the growth of the top layer, a higher growth rate is needed which requires a larger mass flow of the TMAI precursor. For that purpose, a second TMAI bubbler at a temperature of 17°C is applied.

For the growth of boron containing materials, an additional bubbler needs to be installed into our MOVPE. Unfortunately, no spare channel is available. Therefore, one of the TMAI bubblers needs to be replaced. The idea was to find a compromise between slow and fast growth rate resulting in a bubbler temperature of 10°C.

In order to determine which bubbler is better suited for this purpose, we have grown with different bubbler configurations, as displayed in Table 1.

Table 1: Comparison of the the crystal quality obtained with the two TMAI bubblers for a 500 nm thick AlN layer on sapphire.

	sample	T6028Aa	T6029Aa	T6033Aa
nucleation	bubbler	1	1	2
	bubbler temperature (°C)	4	4	10
	pressure (mbar)	1000	400	1400
	source flow (sccm)	25	10	25
layer	bubbler	2	1	2
	bubbler temperature (°C)	17	4	10
	pressure (mbar)	1000	400	1000
	source flow (sccm)	25	22	38
	FWHM (10 $\bar{1}2$)	1500	4200	2100

The pressure as well as the temperature of the bubblers are chosen to keep the TMAI mass flow constant. Therefore, all templates are expected to have the same crystal quality. However, as can be clearly seen, the FWHM of the (10 $\bar{1}2$) reflection changes significantly depending on the bubbler used as precursor source for AlN growth. Neither bubbler one nor bubbler two can be used for both, nucleation and buffer layer growth to achieve the same FWHM as compared to the combination of both. The reason for that behaviour is not known until now. It is supposed that bubbler one might be contaminated since it is a rather old source. However, this contamination seems to help for the growth of a good nucleation layer since the crystal quality is better compared to templates with nucleation layers grown with the second bubbler. Further studies are needed to clarify this issue.

4. Summary

First studies on the growth of AlN templates were performed. Templates with a thickness of 500 nm show a FWHM of the XRD of 92 arcsec and 1162 arcsec for the (0002) and (10 $\bar{1}$ 2) peaks, respectively. This is equal to a TDD of $D_{\text{screw}} = 2 \cdot 10^7 \text{ cm}^{-2}$ and $D_{\text{edge}} = 1 \cdot 10^{10} \text{ cm}^{-2}$. However, for the growth of highly efficient UV-LEDs further improvement needs to be achieved.

5. Acknowledgment

I thank the coauthor J.P. Scholz of the Institute of Quantum Matter, Semiconductor Physics Group at Ulm University and K. Thonke of the same group as well as T. Meisch of the Institute of Optoelectronics at Ulm University for their scientific support. This work was financially supported by the DFG within the framework of the project “Investigations on the epitaxy of AlBGaN-heterostructures for applications in UV-LEDs”.

References

- [1] Y. Narukawa, M. Ichikawa, D. Sanga, M. Sano, and T. Mukai, “White light emitting diodes with super-high luminous efficacy”, *J. Phys. D: Appl. Phys.*, vol. 43, pp. 354002-1–6, 2010.
- [2] M. Kneissl, T. Kolbe, C. Chua, V. Kueller, N. Lobo, J. Stellmach, A. Knauer, H. Rodriguez, S. Einfeldt, Z. Yang, N.M. Johnson, and M. Weyers, “Advances in group III-nitride-based deep UV light-emitting diode technology”, *Semicond. Sci. Technol.*, vol. 26, pp. 014036-1–6, 2011.
- [3] H. Hirayama, S. Fujikawa, N. Noguchi, J. Norimatsu, T. Takano, K. Tsubaki, and N. Kamata, “222–282 nm AlGaN and InAlGaN-based deep-UV LEDs fabricated on high-quality AlN on sapphire”, *Phys. Status Solidi A*, vol. 206, pp. 1176–1182, 2009.
- [4] X. Hu, J. Deng, J.P. Zhang, A. Lunev, Y. Bilenko, T. Katona, M.S. Shur, R. Gaska, M. Shatalov, and A. Khan, “Deep ultraviolet light-emitting diodes”, *Phys. Status Solidi A*, vol. 203, pp. 1815–1818, 2006.
- [5] C. Pernot, M. Kim, S. Fukahori, T. Inazu, T. Fujita, Y. Nagasawa, A. Hirano, M. Ippommatsu, M. Iwaya, S. Kamiyama, I. Akasaki, and H. Amano, “Improved efficiency of 255–280 nm AlGaN-based light-emitting diodes”, *Appl. Phys. Express*, vol. 3, pp. 061004-1–3, 2010.
- [6] M. Bickermann, B.M. Epelbaum, O. Filip, P. Heimann, S. Nagata, and A. Winnacker, “UV transparent single-crystalline bulk AlN substrates”, *Phys. Status Solidi C*, vol. 7, pp. 21–24, 2010.
- [7] T. Akasaka and T. Makimoto, “Flow-rate modulation epitaxy of wurtzite AlBN”, *Appl. Phys. Lett.*, vol. 88, pp. 041902-1–3, 2006.

- [8] C.H. Wei and J.H. Edgar, “Unstable composition region in the wurtzite $B_{1-x-y}Ga_xAl_yN$ system”, *J. Cryst. Growth*, vol. 208, pp. 179–182, 2000.
- [9] T. Akasaka and T. Makimoto, “Flow-rate modulation epitaxy of wurtzite AlBN”, *Appl. Phys. Lett.*, vol. 88, pp. 041902-1–3, 2006.
- [10] A.Y. Polyakov, M. Shin, W. Qian, M. Skowronski, D.W. Greve, and R.G. Wilson, “Growth of AlBN solid solutions by organometallic vapor-phase epitaxy”, *J. Appl. Phys.*, vol. 81, pp. 1715–1719, 1997.
- [11] M. Kurimoto, T. Takano, J. Yamamoto, Y. Ishihara, M. Horie, M. Tsubamoto, and H. Kawanishi, “Growth of BGaN/AlGaN multi-quantum-well structure by metalorganic vapor phase epitaxy”, *J. Cryst. Growth*, vol. 221, pp. 378–381, 2000.
- [12] S. Thapa, *Studies of AlN grown by MOVPE for Electronic and Optoelectronic Applications*, Ph.D. Thesis, Ulm University, Ulm, Germany, 2010.
- [13] H. Qi, *Investigations on AlN Buffer Layer for AlGaN-based Deep Ultraviolet LEDs*, Master Thesis, Ulm University, Ulm, Germany, 2011.
- [14] S. Thapa, C. Kirchner, F. Scholz, G. Prinz, K. Thonke, R. Sauer, A. Chuvilin, J. Biskupek, U. Kaiser, and D. Hofstetter, “Structural and spectroscopic properties of AlN layers grown by MOVPE”, *J. Cryst. Growth*, vol. 298, pp. 383–386, 2007.
- [15] S. Keller, S. Heikman, I. Ben-Yaacov, L. Shen, S.P. DenBaars, and U.K. Mishra, “Indium-surfactant-assisted growth of high-mobility AlN/GaN multilayer structures by metalorganic chemical vapor deposition”, *Appl. Phys. Lett.*, vol. 79, pp. 3449–3451, 2001.
- [16] C. Dunn and E. Kogh, “Comparison of dislocation densities of primary and secondary recrystallization grains of Si-Fe”, *Acta Metallurgica*, vol. 5, pp. 548–554, 1957.
- [17] H. Hirayama, T. Yatabe, N. Noguchi, T. Ohashi, and N. Kamata, “231–261 nm AlGaN deep-ultraviolet light-emitting diodes fabricated on AlN multilayer buffers grown by ammonia pulse-flow method on sapphire”, *Appl. Phys. Lett.*, vol. 91, pp. 071901-1–3, 2007.
- [18] H. Miyake, G. Nishio, S. Suzuki, K. Hiramatsu, H. Fukuyama, J. Kaur, and N. Kuwano, “Annealing of an AlN buffer layer in N_2 -CO for growth of a high-quality AlN film on sapphire”, *Appl. Phys. Express*, vol. 9, pp. 025501-1–4, 2016.
- [19] U. Zeimer, V. Kueller, A. Knauer, A. Mogilatenko, M. Weyers, and M. Kneissl, “High quality AlGaN grown on ELO AlN/sapphire templates”, *J. Cryst. Growth*, vol. 377, pp. 32–36, 2013.

Ph.D. Theses

1. Jan-Philipp Ahl,
Growth and analysis of blue LEDs comprising quaternary AlInGaN,
June 2015.
2. Benedikt Westenfelder,
Elektrische in-situ-TEM-Untersuchungen an Graphen,
July 2015.
3. Dietmar Grimm né Wahl,
*MBE-Wachstum und Charakterisierung anwendungsspezifischer
vertikal emittierender Laserdioden,*
November 2015.

Diploma and Master Theses

1. Ifeanyi Francis Edokam,
Growth and Characterization of $\{11\bar{2}2\}$ Semipolar Gallium Nitride on 100 mm Diameter Patterned Sapphire Substrate,
Master Thesis, January 2015.
2. Sepideh Faraji,
Epitaxy and Characterization of Semi-polar $(10\bar{1}1)$ and $(20\bar{2}1)$ GaN-based Hetero-structures on $(11\bar{2}3)$ and $(22\bar{4}3)$ Patterned Sapphire Substrate,
Master Thesis, January 2015.
3. Raphael Albert Zeller,
Epitaxie und Charakterisierung von semipolaren InGaN / GaN-LEDs auf strukturierten Saphirsubstraten,
Master Thesis, January 2015.
4. Andreas Ziegler,
Optische und elektrische Untersuchungen an GaAs-basierten Phototransistoren,
Master Thesis, January 2015.
5. Haitham Nasr,
Relative Intensity Noise Characterization of Vertical-Cavity Surface-Emitting Lasers,
Master Thesis, April 2015.
6. Stefanie Unseld,
Untersuchung von temperaturabhängigen Effekten in vertikal emittierenden Laserdioden (VCSEL),
Master Thesis, April 2015.
7. Muhammad Asad,
Chemical functionalization of GaN surfaces,
Master Thesis, May 2015.
8. Florian Betz,
Einfluss der Aufbau- und Verbindungstechnik auf die Zuverlässigkeit von vertikal emittierenden Laserdioden,
Diploma Thesis, May 2015.
9. Sushil Tandukar,
Epitaxial growth of $(11\bar{2}2)$ semipolar GaN on sapphire patterned by deep UV-lithography,
Master Thesis, May 2015.
10. Hongfei Wang,
Investigations Into Vertical-Cavity Laser Diodes With Integrated Electrical Heaters,
Master Thesis, June 2015.

11. Markus Polanik,
Charakterisierung von optisch quantenfilmgepumpten Halbleiterscheibenlasern mit kleinem Quantendefekt,
Master Thesis, November 2015.
12. Ze Jiang,
Evaluation of semipolar GaN characterization grown by MOVPE and HVPE for LEDs application,
Master Thesis, December 2015.
13. Sukhjit Singh,
Investigations Into Dynamic Photodiode Characteristics With Optical Heterodyning,
Master Thesis, December 2015.
14. Linyuan Wu,
Functionalization of Ga(In)N nanostructures for optical sensing,
Master Thesis, December 2015.

Bachelor Theses

1. Feihong Song,
Development of the Hall measurement system based on van der Pauw method,
May 2015.
2. Donghao Wu,
Realization of micro-fluidic channels on structured GaN surfaces,
May 2015.

Talks and Conference Contributions

- [1] S. Bader, P. Gerlach, and R. Michalzik, “Novel oxide-free VCSEL with optically controlled current confinement”, *Conf. on Lasers and Electro-Optics Europe, CLEO/Europe 2015*, Munich, Germany, June 2015.
- [2] M. Caliebe, Y. Han, M. Hocker, T. Meisch, C. Humphreys, K. Thonke, and F. Scholz, “Studies with marker layers on semipolar (11-22) oriented GaN grown on (10-12) pre-structured sapphire substrates”, poster at *16th European Workshop on Metalorganic Vapor Phase Epitaxy (EWMOVPE XVI)*, Lund, Sweden, June 2015.
- [3] M. Caliebe, Y. Han, T. Meisch, C. Humphreys, and F. Scholz, “Growth and coalescence studies with marker layers on (11-22) oriented GaN on pre-structured sapphire substrates”, *PolarCoN Winterschool*, Reisenburg, Günzburg, Germany, March 2015.
- [4] M. Caliebe, S. Tandukar, Z. Cheng, T. Meisch, D. Heinz, F. Scholz, A. Plettl, Y. Han, C. Humphreys, M. Hocker, S. Bauer, F. Huber, and K. Thonke, “Influence of trench period and depth on MOVPE grown (11-22) GaN on patterned r-plane sapphire substrates”, *30th DGKK Workshop Epitaxie von III-V-Halbleitern*, Göttingen, Germany, December 2015.
- [5] M. Daubenschütz, P. Gerlach, and R. Michalzik, “Epitaxy-based electro-thermal simulation approach for vertical-cavity surface-emitting laser structures”, poster at *Conf. on Lasers and Electro-Optics Europe, CLEO/Europe 2015*, Munich, Germany, June 2015.
- [6] S. Faraji, “Epitaxy and characterisation of semipolar (10-11) and (20-21) GaN on patterned sapphire substrates”, *PolarCoN Winterschool*, Reisenburg, Günzburg, Germany, March 2015.
- [7] D. Heinz, R.A.R. Leute, M. Fikry, L. Wu, D. Wu, F. Huber, O. Rettig, M. Asad, S. Bauer, M. Hocker, I. Tischer, T. Aschenbrenner, M. Schowalter, D. Hommel, A. Rosenauer, K. Thonke, and F. Scholz, “GaN-based nanostructures as novel optical sensor elements” (invited), *Recent Advances in Nano Science and Technology (RAINSAT-2015)*, Chennai, India, July 2015.
- [8] D. Heinz, O. Rettig, F. Huber, M. Madel, M. Asad, J. Jakob, S. Bauer, M. Hocker, S. Jenisch, K. Thonke, and F. Scholz, “Ga(In)N nanostructures as optical sensing elements”, poster at *Forschungstag Baden-Württemberg Stiftung*, Stuttgart, Germany, July 2015.
- [9] M. Klein, D. Heinz, T. Meisch, F. Lipski, and F. Scholz, “Ferrocene doping in hydride vapor phase epitaxy”, *6th International Symposium on Growth of III-Nitrides (ISGN-6)*, Hamamatsu, Japan, November 2015.
- [10] M. Klein, R. Leute, T. Meisch, F. Lipski, and F. Scholz, “Properties of selective area growth patterns for gallium-nitride self-separation in hydride vapor phase epitaxy”, *6th International Symposium on Growth of III-Nitrides (ISGN-6)*, Hamamatsu, Japan, November 2015.

-
- [11] R.A.R. Leute, D. Heinz, J. Wang, T. Meisch, F. Scholz, O. Rettig, F. Huber, K. Thonke, S. Jenisch, and S. Strehle, “GaN nanostripes with sub-200-nm periodicity”, *PolarCoN Winterschool*, Reisenburg, Günzburg, Germany, March 2015.
- [12] T. Meisch, K. Alkhouly, G. Gahramanova, R. Zeller, S. Schörner, K. Thonke, L. Kirste, T. Fuchs, M. Caliebe, and F. Scholz, “Planar semipolar (11-22) green In-GaN/GaN LEDs grown on patterned sapphire substrates”, *11th International Conference on Nitride Semiconductors (ICNS 2015)*, Beijing, China, September 2015.
- [13] T. Meisch, K. Alkhouly, G. Gahramanova, R. Zeller, S. Schörner, K. Thonke, L. Kirste, T. Fuchs, M. Caliebe, and F. Scholz, “Planar semipolar (11-22) green In-GaN/GaN LEDs grown on patterned sapphire substrates”, *30th DGKK Workshop Epitaxie von III-V-Halbleitern*, Göttingen, Germany, December 2015.
- [14] T. Meisch, R. Zeller, S. Schörner, and F. Scholz, “Doping behavior of (11-22) GaN grown on PSS”, *PolarCoN Winterschool*, Reisenburg, Günzburg, Germany, March 2015.
- [15] T. Pusch, M. Lindemann, N.C. Gerhardt, M.R. Hofmann, and R. Michalzik, “Increasing the birefringence of VCSELs beyond 250 GHz”, *Conf. on Lasers and Electro-Optics Europe, CLEO/Europe 2015*, Munich, Germany, June 2015.
- [16] O. Rettig, D. Heinz, S. Jenisch, F. Huber, M. Madel, S. Bauer, M. Hocker, K. Thonke, and F. Scholz, “GaN-nanowires for sensor applications”, *30th DGKK Workshop Epitaxie von III-V-Halbleitern*, Göttingen, Germany, December 2015.
- [17] F. Scholz, “GaN-based LEDs: promises and challenges” (invited), *EBV Lighting Academy*, Munich, Germany, March 2015.
- [18] F. Scholz, “GaN-based LEDs and laser diodes: promises and challenges”, seminar talk at *IMTEK, University of Freiburg*, Freiburg, Germany, November 2015.
- [19] F. Scholz, “LEDs statt Glühbirnen: Wie funktioniert’s? Was bringt’s?”, *25th Anniversary of the Faculty of Engineering and Computer Science*, Ulm University, Germany, June 2015.
- [20] F. Scholz, D. Heinz, K. Thonke, F. Huber *et al.*, “GaN-based hetero and nanostructures for chemical sensing and UV light emission”, *The International Symposium on Bio & Nano Interface*, Suzhou, China, November 2015.
- [21] F. Scholz, M. Caliebe, M. Fikry, D. Heinz, R.A.R. Leute, T. Meisch, O. Rettig, and J. Wang, “Epitaxially grown GaN-based micro- and nanostructures for optoelectronic applications”, *Sino-German Workshop on Photonic Manufacturing, Manipulation and Measurement (PMMM 2015)*, Changchun, China, July 2015.
- [22] J. Wang, T. Meisch, R. Zeller, and F. Scholz, “Internal quantum efficiency and carrier injection efficiency of c-plane, {10-11} and {11-22} InGa_N/Ga_N-based LEDs”, *PolarCoN Winterschool*, Reisenburg, Günzburg, Germany, March 2015.

-
- [23] M. Lindemann, H. Höpfner, N.C. Gerhardt, M.R. Hofmann, T. Pusch, and R. Michalzik, “Ultrafast polarization dynamics with controlled polarization oscillations in vertical-cavity surface-emitting lasers”, *SPIE Photonics West 2015*, Conf. on *Vertical-Cavity Surface-Emitting Lasers XIX*, San Francisco, CA, USA, Feb. 2015.
- [24] M. Lindemann, H. Höpfner, N.C. Gerhardt, M.R. Hofmann, T. Pusch, and R. Michalzik, “Controlling the frequency of ultra-fast polarization oscillations in spin-VCSELs”, poster at *79th Annual Meeting of the German Physical Society (DPG) and DPG Spring Meeting*, Berlin, Germany, March 2015.
- [25] M. Lindemann, T. Pusch, N.C. Gerhardt, M.R. Hofmann, and R. Michalzik, “Tuning the frequency of polarization oscillations in spin-VCSELs by mechanical strain induction”, *Conf. on Lasers and Electro-Optics Europe, CLEO/Europe 2015*, Munich, Germany, June 2015.
- [26] M. Lindemann, T. Pusch, N.C. Gerhardt, M.R. Hofmann, and R. Michalzik, “Towards high frequency operation of polarization oscillations in spin vertical-cavity surface-emitting lasers” (invited), *SPIE Optics + Photonics 2015*, Conf. on *Spintronics VIII*, San Diego, CA, USA, Aug. 2015.
- [27] M. Lindemann, H. Höpfner, N.C. Gerhardt, M.R. Hofmann, T. Pusch, and R. Michalzik, “Controlled switching and frequency tuning of polarization oscillations in vertical-cavity surface-emitting lasers”, poster at *SPIE Optics + Photonics 2015*, Conf. on *Spintronics VIII*, San Diego, CA, USA, Aug. 2015.

Publications

- [1] M. Alimoradi Jazi, T. Meisch, M. Klein, and F. Scholz, “Defect reduction in GaN regrown on hexagonal mask structure by facet assisted lateral overgrowth”, *J. Cryst. Growth*, vol. 429, pp. 13–18, 2015.
- [2] S. Bader, P. Gerlach, and R. Michalzik, “Novel oxide-free VCSEL with optically controlled current confinement”, in Online Digest *Conf. on Lasers and Electro-Optics Europe, CLEO/Europe 2015*, paper CB-2.6, one page. Munich, Germany, June 2015.
- [3] M. Caliebe, T. Meisch, M. Madel, and F. Scholz, “Effects of miscut of prestructured sapphire substrates and MOVPE growth conditions on (11 $\bar{2}$ 2) oriented GaN”, *J. Cryst. Growth*, vol. 414, pp. 100–104, 2015.
- [4] M. Daubenschütz, P. Gerlach, and R. Michalzik, “Epitaxy-based electro-thermal simulation approach for vertical-cavity surface-emitting laser structures”, in Online Digest *Conf. on Lasers and Electro-Optics Europe, CLEO/Europe 2015*, paper CB-P.14, one page. Munich, Germany, June 2015.
- [5] R.A.R. Leute, J. Wang, T. Meisch, J. Biskupek, U. Kaiser, and F. Scholz, “Blue to true green LEDs with semipolar quantum wells based on GaN nanostripes”, *Phys. Status Solidi C*, vol. 12, pp. 376–380, 2015.
- [6] T. Pusch, M. Lindemann, N.C. Gerhardt, M.R. Hofmann, and R. Michalzik, “Increasing the birefringence of VCSELs beyond 250 GHz”, in Online Digest *Conf. on Lasers and Electro-Optics Europe, CLEO/Europe 2015*, paper CB-2.2, one page. Munich, Germany, June 2015.
- [7] T. Pusch, M. Lindemann, N.C. Gerhardt, M.R. Hofmann, and R. Michalzik, “Vertical-cavity surface-emitting lasers with birefringence splitting above 250 GHz”, *Electron. Lett.*, vol. 51, pp. 1600–1602, 2015.
- [8] B. Westenfelder, J. Biskupek, J.C. Meyer, S. Kurasch, X. Lin, F. Scholz, A. Gross, and U. Kaiser, “Bottom-up formation of robust gold carbide”, *Scientific Reports*, vol. 5, pp. 8891–1–6, 2015.
- [9] S. Bauer, S. Lazarev, M. Bauer, T. Meisch, M. Caliebe, V. Holý, F. Scholz, and T. Baumbach, “Three-dimensional reciprocal space mapping with a two-dimensional detector as a low-latency tool for investigating the influence of growth parameters on defects in semipolar GaN”, *J. Appl. Cryst.*, vol. 48, pp. 1000–1010, 2015.
- [10] D.V. Dinh, M. Akhter, S. Presa, G. Kozłowski, D. O’Mahony, P.P. Maaskant, F. Brunner, M. Caliebe, M. Weyers, F. Scholz, B. Corbett, and P.J. Parbrook, “Semipolar (11 $\bar{2}$ 2) InGaN light-emitting diodes grown on chemically-mechanically polished GaN templates”, *Phys. Status Solidi A*, vol. 212, pp. 2196–2200, 2015.
- [11] Y. Han, M. Caliebe, M. Kappers, F. Scholz, M. Pristovsek, and C. Humphreys, “Origin of faceted surface hillocks on semi-polar (11 $\bar{2}$ 2) GaN templates grown on pre-structured sapphire”, *J. Cryst. Growth*, vol. 415, pp. 170–175, 2015.

- [12] M. Karlušić, R. Kozubek, H. Lebius, B. Ban-d'Etat, R.A. Wilhelm, M. Buljan, Z. Siketić, F. Scholz, T. Meisch, M. Jakšić, S. Bernstorff, M. Schleberger, and B. Šantić, “Response of GaN to energetic ion irradiation: conditions for ion track formation”, *J. Phys. D: Appl. Phys.*, vol. 48, pp. 325304-1–12, 2015.
- [13] M. Lindemann, H. Höpfner, N.C. Gerhardt, M.R. Hofmann, T. Pusch, and R. Michalzik, “Ultrafast polarization dynamics with controlled polarization oscillations in vertical-cavity surface-emitting lasers”, in *Vertical-Cavity Surface-Emitting Lasers XIX*, C. Lei, K.D. Choquette (Eds.), Proc. SPIE 9381, pp. 93810I-1–7, 2015.
- [14] M. Lindemann, T. Pusch, N.C. Gerhardt, M.R. Hofmann, and R. Michalzik, “Tuning the frequency of polarization oscillations in spin-VCSELs by mechanical strain induction”, in *Online Digest Conf. on Lasers and Electro-Optics Europe, CLEO/Europe 2015*, paper CB-2.1, one page. Munich, Germany, June 2015.
- [15] M. Lindemann, T. Pusch, N.C. Gerhardt, M.R. Hofmann, and R. Michalzik, “Towards high frequency operation of polarization oscillations in spin vertical-cavity surface-emitting lasers” (invited), in *Spintronics VIII*, H.-J. Drouhin, J.-E. Wegrowe, M. Razeghi (Eds.), Proc. SPIE 9551, pp. 95512O-1–5, 2015.
- [16] M. Lindemann, H. Höpfner, N.C. Gerhardt, M.R. Hofmann, T. Pusch, and R. Michalzik, “Controlled switching and frequency tuning of polarization oscillations in vertical-cavity surface-emitting lasers”, in *Spintronics VIII*, H.-J. Drouhin, J.-E. Wegrowe, M. Razeghi (Eds.), Proc. SPIE 9551, pp. 95512Z-1–5, 2015.
- [17] B. Neuschl, M.L. Gödecke, K. Thonke, F. Lipski, M. Klein, F. Scholz, and M. Feneberg, “Zeeman spectroscopy of the internal transition 4T_1 to 6A_1 of Fe^{3+} ions in wurtzite GaN”, *J. Appl. Phys.*, vol. 118, pp. 215705-1–10, 2015.
- [18] I. Tischer, M. Hocker, B. Neuschl, M. Madel, M. Feneberg, M. Schirra, M. Frey, M. Knab, P. Maier, T. Wunderer, R.A.R. Leute, J. Wang, F. Scholz, J. Biskupek, J. Bernhard, U. Kaiser, U. Simon, L. Dieterle, H. Groiss, E. Müller, D. Gerthsen, and K. Thonke, “Optical properties of defects in nitride semiconductors”, *J. Mater. Res.*, vol. 30, pp. 2977–2990, 2015.



ulm university universität
uulm

Ulm University
Institute of Optoelectronics
Albert-Einstein-Allee 45
89081 Ulm | Germany